Università degli Studi di Napoli *Federico II*

Scuola Politecnica e delle Scienze di Base
Collegio di Scienze

Dipartimento di Fisica "Ettore Pancini"

DOTTORATO DI RICERCA IN FISICA

Ciclo XXX

Coordinatore: Prof. Salvatore Capozziello

Settore Scientifico Disciplinare FIS/07

Breast cancer: imaging and radiotherapy with synchrotron radiation

Tutori	**Candidata**
Prof. Paolo Russo	Dott.ssa Francesca Di Lillo
Prof. Giovanni Mettivier	

Anni Accademici 2014/2017

Università degli Studi di Napoli *Federico II*

Scuola Politecnica e delle Scienze di Base

Collegio di Scienze
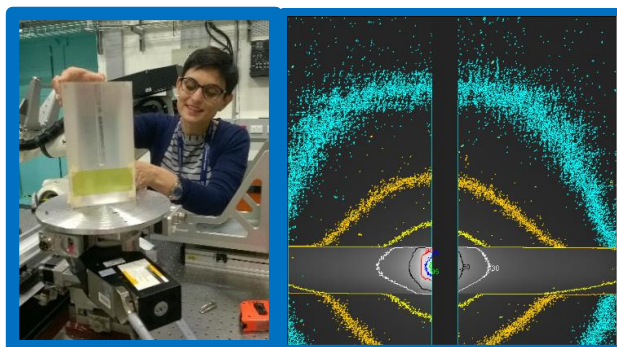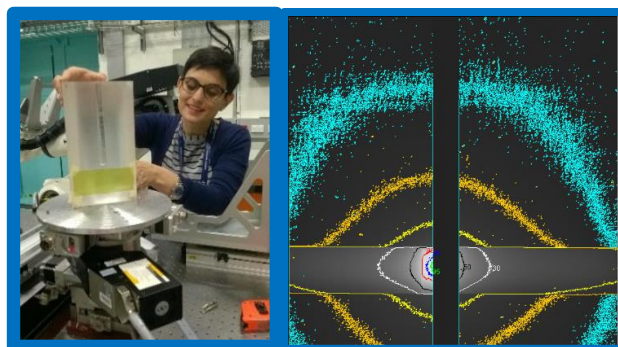
Dipartimento di Fisica "Ettore Pancini"

PhD IN PHYSICS

Cycle XXX

Chair of PhD School: Prof. Salvatore Capozziello

Settore Scientifico Disciplinare FIS/07

Breast cancer: imaging and radiotherapy with synchrotron radiation

Supervisors	**Candidate**
Prof. Paolo Russo	Dott.ssa Francesca Di Lillo
Prof. Giovanni Mettivier	

Academic Years 2014/2017

Alla mia famiglia

"A scientist in his laboratory is not a mere technician:
he is also a child confronting natural phenomena that
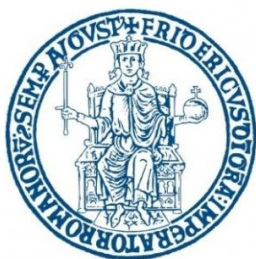*impress him as though they were fairy tales"*

M. Curie

Preface

This dissertion is submitted for the degree of *Philosophiae Doctor* (Ph.D.) in Physics at Università di Napoli Federico II, Italy. I present the research on the use of the synchrotron radiation for imaging and radiotherapy of breast cancer.

The studies described in this thesis were conducted under the supervision of Prof. Paolo Russo and co-supervision of Prof. Giovanni Mettivier who approved this thesis.

My work was carried out at the following institutions/facilities:

Contents

List of Publications (from November 2014 to October 2017)

1. **Di Lillo F**, Dreossi D, Emiro F, Fedon C, Longo R, Mettivier G, Rigon L, Russo P, & Tromba G (2015) Use of XR-QA2 radiochromic films for quantitative imaging of synchrotron radiation beam. *J Instrum* **10**, C05002.

2. Emiro F, **Di Lillo F**, Mettivier G, Fedon C, Longo R, Tromba G, Russo P (2015). Energy response of GR-200A thermoluminescence dosemeters to ^{60}Co and to monoenergetic synchrotron radiation in the energy range 28–40 keV. *Rad Protec Dosim* **168**, 40–45.

3. Mettivier G, Fedon C, **Di Lillo F**, Longo R, Sarno A, Tromba G and Russo P. (2016) Glandular dose in synchrotron radiation breast computed tomography *Phys. Med. Biol.* **61** 569–587. (Featured article)

4. Russo P, Larobina M, **Di Lillo F**, Del Vecchio S, Mettivier G (2016) Combined SPECT/CT and PET/CT for breast imaging. *Nucl. Instrum. Methods Phys. Res*. A **809**, 58–66.

5. Longo R, Arfelli F, Bellazzini R, Bottigli U, Brez A, Brun F, Brunetti A, Delogu P, **Di Lillo F**, Dreossi D, Fanti V, Fedon C, Golosio B, Lanconelli N, Mettivier G, Minuti M, Oliva P, Pinchera M, Rigon L, Russo P, Sarno A, Spandre G, Tromba G and Zanconati F. (2016) Towards breast tomography with synchrotron radiation at Elettra: first images *Phys. Med. Biol.* **61** 1634–1649.

6. Sarno A, Mettivier G, Golosio B, Oliva P, Spandre G, **Di Lillo F**, Fedon C, Longo R and Russo P. (2016) Imaging performance of phase-contrast breast computed tomography with synchrotron radiation and a CdTe photon-counting detector *Phys. Medica* **32** 681–690.

7. **Di Lillo F**, Mettivier G, Sarno A, Tromba G, Tomic N, Devic S and Russo P. (2016) Energy dependent calibration of XR-QA2 radiochromic film with monochromatic and polychromatic x-ray beams *Med. Phys.* **43** 583–588.

8. Sarno A, Mettivier G, **Di Lillo F** and Russo P. Monte Carlo evaluation of normalized glandular dose coefficients in mammography *In: Breast Imaging.* Proc. of 13th International Workshop, IWDM 2016, Malmö, Sweden, June 19-22, 2016, *Lecture Notes in Computer Science, Springer International Publishing, vol 9699,* 190–196 DOI 10.1007/978-3-319-41546-8_25.

9. Giovanni M, Bliznakova K, **Di Lillo F**, Sarno A and Russo P. Evaluation of the BreastSimulator Software Platform for Breast Tomography: Preliminary Results. Proc. of 13th International Workshop, IWDM 2016, Malmö, Sweden, June 19-22, 2016, *Lecture Notes in Computer Science, Springer International Publishing, vol 9699,* 145–151.

10. Sarno A, Mettivier G, **Di Lillo F**, Cesarelli M, Bifulco P and Russo P. (2016) Cone-beam micro computed tomography dedicated to the breast *Med. Eng. Phys.* **38** 1449–1457.

11. Sarno A, Mettivier G, **Di Lillo F** and Russo P. (2016) A Monte Carlo study of monoenergetic and polyenergetic normalized glandular dose (DgN) coefficients in mammography *Phys. Med. Biol.* **62** 306–325 .

12. Delogu P, Golosio B, Fedon C, Arfelli F, Bellazzini R, Brez A, Brun F, **Di Lillo F**, Dreossi D, Mettivier G, Minuti M, Oliva P, Pichera M, Rigon L, Russo P, Sarno A, Spandre G, Tromba G and Longo R. (2017) Imaging study of a phase-sensitive breast-CT system in continuous acquisition mode *J. Instrum* **12** C01016.

13. Sarno A, Dance D R, van Engen R E, Young K C, Russo P, **Di Lillo F**, Mettivier G, Bliznakova K, Fei B W and Sechopoulos I. (2017) A Monte Carlo model for mean glandular dose evaluation in spot compression mammography. *Med. Phys.* 44 (7), 3848–3860.

14. Sarno A, Golosio B, Russo P, Arfelli F, Bellazzini R, Brez A, Brun F, Delogu P, **Di Lillo F**, Dreossi D, Fedon C, Longo R, Mettivier G, Oliva P, Rigon L, Spandre G and Tromba G. (2017) A framework for iterative reconstruction in phase-contrast computed tomography dedicated to the breast. *Trans. Rad. Pl. Med. Sc, DOI 10.1109/TRPMS.2017.2749059.*

15. Sarno A, Masi M, Antonelli N, **Di Lillo F**, Mettivier G, Castriconi R and Russo P. (2017) Dose Volume Distribution in Digital Breast Tomosynthesis: a Phantom Study. *Trans. Rad. Pl. Med. Sc.* **1**(4), 322–328.

16. Mettivier, G., Bliznakova, K., Sechopoulos, I., Boone, J., **Di Lillo, F.,** Sarno, A., Castriconi R. & Russo, P. (2017). Evaluation of the BreastSimulator software platform for breast tomography. *Phys Med Biol* **62**(16), 6446–6466.

17. Stevenson, A.W., and **Di Lillo, F.** (2017). Estimating the absolute flux distribution for a synchrotron X-ray beam using ionization-chamber measurements with various filters. *J Synchrotron Rad* **24**(5), 939–953.

18. **Di Lillo, F.,** Mettivier, G., Sarno, A., Castriconi, R., and Russo, P. (2017). Towards

breast cancer rotational radiotherapy with synchrotron radiation. *Phys Med*, *41*, 20-25.

Ongoing Papers:

1. **Di Lillo, F**., Mettivier, G., Castriconi, R., Sarno, A., Stevenson, A.W., Hall, C.J., Häusermann, D., and Russo, P. (2017) Synchrotron radiation external beam rotational radiotherapy of breast cancer: proof of principle. J Synchrotron Rad, *under review.*

List of Conference Presentations

1. **Di Lillo, F.**, Stevenson, A.W., Mettivier, G., Sarno, A., Castriconi, R., Hall, C.J., Häusermann, D., Russo, P. "Monte Carolo simulation and simple model of dose distribution in synchrotron radiation rotational radiotherapy of breast cancer : An experimental phantom study", Poster Presentation at International Conference on Monte Carlo techniques for Medical applications, Napoli, Italy, October 16th-18th, 2017.

2. **Di Lillo, F.**, Mettivier, G., Castriconi, R., Sarno, A., Hall, C.J., Häusermann, D., Stevenson, A.W., Russo, P. "Breast cancer rotational radiotherapy with synchrotron radiation". Oral presentation at Australian Synchrotron User Meeting 2016, Melbourne, Australia, November 24th-25th, 2016.

3. **Di Lillo, F.**, Mettivier, G., Sarno, A., Russo, P. "Towards breast cancer rotational radiotherapy with synchrotron radiation". Oral presentation at 1st European Congress of Medical Physics, Athens, Greece, September 1st-4th, 2016. This presentation was selected to contribute a paper to the Focus Issue of the journal Physica Medica: European J. Med. Phys. with the topic "ECMP 2016".

4. **Di Lillo, F.**, Corvino, V., Sarno, A., Mettivier, G., Russo, P. "Performance of MediPROBE compact gamma camera". Poster presentation at 9° Italian National Congress AIFM (Italian Association of Medical Physics), Perugia, Italy, February 25th-28th, 2016.

List of Figures

List of Tables

Abstract

The breast cancer is the most common cancer in woman worldwide. In this scenario, two aspects are very important: the early diagnosis and the efficacy of the care. The gold standard for the screening of breast cancer is the two-view mammography and the standard care includes surgery, usually coupled with chemotherapy or radiotherapy with 6-MV X-ray tangential beams from a linear accelerator. The problem of superimposition of tissue along the direction of the beam, which can make difficult the task of lesion detection in mammography, has led to the development of 3D techniques – such as Digital Breast Tomosynthesis (DBT) and Breast Computed Tomography (BCT) – which resolve the breast anatomy also in the longitudinal direction. In addition, in the last decades the use of phase-contrast (PhC) imaging techniques (which permit to detect the phase-shift of the X-ray beam in tissue) produced improvements in the detection of breast cancer. As regards adjuvant radiotherapy of breast cancer, an effective treatment has to guarantee the maximum sparing to the healty tissues, in particular to the skin. For this purpose, new techniques – such as IMRT, helical tomotherapy, VMAT – are under clinical investigation. Moreover, new kilovoltage rotational radiotherapy techniques with X-ray beam from orthovoltage X-ray tube as well as linear accelerator have been proposed.

In this work, we investigated the use of the synchrotron radiation (SR) for both low-dose phase-contrast breast computed tomography (PhC-BCT) and breast rotational radiotherapy, via Monte Carlo simulations and measurements. Experiments were conducted at three different synchrotron radiation facilities: ELETTRA (Trieste, Italy), ESRF (Granoble, France), Australian Synchrotron (Melbourne, Australia). Phase contrast mammography on a cohort of patients was pioneered at ELETTRA in the last decade, showing the advantage of propagation based PhC imaging in producing higher conspicuity of breast masses; the ongoing projects at ELETTRA aim at devising a setup and a protocol for future computed tomography (CT) scans of the breast.

The first part of the work, carried out in the framework of the SYRMA-CT/3D projects funded by INFN (National Institute for Nuclear Physics, Italy), showed the dosimetry measurements as well as the first imaging test of PhC-BCT at ELETTRA, carried out at 38 keV or lower energies. New dose metrics were introduced to take into account the partial breast irradiation envisaged for the exam; in addition, we carried out a characterization of dosimeters (TLD GR-200A and radiochromic film XR-QA2) to be employed for beam and phantom dosimetry. Finally, we showed the results of the first imaging test with a breast tissue specimen.

In the second part of this PhD work, we demonstrated the feasibility of rotational breast radiotherapy with synchrotron radiation laying the foundations for the study of a new image-guided radiotherapy technique for breast cancer. This technique employs the same setup used for BCT but uses higher energies (60–120 keV) and higher intensity SR beams. The use of such low photon energies (with respect to megavoltage photon energies used in conventional radiotherapy) would provide a higher dose-enhancement when a radiosensitizing (e.g. gold nanoparticles) is used for breast radiotherapy. Possible applications of this technique could be the treatment of the small lesion and hypo-fractionated radiotherapy.

Introduction

Breast cancer is the most common cancer in women. The effective care requires an early diagnosis by mammography screening and includes surgery, usually coupled to chemotherapy and radiotherapy. The conventional radiotherapy of breast cancer uses 6-MV tangential X-ray beams produced with a medical accelerator (linac). In the last decades, 3D conformal radiotherapy (3D-CRT), Intensity Modulated Radiotherapy (IMRT) and Protontherapy are also employed for treatment of the breast cancer.

In the last years, the use of a synchrotron radiation (SR) source has been proposed for investigating improvements of the mammography technique through phase-contrast imaging, which may permit to increase the contrast between tumour and healthy tissue and the lesion conspicuity. This activity has been carried out, in particular, at the SYRMEP beamline of ELETTRA synchrotron radiation facility in Trieste, Italy. The National Institute of Nuclear Physics (INFN) in Italy has promoted research projects dedicated to phase-contrast breast computed tomography (BCT) with SR by using a high-spatial resolution photon counting detector. These projects (SYRMA-CT and SYRMA-3D), based at ELETTRA, involve a large collaboration including University of Trieste, University of Napoli Federico II, University of Cagliari, University of Sassari, University of Pisa, University of Siena, University of Ferrara, and the INFN sections of Napoli, Trieste, Cagliari, Pisa and Ferrara as well as the INFN spin-off PIXIRAD srl (the latter involved in the SYRMA-CT project).

At the same time, as a specific outcome of the activity of Naples medical physics group on cone-beam BCT as well as SR-BCT, the Naples team proposed the use of the high intensity monoenergetic SR beam for breast radiotherapy as an alternative to the conventional treatment with 6-MV X-ray beams.

Both CT *breast imaging* with SR source and phase contrast techniques, and *breast radiotherapy* with a SR source, have been the object of my PhD activity on breast cancer research, during the period November 2014 – October 2017. As a consequence, this thesis comprises two parts, as briefly outlined in this introduction and thoroughly illustrated in the following pages.

My thesis work has been focused, for the first part, on the SYRMA-CT project in which the Naples medical physics group has been responsible for phantom and beam dosimetry. I participated in all mesurement shifts at the ELETTRA facility dedicated to beam and phantom dosimetry, and to the corresponding data analysis. My specific contribution was on the assessment of accuracy and energy response of the dosimeters employed in the SYRMA-CT experiment (TLDs, radiochromic films, ion chambers), and in the analysis of the first images.

As regards research on SR breast radiotherapy, a project (SR^{3}T) has been recently approved by INFN and will involve activities carried out at the European Synchrotron Radiation Facility (ESRF) (Grenoble, France), Australian Synchrotron (AS) (Melbourne, Australia) and also Canadian Light Source (Saskatoon, Canada). The study of SR rotational radiotherapy for breast cancer treatment has been the main object of the second part of my thesis work. I was totally involved in conceiving and in the first tests of SR breast radiotherapy by participating in all phases of data acquisition, data analysis and scientific publications.

In this thesis, from measurements carried out at the ELETTRA facility within the SYRMA-CT/SYRMA-3D collaborations, the synchrotron radiation (SR) source (photon energy = 38 keV) proved to be effective in producing high contrast, high resolution phase-contrast images of the breast anatomy in mastectomy samples, after retrieval of the phase map. For Monte Carlo (MC) determination of normalized glandular dose coefficients in a SR BCT scan, new dose metrics will be presented, which will take into account the different geometry of a mammography or a dedicated cone-beam CT scan (where the whole breast is irradiated) with respect to the partial irradiation of a SR BCT scan (where only a thin layer of the breast is irradiated).

The analysis of the mono-energetic dose distributions in such 360-deg scans around the breast, derived from MC simulations, led us naturally to explore the case of the SR irradiation in a circular orbit of a small volume of the breast, simulating a small lesion. In this case the SR beam is collimated horizontally – in addition to being collimated in the vertical direction for definition of the breast layer. We then investigated the possibility of performing (high-dose) breast 3D radiotherapy in addition to (low-dose) breast 3D imaging, by adopting a (horizontally collimated)

rotational irradiation of the pendant breast with a SR beam with photon energy in the range 60-120 keV. Indeed, such a new technique of kilovoltage rotational radiotherapy of breast cancer with a SR source can produce skin-to-tumor dose ratios comparable to those achievable with conventional megavoltage breast radiotherapy, and also comparable to that indicated by J. Boone at UC Davis using orthovoltage rotational breast radiotherapy. With respect to this last technique (operating at about 320 kVp, effective energy about 180 keV) the SR source would present the advantage of a higher flux and of a lower achievable energy (down to e.g. 60 keV), which would permit to have higher dose enhancements when using a radiosensitizing agent (e.g. gold nanoparticles) for breast radiotherapy.

The thesis is divided in two parts.

In the first part, I describe the work related to phase-contrast breast computed tomography.

In the second part of this thesis, I present the first feasibility studies of SR^{3}T carried out at Imaging and Medical Beamline (IMBL) of AS and ID 17 beamline of ESRF. In particular, I report the results of the first proof-of-concept at 60 keV as well as the study at higher energies in the range 80–175 keV and the preliminary results of the use of dose-enhancement agents.

The strategy followed in writing my thesis was to illustrate the diverse scientific papers, which are the scientific product of this thesis work, highlighting my role in SYRMA-CT/3D and SR^{3}T collaboration. The list of papers that I co-authored in the last three year as well as the list of conference presentations, which I attended for poster or oral presentation, are present in the previous pages and include both my activities.

PART I

Breast Computed Tomography with synchrotron radiation

1.1 Introduction

This paragraph of the thesis presents the description of the projects on breast computed tomography with synchrotron radiation (SYRMA-CT and SYRMA-3D) in which I was involved during my PhD work. The text describes the content of the following publications:

- Longo, R., Arfelli, F., Bellazzini, R., Bottigli, U., Brez, A., Brun, F., Brunetti, A., Delogu, P., Di Lillo, F., Dreossi, D., Fanti, V., Fedon, C., Golosio, B., Lanconelli, N., Mettivier, G., Minuti, M., Oliva, P., Pinchera, M., Rigon, L., Russo, P., Sarno, A., Spandre, G., Tromba, G., & Zanconati, F. (2016). Towards breast tomography with synchrotron radiation at Elettra: first images. *Phys. Med. Biol.* **61**(4), 1634–1649.
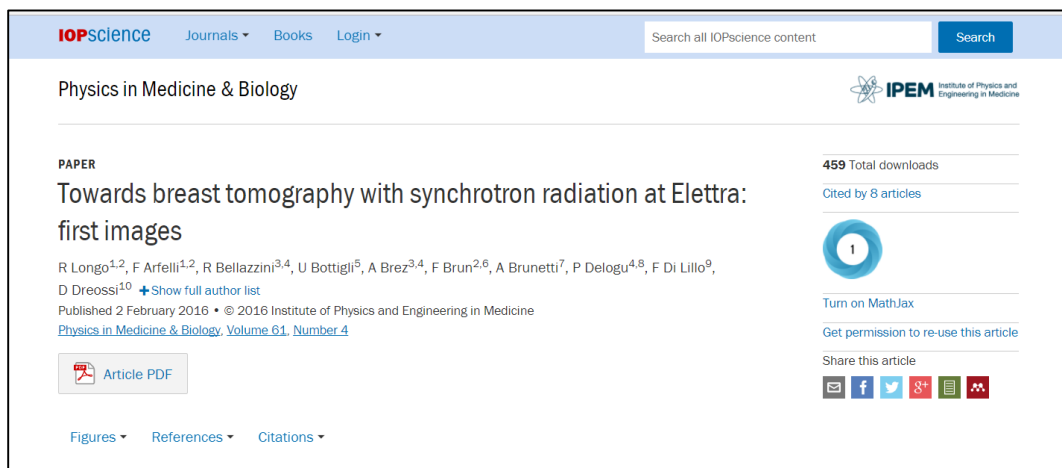
- Delogu, P., Golosio, B., Fedon, C., Arfelli, F., Bellazzini, R., Brez, A., Brun, F., Di Lillo, F., Dreossi, D., Mettivier, G., Minuti, M., Oliva, P, Pinchera, M., Rigon, L, Russo, P., Sarno, A., Spandre, G., Tromba, G., Longo, R. (2017) Imaging study of a phase-sensitive breast-CT system in continuous acquistion mode. *J. Instrum.* **12**, C01016.

1.1.1 Background

The gold standard imaging technique for screening of breast cancer is mammography. The introduction of the screening program in the late 80's (Shapiro *et al*, 1998) resulted in a significant reduction of the rates death due to the breast cancer in women in the next years. In a study on the cancer mortality predicted for 2017 in Europe, Malvezzi *et al.* (2017) show that the rate of more than 20 cancer deaths per 100.000 females in 1990 decreased to 15.19 per 100.000 females in 2012; they also predict a rate of cancer deaths of about 14.03 per 100.000 females in 2017. Similar results are showed by Siegel *et al.* (2016) for cancer statistics in USA where the death rates were from about 35 per 100.000 female in 1990 to about 20 per 100.000 females in 2012. Although mammography specificity – defined as *the percentage of non-cancer with a negative initial interpretation* (BCSC 2009) – is about 90.3 % (BCSC 2009), its sensitivity – defined as *the percentage of cancers with an initial positive interpretation* (BCSC 2009) – is about 84.9 % (BCSC 2009). The main limitation of sensitivity for mammography is that it is a form of planar imaging which cannot overcome the superimposition of the tissues in the direction of the X-ray beam. This makes difficult the detection of breast lesions immersed in normal glandular tissue. 3D imaging techniques such as Digital Breast Tomosynthesis (DBT) (Sechopoulos, 2013a, 2013b) and Breast Computed Tomography (BCT) (Sarno *et al*, 2015, Prionas *et al* 2010, O'Connell *et al*, 2014, Zhao *et al*, 2015) have been proposed to overcome this problem. In DBT, several projections of the organ are acquired at different angles in a limited range by rotating

the X-ray tube around the compressed breast while detector can be fixed or can rotate with the surface perpendicular to the X-ray beam. The reconstructed images provides *"a 3D distribution of the tissue with an anisotropic spatial resolution"* (Sechopoulos, 2013a, 2013b). DBT is now a clinical practice which can be employed coupled with mammography. In BCT, the patient is prone on a bed with a hole for the hanging breast. The X-ray tube as well as the X-ray detector is on a rotating gantry and rotates around the uncompressed breast. This technique permits to obtain a 3D image of the breast with an isotropic spatial resolution (Sarno, 2017a). However, the dose to the organ is a significant constraint for the technique (Kalender *et al*, 2012, Vedantham *et al*, 2013, Sarno *et al*, 2015). Indeed, the mean dose to the glandular tissue (MGD) in a BCT exam may be comparable with, or lower than, the MGD delivered to the same breast in a mammography exam with the compressed breast. This value ranges between 3 and 4 mGy in two-view mammography, for a standard breast (Sarno *et al*, 2015). The BCT scanner produced by Koning corp (http://koninghealth.com/) is the only system which obtained CE mark (2012); in its FDA approval document (2015) this device should be used as diagnostic technique coupled with two-view mammography (Sarno, 2017a). BCT did not receive FDA approval for breast cancer screening, but it provides additional information with respect to mammography to determine if a patient with a suspicious abnormality needs a needle biopsy.

The conventional CT is based on the detection of the X-ray attenuation signal and provides a 3D map of the attenuation coefficient of the sample. In the last decades, new techniques for phase-shift detection, called phase-contrast (PhC) imaging techniques, have been investigated (Fiedler *et al,* 2004*;* Bravin *et al*, 2013; Keyriläinen *et al*, 2005, 2008; Momose *et al*, 1996; Sztrókay *et al*, 2013; Takeda *et al,* 1998, 2000; Zhao *et al,* 2012; David *et al,* 2007*;* Cai and Ning, 2009; Snigirev *et al*, 1995; Wilkins *et al*, 1996). The simplest PhC technique to be implemented is Propagation-based imaging (PBI) (Snigirev *et al*, 1995; Wilkins *et al*, 1996) which requires an acquisition system similar to that used in attenuation-based imaging without any sophisticated X-ray optics (Wilkins *et al*, 1996). This setup employs an X-ray beam with high-spatial coherence – such as Synchrotron Radiation (SR) beam (Snigirev *et al*, 1995, Longo *et al,* 2016, Sarno *et al,* 2016a, Nesterets *et al,* 2015) or

the X-ray beam from a micro-focus X-ray tube (Wilkins *et al*, 1996, Auweter *et al* 2014, Sarno *et al*, 2016d) – and a detector with high-spatial resolution placed at a distance from the sample sufficient to detect the interference pattern in the transmitted beam. However, the requirement for the high-spatial resolution detector may, in some cases, be relaxed in the case of micro-focus X-ray sources in the laboratory context. The PBI technique can provide an edge-enhancement in the attenuation images useful to recognise small details in the image. Moreover, the phase signal can be separated from the absorption signal by applying a specific algorithm on the projection images before CT reconstruction. The most diffuse algorithm is based on the homogeneous transport of an intensity equation (Paganin *et al*, 2002).

The use of PBI technique for breast imaging with SR source is under investigation (Castelli *et al*, 2011, Longo *et al*, 2014, 2016, Nesterets *et al,* 2015, Sarno *et al*, 2016c, Coan *et al*, 2013). The SR source provides a monoenergetic laminar X-ray beam, tunable in energy, with high flux and a very high-spatial coherence which permits to investigate the phase effects. The first clinical trial of PhC-mammography with SR was performed at SYRMEP beamline of ELETTRA synchrotron facility in Trieste, Italy (Castelli *et al*, 2011, Longo *et al*, 2014) showing an improvement of the image quality with MGD values comparable to that delivered for conventional two-view mammography in the order of 3-4 mGy for a standard breast (Sarno *et al*, 2015). Moreover, recent study on BCT with synchrotron radiation (SR-BCT) have compared the PBI to absorption-based imaging revealing a significant improvement of the image quality when the PhC technique is employed (Pacilè *et al, 2015; Nesterets *et al,* 2015; Longo *et al,* 2016). At the present, SR-BCT is investigated at the SR facility ELETTRA (Trieste, Italy) (Castelli *et al* 2011; Quai *et al* 2013; Longo *et al* 2014, 2016; Pani *et al* 2004; Pacilè *et al* 2015; Tromba *et al*, 2016), at the European Synchrotron Radiation Facility in Grenoble, France (Fiedler *et al* 2004; Bravin *et al* 2013; Keyriläinen *et al* 2005, 2008) and at the Imaging and Medical beamline of the Australian Synchrotron (Nesterets *et al* 2015, Tromba *et al*, 2016).

1.1.2 SYRMA-CT and SYRMA-3D Projects

The SYRMA-CT project (2014-2016) has been proposed in the scenario described in the previous section. Its following project SYRMA-3D (2017-2018) should conclude the five-year research effort for demonstrating the feasibility of BCT with monoenergetic X-rays using phase-contrast techniques and a synchrotron radiation source. The SYRMA-CT/3D (SYnchrotron Radiation- MAmmography-Computed Tomography/three-Dimensional) collaboration aims *"to set-up the first clinical trial of PhC breast CT with SR at the SYRMEP (SYnchrotron Radiation for MEdical Physics) beamline of Elettra, the synchrotron radiation laboratory in Trieste (Italy)"* (Longo *et al*, 2016). The projects have a number of innovative elements such as the use of a CdTe single-photon counting detector, state-of-art CT reconstruction techniques and phase retrieval algorithms, and an *ad-hoc* dose metric. The merge of these elements will provide the highest image quality with the lower delivered dose. The SYRMA-CT/3D projects, funded by INFN (Istituto Nazional di Fisica Nucleare. Italy) involve several Italian institutions such as University of Napoli "Federico II", University of Trieste, University of Cagliari, University of Pisa, University of Siena and University of Ferrara, together with the INFN sections of Napoli, Trieste, Cagliari, Pisa and Ferrara and the INFN spin-off PIXIRAD srl (partner in SYRMA-CT project only) and the Elettra-Sincrotrone Trieste SPcA where the SYRMA-CT/3D system is installed.

Setup @ SYRMEP

ELETTRA is a third generation SR facility with a 259.2 m-circumference storage ring, which operates in "top-up" mode at two different electron energies of 2 and 2.4 GeV. The ring current is 300 mA and 140 mA at 2.0 GeV and 2.4 GeV, respectively (https://www.elettra.trieste.it/lightsources/elettra/elettra-parameters. html?showall=).

SYRMEP beamline is dedicated to research in medical diagnostic radiology, material science and life science applications. The X-ray beam produced by a storage ring bending magnet is monochromatized by a double-crystal Si (111) monochromator working in the energy range 8–38 keV with an energy resolution of

0.2% (https://www.elettra.trieste.it/lightsources/elettra/elettra-beamlines/syrmep/ specification.html.). SYRMEP has three hutches: the optical hutch, the experimental hutch, the patient room. The maximum beam size in the patient room is 220 mm (horizontal) × 5 mm (vertical, Gaussian shape, evaluated as the FWHM of the Gaussian shape) (Abrami *et al*, 2005). The patient room hosts a clinical bed in carbon fibre (210-cm length and 80-cm width) with a 25-cm diameter hole (Figure 1.1) The patient lies prone on the bed with one breast hanging from the hole. A compression system can be used for mammographic exam. The detector is placed on a dedicated rail which permits to select the optimal sample-to-detector distance, up to 2 m, for detecting phase effects. Since the beam is fixed, the patient support has to rotate in order to collect the CT projections.

SYRMEP has a specific dose control system to guarantee low dose levels to the patient during the exams. It consists of a set of shutters with a fast opening/closing system and two parallal-plate ionization chambers (IOC). The IOCs are employed as dose monitor on the beamline. They were designed and constructed at ELETTRA laboratories specifically for the laminar beam geometry. Their response was calibrated against the air kerma primary standard of the INMRI-ENEA (Italia National Institute for Ionizing Radiation Metrology) in the energy range 8–28 keV.

As regards the acquisition protocol, the negligible horizontal divergence of SR beam (7 mrad) permits acquisition in parallel geometry and therefore the CT scan will be performed in axial mode over 180 degrees. On the other hand, the laminar shape of the SR beam requires multiple rotations to image the breast volume. In order to reduce the scan time and limit the number of rotations of the patient, the SYRMA-CT collaboration plans to irradiate only the part of the breast where the suspected lesion is localized with a rotate/translate scan geometry (Longo *et al*, 2016).

Figure 1.1: Photo of the SYRMA-CT setup for phase-contrast breast CT at the ELETTRA synchrotron radiation laboratory (Trieste, Italy). The horizontal beam irradiates the breast hanging from a hole in the patient bed; the transmitted beam is recorded by a high resolution photon counting detector. Rotation and translation of the bed permits to acquire in successive axial scans over 180 deg a complete dataset for CT reconstruction. (from Sarno et al, 2016c)

CdTe single photon counting detector: PIXIRAD

One of the innovative elements of SYRMA-CT/3D projects is the use of a photon counting detector. The collaboration decided to employ a multi-block module (PIXIRAD-8) of 8 units (PIXIRAD) for a global active area of 250mm × 25mm. The detector is produced by PIXIRAD Imaging counter s.r.l (http://www.pixirad.com/), an INFN Pisa spin-off company. PIXIRAD is a hybrid detector composed of a 0.65 mm-thick CdTe sensor layer with an area of 30.96 mm × 24.98 mm electrically connected to a CMOS VLSI chip with an active area of 30.7mm × 24.8mm by bump-bonding process. The CdTe sensor (ACRORAD Co., Ltd.)) is a Schottky type array of diodes. As reported by Bellazzini *et al* (2013), "*ASIC is organized as a matrix of 512×476 hexagonal pixels that match the identical pixel arrangement of the CdTe crystal. Each pixel is connected to a charge amplifier which feeds two discriminator and two 15-bit counters.*" The pixel pitch is 60 μm. The detector can work in either dual-thresholds mode (2 colours mode) or single-threshold continuous reading mode (Bellazzini *et al*, 2013).
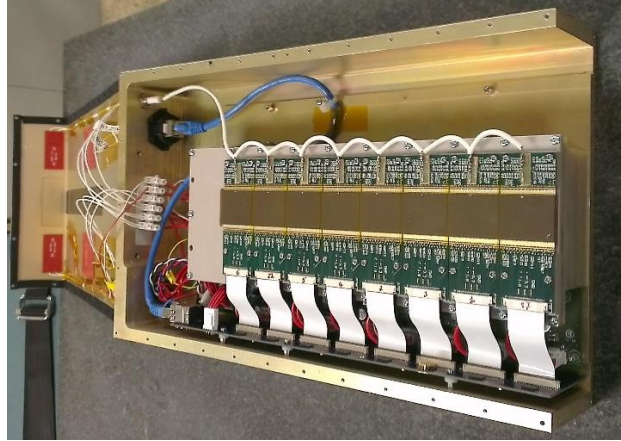
Figure 1.2: PIXIRAD-8: the single blocks are assembled and placed in a metal case (from Longo *et al*, 2016)

In continuous reading mode, both counters work by using the same threshold and photons are counted in one counter while reading the other one. In this way, a dead-time free modality is obtained. The modular structure of PIXIRAD-8 detector produces a dead space of 180 μm between adjacent blocks.

1.2 Dosimetry in breast computed tomography with synchrotron radiation

1.2.1 Dosimeters Characterization

During the first part of the SYRMA-CT project on which my work was centred, due attention was given to determine an accurate beam dosimetry. This implies the use of TLD dosimeters and film dosimeters, which we characterized at the energy of the SR beam. This work resulted in the publication of the following two papers in international scientific journals. Here, we describe this work as illustrated in the corresponding papers.

- Di Lillo, F., Mettivier, G., Sarno, A., Tromba, G., Tomic, N., Devic, S. & Russo, P. (2016a) Energy dependent calibration of XR-QA2 radiochromic film with monochromatic and polychromatic x-ray beams. *Med. Phys.* **43**(1), 583–588.

- Emiro, F., Di Lillo, F., Mettivier, G., Fedon, C., Longo, R., Tromba, G. & Russo, P. (2015) Energy response of GR-200A thermoluminescence dosemeters to 60Co and to monoenergetic synchrotron radiation in the energy range 28–40 keV. *Rad. Prot. Dosim.* **168**(1), 40–45.

Energy response of GR-200A thermoluminescence dosemeters to ^{60}Co and to monoenergetic synchrotron radiation in the energy range 28–40 keV

F. Emiro, F. Di Lillo, G. Mettivier ✉, C. Fedon, R. Longo, G. Tromba, P. Russo

Views ▾   PDF   Cite   Permissions   Share ▾

TLDs and radiochromic films were characterized in the effective photon energy in the range 18–46.5 keV, corresponding to half value layer (HVL) extending from 0.55 mm Al to 6.09 mm Al as shown Figure 1.3. A 100-mm long ionization chamber (mod. 20X6-3CT, with mod. 2026C dosimeter, Radcal Corp., Monrovia, CA, USA, with an active volume of 3 cm^3) was used as reference. This chamber is factory calibrated at 150 kV, HVL = 10.2 mm Al with an accuracy ± 4% after temperature and pressure correction. However, for beam energies in the range 18–28 keV, the response of the chamber was calibrated in terms of air kerma free-in-air, with respect to a calibrated parallel-plate transmission chamber (IOC) employed as the dose monitor on the SYRMEP beamline. For calibration, the ionization chamber was positioned horizontally along the beam width direction and translated along the vertical direction to expose its entire active volume to the thin laminar beam (Prezado *et al*, 2011). Table 1.1 reports the air kerma calibration factors for the Radcal ionization chamber estimated at 18, 20, 24, and 28 keV. For energies higher than 28 keV, since the SYRMEP monitor chamber are not calibrated, the air kerma values measured with the 100-mm chamber were obtained by using the manufacturer calibration data. Furthermore, temperature, pressure, and energy dependence corrections were applied; the coefficients for energy dependence correction were those provided by the manufacturer.
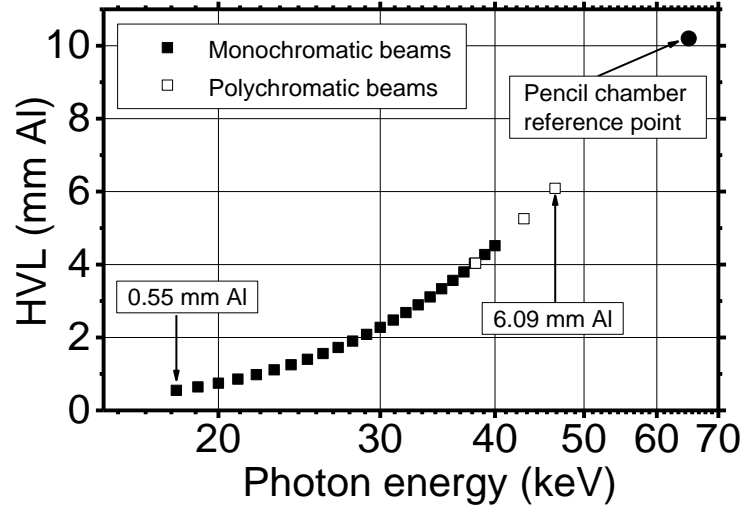
Figure 1.3: HVLs and effective energies employed in this study with monochromatic and polychromatic X-ray beam. (from Di Lillo *et al*, 2016a)

Table 1.1: Air kerma calibration factor for Radcal ion chamber. The values were estimated with reference to a calibrated transmission chamber on the SYRMEP beamline at ELETTRA SR facility. (from Di Lillo *et al*, 2016a)

Photon energy (keV)	Calibration factor
18	0.978
20	0.935
24	0.932
28	0.911

1.2.1.1   Characterization of radiochromic film XR-QA2

The GafChromic™ XR-QA2 film (Ashland, NJ, USA) is intended for quality control in radiology applications. These films can also be used as 2D dosimeters. By specifications, the film is sensitive in the dose range 1−200 mGy in the photon energy range 20−200 keV. The film consists of a 25-μm thick active layer attached to an acrylic adhesive layer of 20-μm thickness and sandwiched between two 97-μm thick polyester layers, one with an orange colour on the front and the other with a white colour on the back (Figure 1.4). Nominally, the active layer consists of H, Li, C, N, O, Bi (table 1.2). The inclusion of Bi ($Z = 83$) boosts the photoelectric cross section and improves the film sensitivity to lower X-ray energy. On the other hand, the

presence of bismuth in the elemental composition of active layer results in a Z_{eff} 55.2 (Devic *et al*, 2016) which is much larger than Z_{eff} of soft tissue (Z_{eff} = 7). The white polyester layer also presents a Z_{eff} of 27.5 (Devic *et al*, 2016) because of the Barium (Z = 56), while the other layers have a Z_{eff} close to 6 (Devic *et al*, 2016). These characteristics indicate that the high response at radiological photon energies is obtained at the price of losing the tissue equivalence which characterizes the radiochromic film for radiotherapy applications, such as EBT series. Indeed. Xr-QA2 films are used clinically only for quality assurance in radiology setups.

The change in optical reflectance of the film increases with increasing doses of ionizing radiation, particularly in the red part of its optical reflection spectrum. The film requires digitization using a reflective densitometry due to the incorporation of the white polyester film layer, although optical film scanning via transmission densitometry has also been reported for this film model (Giaddui *et al*, 2012).
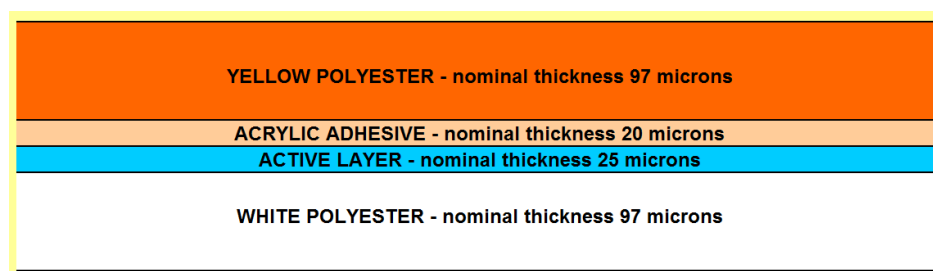
Figure 1.4: Structure of Gafchromic® XR-QA2 (Di Lillo, 2014 - Private communication by Dott. Lewis, independent consultant formerly employed by Ashland)

Table 1.2: Nominal thickness, density, elemental compositions by atoms for each layer of the Gafchromic XR-QA2. (Di Lillo, 2014 - Private communication by Dott. Lewis, independent consultant formerly employed by Ashland)

Layer	Nominal thickness (µm)	Density (g/cm²)	Composition (Atom %)							
			H	Li	C	N	O	S	Ba	Bi
Yellow Polyester Film	97	1.35	36.36	0	45.45	0	18.18	0	0	0
Acrylic adhesive	20	approx. 1.2	33.33	0	57.14	0	9.52	0	0	0
Active layer (assumes 7.5% moisture)	25	approx. 3.9	56.34	1.00	27.64	1.60	11.72	0	0	1.70
White polyester film base	97	approx. 1.6	33.80	0	42.25	0	21.55	1.20	1.20	0

The evaluation of the energy dependent dose response of XR-QA2 has been reported by Tomic *et al.* (2014), covering a broad range of effective beam energies from 12.7 to 56.3 keV (half value layer, HVL, from 0.16 to 8.25 mm Al), corresponding to beam qualities used in diagnostic radiology examinations. Those authors reported a significant variation (close to 190%) in XR-QA2 film response in that energy range, at the value of 80 mGy air kerma in air, a finding that motivates further investigations. In addition, Tomic *et al.* (2014) reported on the characterization of XR-QA2 film calibration curve by testing three fit functions (rational, linear exponential, and power); the power function was evaluated as the most appropriate for expressing the dose vs. net optical reflectance curve, for reference radiochromic dosimetry with XR-QA2 films. We reported a characterization for monochromatic X-ray beams with a synchrotron radiation (SR) source (at 28, 35, 38 and 40 keV photon energy), using a logarithmic function to express the functional dependence between air kerma in air and net variation in optical reflectance (Di Lillo et al, 2015); the logarithmic function was proposed in Tomic *et al.* (2014) for a polychromatic beam. The issue of the optimal fit function for the dose response curve of XR-QA2 films exposed to monochromatic X-rays beam is still to be investigated: indeed, error uncertainty analysis for calibration curve fitting of radiochromic films is necessary for establishing the optimal trade-off between fit precision and fit accuracy. Starting from ths considerations, we exposed the XR-QA2 radiochromic films to monoenergetic X-ray beams (in the range 18–40 keV) from a SR source to assess their energy dependent response and test various dose-response fitting functions. Additionally, we extended the study to polyenergetic X-ray beams (range of effective energies from 38 to 46.5 keV – for each polyenergetic X-ray beam, effective energies were evaluated as the energy, E, corresponding to the attenuation coefficient of Aluminium, $\mu_{Al}(E)$, which provides, by means the relation $HVL = \frac{\ln 2}{\mu_{Al}(E)}$, an HVL equal to that measured).

Film Irradiation and digitization

The measurements with the monochromatic beam were performed at the SYRMEP beamline of ELETTRA with a laminar SR beam of transverse size 16 cm × 0.335 cm (H × V). In order to evaluate the best fit function for the dose response curve of the

films, pieces of film were irradiated by the SR beam to various air kerma, K_{air}, values in the range 1–20 mGy. The film pieces (30 mm×50 mm) were cut from a single sheet (lot no. 01311401) and irradiated free-in-air in a plane transverse to the beam at the same distance from the x-ray source where the air kerma measurements with the ionization chamber were performed. In order to obtain a uniform film exposure over its height of 50 mm, the film was translated across the 3.35-mm beam size along the vertical direction, at a constant speed (Brown *et al*, 2012). Calibration curves were created for 20, 30, and 38 keV photon energies. In order to assess the energy dependent response of the radiochromic film, film pieces were irradiated at beam qualities from 18 to 40 keV with energy step of 1 keV, to a nominal air kerma of 10 mGy. Actually, the experimental air kerma obtained in each exposure was slightly different from the nominal value, with an average value of 10.26 mGy, a maximum variation in the range 9.87–10.50 mGy, and a standard deviation of 0.18 mGy.

For polychromatic beam irradiation of the XR-QA2 film, a microfocus X-ray tube was used (Hamamatsu mod. L8121-03), at tube voltages of 80 kV, 100 kV or 120 kV, with HVLs (measured in narrow beam geometry and using 99.99% pure Al foils) as given in Table 1.3. The tube operated at constant voltage with a ripple of about 0.1%. The film pieces were positioned free-in-air at the same position where the ionization chamber was placed during air kerma measurement. The latter was acquired with the pencil chamber positioned along the vertical direction (anode-cathode axis) at 400 mm from the focal spot. Temperature, pressure and beam quality corrections were applied. For film calibration, nine air kerma values were selected in the range 5–100 mGy. At each air kerma value, three film pieces (30×30 mm^2) were irradiated, cut from a single sheet (lot no. 01311401).

Table 1.3: Characteristics of polychromatic beams used for film irradiation. (from Di Lillo *et al*, 2016a)

Tube Voltage (kV)	Effective energy (keV)	HVL (mm Al)
80	38	4.03
100	43	5.25
120	46.5	6.09

A flatbed scanner (Epson Perfection V750 Pro, EPSON Scan readout software) was used in reflectance mode for scanning films with an image resolution of 96 dpi without color correction factors or filters. The images were saved as tagged image file format (TIFF) files in 48-bit RGB mode. Each scan was repeated five consecutive times after a first preview acquisition. The scanner warm-up response was stable after the third scan, and the average over the last three acquisitions was analysed (Menegotti *et al*, 2008, Devic *et al*, 2005).The film response analysis was performed by using the open software ImageJ 1.49n (National Institutes of Health, Bethesda, MD) (Abramoff *et al*, 2004). Following Tomic *et al* (2010, 2014), the response of the film was evaluated in terms of reflectance change, ΔR, in the 16-bit red channel of the RGB image, defined as:

$$\mathbf{\Delta R} = \frac{\mathbf{1}}{\mathbf{2^{16}}} [\mathbf{PV_{Before}} - \mathbf{PV_{After}}] \tag{1.1}$$

By error propagation, the corresponding uncertainty $\sigma_{\Delta R}$ was calculated:

$$\boldsymbol{\sigma_{\Delta R}} = \frac{\mathbf{1}}{\mathbf{2^{16}}} \sqrt{\left(\boldsymbol{\sigma_{PV_{Before}}}\right)^{\mathbf{2}} + \left(\boldsymbol{\sigma_{PV_{After}}}\right)^{\mathbf{2}}} \tag{1.2}$$

where: $(PV_{Before}, \sigma_{PV_{Before}})$, $(PV_{After}, \sigma_{PV_{After}})$ are the mean pixel value and standard deviation, respectively, estimated before and after the exposure, in a Region of Interest (ROI) of size 10 mm × 10 mm; the statistical uncertainty due to scanner response repeatability calculated as the standard deviation of the three scans of a film (Rampado *et al*, 2006) was also evaluated. A film not exposed was used as control film in order to quantify any reflectance change due to effects different from the X-ray exposure. After determining the change of reflectance for this control piece, $\Delta R^{control}$, by means equation 1.1, the net reflectance ΔR can be calculated:

$$net \, \Delta R = \Delta R - \Delta R^{control} \tag{1.3}$$

with an uncertainty, $\sigma_{net\Delta R}$:

$$\boldsymbol{\sigma_{net\Delta R}} = \frac{\mathbf{1}}{\mathbf{2^{16}}} \sqrt{\left(\boldsymbol{\sigma_{PV_{\Delta R}}}\right)^{\mathbf{2}} + \left(\boldsymbol{\sigma_{PV_{\Delta Rcontrol}}}\right)^{\mathbf{2}}} \tag{1.4}$$

Dose-response fitting curve

The XR-QA2 radiochromic film based dosimetry system was calibrated in terms of net reflectance within the ROI versus the air kerma measured in air at the plane where the film was positioned. By using the graphics and analysis software Origin 9 (OriginLab Corporation, Northampton, MA), the four different functions proposed in literature for this for polychromatic beams were investigated for fitting the calibration data points (Tomic *et al*, 2010, 2014):

- Rational function: $y = \frac{ax}{1+bx}$;
- Exponential function: $y = ax\, e^{mx}$;
- Power function: $y = ax + bx^n$;
- Logarithm function: $y = a + \frac{bx}{\ln x}$.

The adequacy of the various fitting functions was tested using the dose uncertainty analysis. Following Devic *et al.* (2004), for each function, the total dose uncertainty was calculated as:

$$\sigma_y^2 = \sum_i \left(\frac{\partial y}{\partial x_i}\right)^2 \cdot \sigma_{x_i}^2 \tag{1.5}$$

where σ_y is the total estimated uncertainty (standard deviation) for a dose determined with one of the fit functions and σ_{x_i} represents the standard deviations for the net reflectance ($\sigma_{net\Delta R}$) and the fitting parameters. Thus, the overall dose uncertainty consists of two terms: a term from the experimental uncertainty and another term due to the fitting process and its parameters determined during film calibration. The experimental uncertainty comprised sources including measurements reproducibility, scan reproducibility, film and scanner non-uniformity, temporal and thermal mismatch of the film pieces, differences in average response values between different film pieces, and stochastic nature of dose deposition (Devic et al, 2004). Moreover, the average of the absolute errors was calculated. The absolute error was calculated as the difference between delivered and measured air kerma value obtained by the conversion of *netΔR* using calibration

curve. Table 1.4 and Table 1.5 show the results of the analysis of the best fitting function in terms of average absolute errors and reduced chi-square of the fit.

Table 1.4: Average absolute error for each calibration curve function. The absolute error is the difference between calculated and delivered air kerma. (from Di Lillo *et al*, 2016a)

Fitting curve type	Average absolute error (%)				
	Monochromatic beam			Polychromatic beam	
	20 keV	*30 keV*	*38 keV*	*80 kV*	*120 kV*
Rational	3.75	6.65	7.15	2.03	3.04
Exponential	3.90	6.97	7.64	5.57	2.91
Power	3.59	5.46	5.07	3.89	3.36
Logarithm	7.25	8.45	6.10	5.27	2.48

Table 1.5: Reduced chi-square of the fitting procedure of dose response data. (from Di Lillo *et al*, 2016a)

Fitting curve type	Reduced chi-square				
	Monochromatic beam			Polychromatic beam	
	20 keV	*30 keV*	*38 keV*	*80 kV*	*120 kV*
Rational	2.06	4.75	7.05	0.71	1.06
Exponential	2.18	4.97	7.69	3.37	1.14
Power	2.02	3.24	4.25	1.78	1.17
Logarithm	7.39	7.28	3.20	3.44	0.93

Figure 1.5 and Figure 1.6 show the calibration curves and the one sigma dose uncertainty as a function of air kerma, for the radiochromic films irradiated with monochromatic (Figure 1.5) or polychromatic x-ray beams (Figure 1.6). In particular, Figure 1.5b and Figure 1.6 b show the one-sigma relative uncertainty of the measured dose together with the corresponding fitting error and experimental uncertainties, for monochromatic and polychromatic beams, respectively.
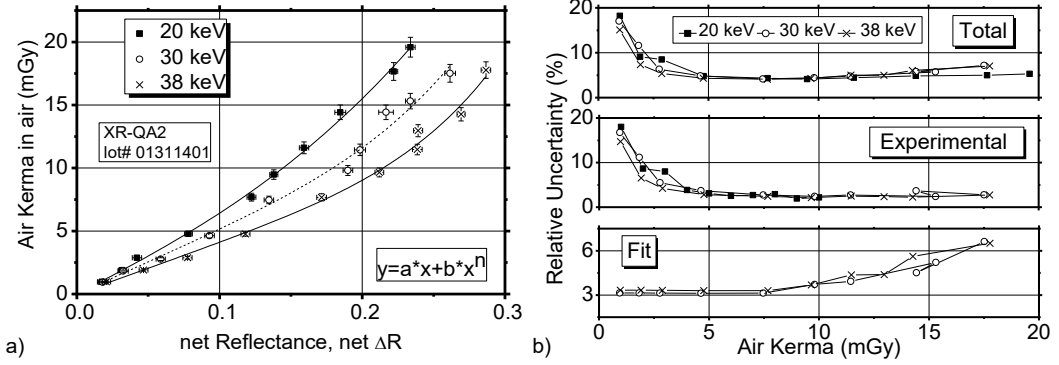
Figure 1.5: a) Dose response curves evaluated for XR-QA2 radiochromic film irradiated with monochromatic beam at photon energies of 20, 30, 38 keV. The experimental data were fitted with the power function whose formula indicated on the graphs. b) Total one-sigma relative dose uncertainty and corresponding fitting and experimental uncertainties as a function of air kerma. (from Di Lillo *et al*, 2016a)
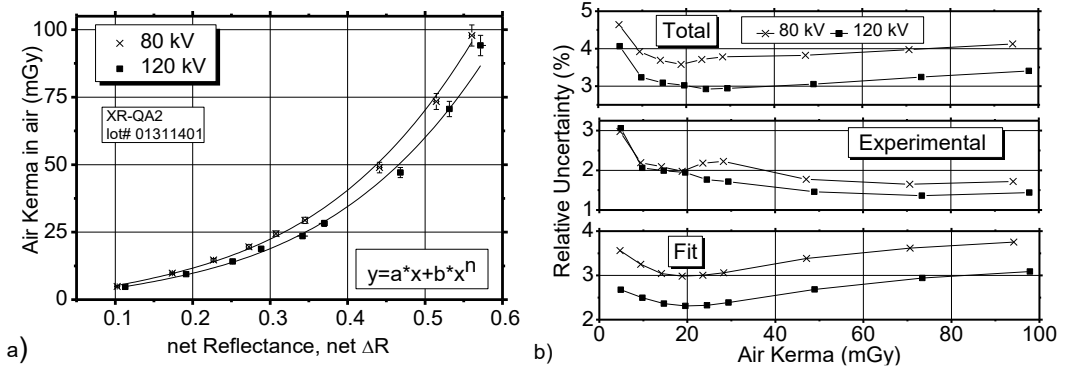
Figure 1.6: a) Dose response curves evaluated for XR-QA2 radiochromic film irradiated with polychromatic beam at tube voltage of 80, 120 kV. The experimental data were fitted with the power function whose formula indicated on the graphs. b) Total one-sigma relative dose uncertainty and corresponding fitting and experimental uncertainties as a function of air kerma. (from Di Lillo *et al*, 2016a)

The power function gives a total uncertainty of less than 6% above 6 mGy of air kerma at 20 and 30 keV, as well as above 3 mGy at 38 keV (Figure 1.5b); for polychromatic irradiation, the relative uncertainty is less than 5% in the whole air kerma range (Figure 1.6b). Moreover, the evaluation of the average absolute error indicates a global fit accuracy within 5%.

The four fitting functions reported by Tomic *et al.* (2012, 2014) for reference radiochromic film dosimetry protocol with a polychromatic X-ray source can also fit the experimental data obtained with a monochromatic X-ray source. In our work, the uncertainty analysis and absolute error study show that in the range of monochromatic or effective energies 20−46.5 keV, the power function provides the

best agreement between fit precision (evaluated via uncertainty analysis) and fit accuracy (assessed via average air kerma absolute error). This finding is in agreement with that carried out by Tomic *et al*. (2014), for the same radiochromic film irradiated with polychromatic X-ray beams in the range 50−140 kV (12.7−56.3 keV beam effective energy).

Energy dependence

A first evaluation of the energy dependent response was performed by comparing the dose-response curve of the XRQA2 film for monochromatic and polychromatic beam irradiations (Figure 1.7a). For photon or effective energy from 20 to 38 keV, there is an increasing vertical shift of the response curve toward lower dose values, while the response curve at 120 kV shows a reversal of this trend with a vertical shift toward higher dose with respect to the curve at 80 kV. An accurate assessment of the energy dependent response of film can be carried out by evaluating the sensitivity of the film at each photon energy defined as the ratio between the change in radiochromic film response and the actual dose, which caused this change. Figure 1.7b shows the sensitivity of the radiochromic film as a function of photon energy (monochromatic beam, open square data symbols) or of effective energy (polychromatic beam, filled circle symbols). The sensitivity of the film under monochromatic irradiation increases with increasing energy in the range 18–39 keV, with a maximum variation of about 170% calculated as the ratio between the maximum and the minimum sensitivity values in this energy range. For polychromatic irradiation, the data show a variation of 118% in the film response with the increment of the effective energy beam in the range 38–46.5 keV. This variation was calculated as the ratio between the sensitivity values at effective energies of 38 keV (0.02098 mGy^{-1}) and 46.5 keV (0.01774 mGy^{-1}). For comparison, Tomic *et al* (2014) showed a significant variation of the film response of about 120 % at 80 mGy in the effective energy range 18−39 keV.
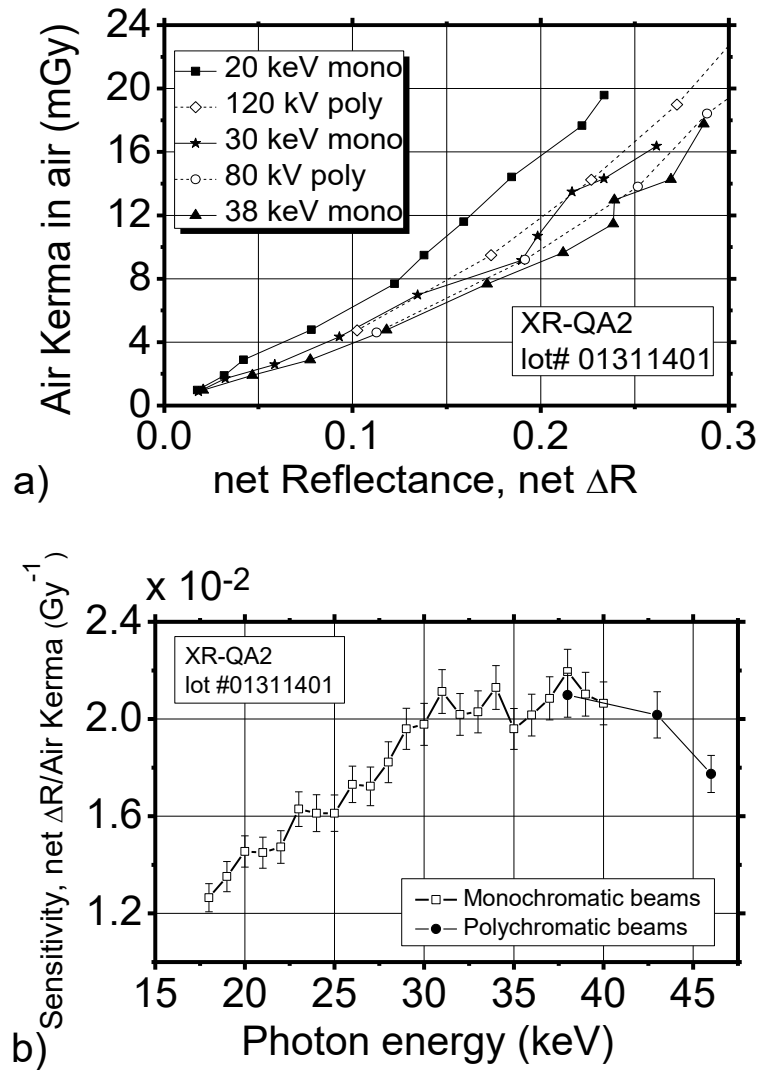
Figure 1.7: a) Dose response curves of XR-QA2 film irradiated with a monochromatic (mono) beam at 20, 30, and 38 and with a polychromatic (poly) beam at 80 and 120 kV. b) Film sensitivity as a function of energy (or effective energy) for monochromatic and for polychromatic irradiation. (from Di Lillo *et al*, 2016a)

Comparison with literature data

A comparison between the dose-response curves obtained in this work and curves reported by Tomic *et al* (2014) and Giaddui *et al* (2012, 2013) at 120 kV for the same film type and comparable values of the beam HVLs is shown in Figure 1.8. In this graph, data by Tomic *et al* (2014) and Giaddui *et al* (2013) show a remarkable agreement; on the other hand, data by Giaddui *et al* (2012) for the same film type show a marked under-response (14%–38%, average value 34%, calculated as percent relative difference in response), while data in this work indicate an over-response

24

with respect to published data (Tomic *et al*, 2014, Giaddui *et al*, 2012,2013). In particular, we evaluated an over-response of XRQA2 radiochromic film in the range 24%–27% (average value, 26%) with respect to data by Tomic *et al*. (2014). A maximum difference of 55% was observed (data in this work with respect to the work of Giaddui *et al*. (2013)). These discrepancies point toward a significant batch-to-batch variation in the response of the XR-QA2 film for this beam quality (120 kV, HVL 6 mm Al). This could be attributed to differences in chemical composition of sensitive and adhesive layers among various batches, regarding the lithium concentration (Private communication by Dott. Lewis, independent consultant formerly employed by Ashland). In favour of this explanation, it is worth noting that Giaddui *et al* (2012, 2013) found two completely different dose response curves for the same film batch. If different scanners are used for film digitization for the same film manufacturer and model, this difference might also contribute, at least in part, to a different response curve for the same film batch. The differences may arise from scanner lamp aging, scanner mechanics, and variation in the readout noise. One of the ways to check for the presence of this specific source of bias in the derivation of the film dose response, and to correct it, is the use of a scanner optical calibration procedure based on a grey scale step wedge prior to the film calibration procedure.
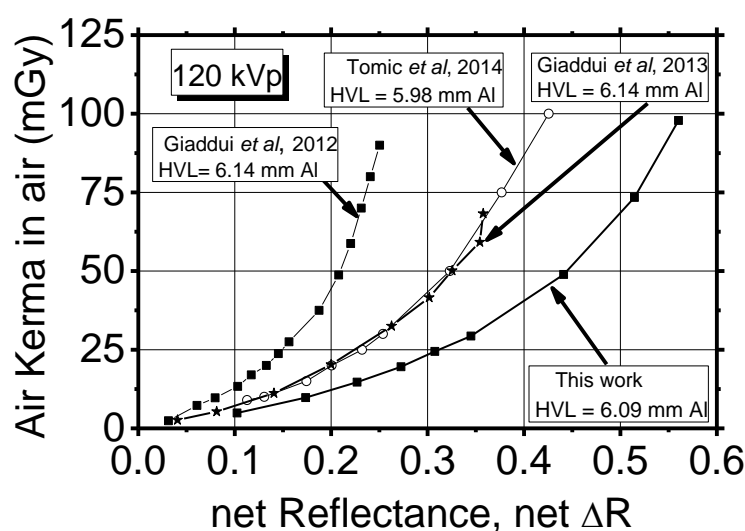
Figure 1.8: Dose response curve of the XR-QA2 radiochromic film irradiated with a polychromatic source at 120 kVp, obtained by Tomic *et al*. (2014) (lot # A07091204), Giaddui *et al*. (2012,2013) (lot # A04280904A) and in this work (lot # 01311401). (from Di Lillo *et al*, 2016a)

1.2.1.2 Characterization of GR-200A thermoluminescence dosimeters

Thermoluminescence dosimeters (TLD) are usually used for personnel, environmental and clinical dosimetry. They were produced, for the first time, in powder form by Nakajima *et al* (1978), by doping LiF with Mg, Cu and P impurities. Presently, there are several companies that manufacture LiF:Mg,Cu,P dosimeters such as Solid Dosimetric Detector & Method Laboratory in Beijing, China (type GR-200), Nemoto in Japan (type NTL-500), Institute of Nuclear Physics in Poland (type MCP-N) and by Thermo Scientific in USA (type TLD-100H, TLD-600H,TLD-700H) (Bos, 2001). TLD is a dosimeter with a good tissue equivalence – Bacci *et al* (1993) reported for GR-200A dosimeter a Z_{eff} between 7 and 8 – high sensitivity, linear dose response, low fading rate and low residual signal (Shen *et al*, 2002). However, data reported in literature show a strong dependence of their response on the photon energy, due to the influence of the concentration of dopants and the spatial distribution of the energy deposition events (Horowitx, 1984). For x-rays, the photon ionization density, expressed by mean linear energy or by Linear Energy Transfer (LET), varies with photon energy because of changes in secondary electron spectra. LiF:Mg,Cu,P shows an anomalous response to low-energy x-rays (< 100 keV), due to its high dependence on LET: small changes of this (due to the gradual transition of x-ray interaction from predominantly photoelectric effect to Compton scattering (Olko *et al*, 1993)) lead to observable change in the response. Kron *et al* (1998) studied the energy response of various radiation detectors (including LiF:Mg,Ti and LiF:Mg,Cu,P TLD dosimeters) to monoenergetic and polyenergetic photons and proved that irradiation with monoenergetic beams permits to avoid the compounding effect of the spectral distribution of x-rays from conventional sources. They also showed an enhancement up to about 50% of the LiF:Mg,Ti response to monoenergetic photon beams in the energy range 10-100 keV, with respect to 6 MV spectral x-rays from a medical linear accelerator. On the other hand, the response for LiF:Mg,Cu,P was close to the 6 MV response, considering the experimental uncertainties, with some over-response up to about 20% at energies around 25 keV (Figure 1.9).
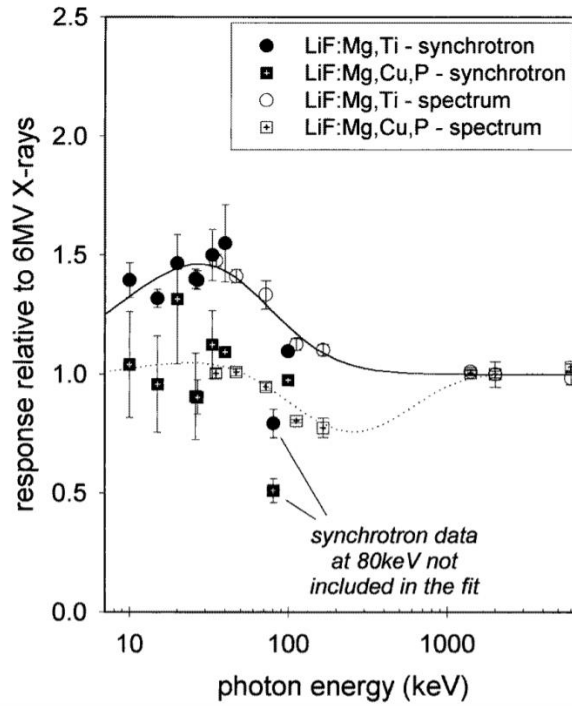
Figure 1.9: Response of LiF:Mg,Cu,P TLDs to monochromatic synchrotron radiation and X-ray spectrum, relative to 6 MV X-ray beam from a medical linear accelerator. (from Kron *et al*, 1998)

Using monoenergetic synchrotron radiation (SR), Duggan *et al* (2004) irradiated LiF:Mg,Cu,P TLDs from two manufacturers (MCP-N, Poland; GR-200 series, China) and LiF:Mg,Ti (GR-100, China) in the range 10-26 keV. Their results confirmed both qualitatively and quantitatively those of Kron *et al* (1998), showing an increased response up to a factor of 1.5 for LiF:Mg,Ti and a response close to unity for LiF:Mg,Cu,P, relative to 6 MV irradiation. Their experimental findings confirmed the model prediction of Kron *et al* (1998).

We investigated the energy response of the cylindrical LiF:Mg,Cu,P TLDs (type GR-200A, Solid Dosimetric Detector & Method Laboratory, Beijing, China) of 4.5 mm diameter and thickness of 0.8 mm in the energy range 18–40 keV following the same protocol which we reported in Emiro *et al* (2015). The annealing of TLD was obtained by heating it at 235°C for 20 minutes. A Thermo Scientific™ Harshaw TLD™ Model 4500 reader was employed to read the dosimeter. The reading procedure consisted of heating the sample to a temperature of 240° with a linear ramp of 8 °C/s without pre-heat step.

First, the response of GR-200A TLDs to the irradiation with a ^{60}Co source with known calibrated activity was calibrated in terms of air kerma. Dosimeters were

27

placed in a PMMA phantom at a depth of 5.07 mm to provide charged particle equilibrium. The distance from source was 1m. The exposure time was tuned in order to obtain three different air kerma levels. A linear calibration curve was used for fitting the experimental data (air kerma in mGy vs. corresponding reading in nC).

The measurements for the evaluation of energy response were acquired at SYRMEP beamline of ELETTRA. A SR beam of size 15 cm × 0.34 cm (H × V) irradiated the dosimeter free-in-air at energy in the range 18–40 keV, with a step of 1 keV. The circular section of dosimeter was in the plane transverse to the direction of the beam propagation. A uniform exposure of TLD dosimeter was obtained by translating across the beam along the vertical direction. At each energy, four TLD were irradiated at a nominal air kerma of 10 mGy. The calibrated ionization chamber measured the real air kerma free-in-air during the irradiations.

We calculated the air kerma relative response of each TLD, R_n, as:

$$R_n = \left(\frac{K_{Co60}^{air}}{K_{SR}^{air}} \right)_n \tag{1.6}$$

where $\left(K_{SR}^{air} \right)_n$ is the air kerma in the SR beam, measured with the ionization chamber and $\left(K_{Co60}^{air} \right)_n$ represents the air kerma in the ^{60}Co reference beam that would give the same reader output T_n obtained with SR beam. K_{Co60}^{air} was estimated by means of linear calibration curve:

$$\left(K_{Co60}^{air} \right)_n = s_n \cdot T_n \tag{1.7}$$

where s_n is the slope of the calibration curve. Relative uncertainty in this value was estimated by propagating the uncertainties on calibration parameters.

Uncertainty on R_n, $\sigma(R_n)$, was estimated by propagating the uncertainties on $\left(K_{Co60}^{air} \right)_n$ and on measured air kerma $\left(K_{SR}^{air} \right)_n$:

$$\sigma_{R_n}^2 = \left(\frac{T_n}{K_{SR}^{air}} \right)^2 \cdot \sigma^2(s_n) + \left(\frac{K_{Co60}^{air}}{\left(K_{SR}^{air} \right)^2} \right)^2 \cdot \sigma^2\left(K_{SR}^{air} \right) + \left(\frac{s_n}{K_{SR}^{air}} \right)^2 \cdot \sigma^2(T_n) \tag{1.8}$$

In equation 1.8, $\sigma(s_n)$ is the uncertainties on slope of the calibration curve of the nth dosimeter calculated using the least mean square method. $\sigma\left(K_{SR}^{air}\right)$ is the uncertainty on K_{SR}^{air} $\sigma(T_n)$ was evaluated with repeated measure on a single TLD and it is about 2%.

At each energy, the average air kerma response (R_E) was calculated as the weighted mean, with weights w_n and weighted standard deviation σ_R, of the air kerma response, R_n, of TLDs exposed to that energy:

$$R_E = \frac{\sum_n w_n \cdot R_n}{\sum_n w_n}; w_n = \frac{1}{\left[\sigma(R_n)\right]^2}; \sigma_{R_E} = \frac{1}{\sqrt{\sum_n w_n}} \tag{1.9}$$

Following (Olko et al., 1999), we evaluated the theoretical trend of relative response as:

$$R_{E,corr} = \frac{\mu'_E}{\mu'_{Co60}} \cdot \frac{F_C^E}{F_C^{Co60}} \cdot \frac{F_L^E}{F_L^{Co60}} \tag{1.10}$$

which takes into account light self-absorption F_L^E and attenuation of X-rays F_c^E in the TLD. The attenuation correction factor at energy E, F_c^E, was defined as:

$$F_c^E = \frac{1 - e^{-\frac{\mu_{en}}{\rho}\rho d}}{\frac{\mu_{en}}{\rho}\rho d} \tag{1.11}$$

where d is the thickness of the dosimeters and μ_{en}/ρ and ρ are the mass energy absorption coefficient and the density of LiF:Mg,Cu,P, respectively, for photons of energy E, calculated with the software XMuDat (Nowotny, 1998).

The light correction factor at energy E, F_L^E, was calculated according the following expression:

$$F_L^E = \frac{\left[1 - e^{\left(-\frac{\mu_{en}}{\rho} + \mu_l\right)\rho d}\right]\left(\frac{\mu_{en}}{\rho}\right)\rho}{\left[1 - e^{\left(-\frac{\mu_{en}}{\rho}\right)\rho d}\right]\left(\frac{\mu_{en}}{\rho} + \mu_l\right)\rho} \tag{1.12}$$

where μ_l is the light absorption coefficient.

Figure 1.10 shows the air kerma response of GR-200A TLDs to monochromatic SR in the energy range 18–40 keV, relative to the response to ^{60}Co γ-rays. The

continuous line represents the theoretical trend of the relative response, calculated according to equation 1.10. The following TLD composition by weight was used for the calculation (Olko et al., 1999): fluorine 0.7252, iodine 0.2648, magnesium 0.0019, phosphorus 0.0069, copper 0.00121. A comparison between data in this work and data from Kron *et al* (1998) and Bakshi *et al* (2010), and data from Gonzalez *et al* (2007) and Emiro *et al* (2015) is also shown in Figure 1.9. It is to be noted that normalization is for 6 MV X-rays in Kron *et al* (1998), and for [60]Co γ-rays in Bakshi *et al* (2010), Gonzalez *et al* (2007), Emiro *et al* (2015) and in the present study.
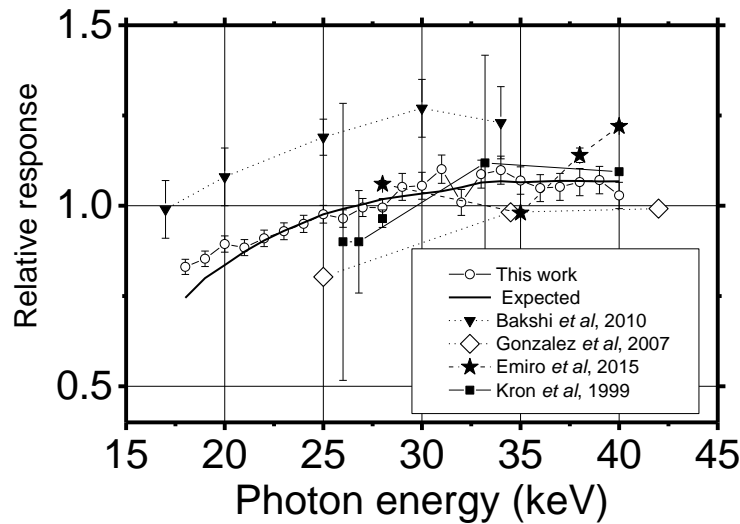
Figure 1.10:Comparison of energy response of LiF:Mg,Cu,P reported in this work and energy response reported in (Kron *et al* ,1998), (Bakshi *et al*, 2010), (Gonzalez *et al*, 2007). Note that Kron *et al* (1998), and in this work, LiF:Mg,Cu,P TLDs produced in China as GR-200A were studied. Bakshi *et al* (2010) investigated the LiF:Mg,Cu,P produced in Poland and commercially sold as MCP-100. Data from in Kron *et al* (1998) are normalized to the response to 6 MV x-rays, while data in the present work and in (Bakshi *et al*, 2010), (Gonzalez *et al*, 2007) are relative to [60]Co γ-rays. The calculated response follows from eq. 1.10 in the text.

Data of this work show an increment of the relative response from 0.8 at 18 keV to 1.05 at 32 keV. For energies higher than 32 keV, a constant relative response of about 1.05 is observed. Martella in an application note shows similar result with a maximum of TLD response around 40 keV. This behaviour agrees with the expected trend estimated via equation 1.13. Our previous data published in (Emiro *et al*, 2015) suggested an over-response of LiF:Mg,Cu,P GR-200A dosemeters (produced in China) with respect to ^{60}Co in the range 28-40 keV. This agrees with the results obtained in this work. However, a different behaviour was observed. In Emiro *et al*

(2015), we indicated a dip in the trend of the air kerma response vs. photon energy from 28 to 40 keV, which is considered significantly above the experimental error. On the other hand, the expected response showed a smooth trend. The measurements reported in this PhD work revealed a behaviour following the smooth trend of theoretical response without any dip. We want to highlight that different procedure for the ionization chamber calibration were employed. In Emiro *et al* (2015), the ionization chamber was calibrated in terms of air kerma with reference to the IOC chamber of SYRMEP in the whole range. However, the reference chamber was not calibrated in the energy range of interest. As already illustrated, in this thesis, we employed the IOC chamber as reference only in its calibration range (18−28 keV), while the beam quality correction factor provided by manufacturing was applied in the range (29−40 keV). For reference, we compared the air kerma measured with the IC at 28 keV using the IOC chamber calibration factor and the manufacture calibration factor. We evaluated values of 10.60 mGy using the calibration factor from the reference IOC chamber and 10.93 mGy taking into account the beam quality correction factor from manufacture. The relative difference of about 3% within the measurement uncertainty. Data in the literature for the response of GR-200A TLDs to low-energy monochromatic x-rays refer to few studies. Bakshi *et al* (2010) measured the energy response, R, of MCP-100 LiF:Mg,Cu,P relative to ^{60}Co and showed that there is a decrease from $R = 1.0$ to $R = 1.23$ (data interpolated from figure 10 in (Bakshi *et al*, 2010)) in going from 16 to 34 keV for SR monochromatic x-rays. In comparison, for those dosemeters, their Monte Carlo simulations indicated values (corrected for the detection efficiency of TLD material) between 0.95 and 1.10 for the relative response, at 30 keV and 34 keV, respectively. Gonzalez *et al* (2007) presented the relative (to ^{60}Co) energy response of GR-200A dosemeters produced in China, exposed to x-rays from x-ray tubes operated at tube potential in the range 30-250 kV. The corresponding data points in Figure 1.9 refer to their data at beam effective energies of 24, 34.5 and 42 keV, for which the estimated uncertainty on the response is 4%. Their data have a maximum value of 1 (i.e., equal response to ^{60}Co) at effective energies between 34 and 42 keV and decrease both at lower and higher energies, so showing an under-response of GR-200A of 20% at 24

keV. It is to be noted, however, that these results refer to polychromatic X-ray spectra, while the data in this work are for monochromatic X-rays. For example, the 34.5 keV effective energy in (Gonzalez *et al*, 2007) corresponded to photon spectra extending up to 80 keV. Indeed, two different manufacturers were implied in the two sets of literature data (Kron *et al*, 1998, Bakshi *et al*, 2010). Moreover, the experimental data reported in Bakshi *et al* (2010) ($R \cong 1.25$) are not consistent (within the experimental uncertainties) with the experimental data of Kron *et al* (1998) ($R \cong 1$). On the other hand, GR-200A exposed to x-ray tube radiation show an under-response in this range of effective energies (Gonzalez *et al*, 2007). This could be an indication of a material-specific and manufacturer-specific air kerma response of LiF:Mg,Cu,P TLDs in the low energy range explored in the present study, where significant deviations from $R \cong 1$ (i.e., from the response to ^{60}Co) have been observed with monochromatic irradiation between 28 and 40 keV.

1.2.2 Breast and Phantom dosimetry

My work for breast and phantom dosimetry included also the validation of the MC simulations (developed within SYRMA-CT collaboration) for estimation of the MGD in a breast CT exam with SR. The validation was performed by measurements of absorbed dose in phantoms. This work resulted in the publication of the following paper in international scientific journals. Here, we describe this work as illustrated in the corresponding paper.

- Mettivier G., Fedon C., Di Lillo F., Longo R., Sarno A., Tromba G. & Russo P. (2016) Glandular dose in breast computed tomography with synchrotron radiation. *Phys. Med. Biol.* **61**(2), 569–587.
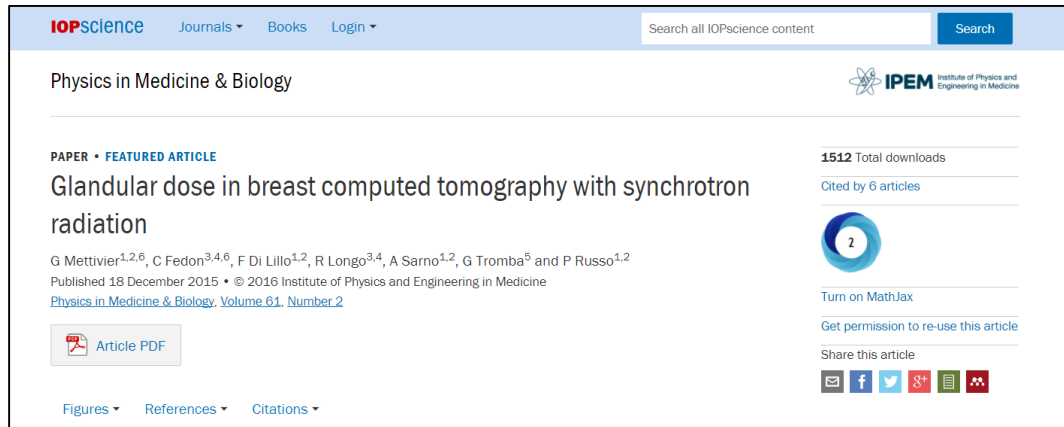
The partial breast irradiation planned by SYRMA-CT collaboration for SR-BCT calls for the specific evaluation of the glandular dose and normalized glandular dose coefficients – via Monte Carlo (MC) simulations – in cases where not all of the (glandular mass in the) breast is irradiated. This evaluation must be performed (for a given breast size, breast composition and monochromatic beam energy) by considering various heights of the total scanned section (in the longitudinal direction from chest wall to nipple), in dependence on the total height of the thick section of the breast selected for imaging. A specific dosimetric protocol of this type is needed for assessing the imaging scan procedure. The condition of partial breast irradiation is different from that of (full field) 2D mammography (Dance 1990, Wu *et al*, 1994), of DBT (Sechopoulos, 2013a, 2013b) as well as of BCT (Boone *et al*, 2001a, 2004, Thacker and Glick, 2004, Yi *et al,* 2011). In dosimetric protocols adopted for those 2D and 3D imaging techniques, the whole breast volume is irradiated and the definition of the mean glandular dose (MGD) refers to the total energy (E_g) deposited in the glandular tissue divided by the total glandular mass (M_g) of the breast (Hammerstein *et al*, 1979). However, dosimetric protocols dedicated to SR-BCT are not available yet, in cases where partial breast irradiations are performed. Indeed, the above protocols, if based on the calculation of the energy e_g deposited in the glandular mass *in the partially irradiated volume* divided by the *whole glandular mass M_g* of the breast, may represent an underestimation of the MGD, since e_g is less than E_g due to the presence of scatter dose in breast regions adjacent to the irradiated volume, and the actual irradiated mass (m_g) is only a fraction of the whole mass of the breast (M_g). Hence, in the case of an irradiated section of the pendant breast

whose height is less than the full height of the breast (from chest wall to nipple), specific dosimetric evaluations are needed, for polychromatic as well as for monochromatic x-ray beams. In this study, we estimate, via Monte Carlo (MC) simulation, the breast glandular dose for a SR-BCT scan for various sizes and compositions of the pendant breast, at various energies of the monochromatic SR beam and at a fixed height of the laminar SR beam, by considering different thicknesses of the total irradiated section of the breast. This permitted to calculate also the normalized glandular dose coefficients (DgN) for given breast size and composition, at the monochromatic beam energy E, to be used for in vivo SR-BCT scans.

1.2.2.1 New dose metrics

The conventional definition of the MGD metric implies that, in the case where the whole breast volume is irradiated, MGD (mGy) is calculated from the total energy deposited (E_g) in the total glandular mass of the breast (M_g), as:

$$MGD = \frac{E_g}{M_g} \tag{1.13}$$

In an analogous way, in the case where a fraction of the breast volume is irradiated, a quantity MGD_v (mGy) can be calculated from the energy (e_g) deposited only in the glandular mass of the directly irradiated breast volume (m_g), as:

$$MGD_v = \frac{e_g}{m_g} \tag{1.14}$$

The energy e_g takes into account also energy deposits in the mass m_g from radiation scattered from regions outside the irradiated volume. However, one has to consider also the dose delivered indirectly to the glandular tissue outside the irradiated volume: this dose originates from radiation scattered to breast regions adjacent to the irradiated ones. Then, one can define a third quantity, MGD_t, as the ration between the total energy deposited in the whole breast (E_g) and the glandular mass in the irradiated volume (m_g):

$$MGD_t = \frac{E_g}{m_g} \tag{1.15}$$

where E_g is greater than e_g due to scatter dose and therefore MGD_t is greater than MGD_V. The two quantities are coincident only in the limit where the whole breast is scanned. In the axial scanning of a section of the breast in multiple successive rotations and corresponding vertical translations of the patient support, for a given width of the SR beam, MGD_V and MGD_t should be evaluated as a function of the total height of the scanned section, since the tails of the longitudinal scatter dose profiles from each axial scan overlap and sum up to determine the multiple scan average dose to the glandular tissue. If the height of the irradiated section corresponds to that of the beam (i.e. just one axial scan is performed), then the MGD_t metric is related to the notion of the computed tomography dose index (CTDI) metric in whole body CT dosimetry (Kalender, 2014). Both of metrics take into account the scatter dose, i.e. the energy deposited by the scatter radiation outside the irradiated section. Indeed, as reported in IAEA (2011), AAPM (2010), Kalender (2014), "*CTDI is defined as:*

$$CTDI_{100} = \frac{1}{NT} \int_{-50mm}^{+50mm} D(z)\, dz \qquad (1.16)$$

where T is the nominal slice thickness, N is the number of slices measured simultaneously and D(z) is the profile of absorbed dose in air originating from one axial rotation along 100 mm of a line perpendicular to the tomographic plane. The $CTDI_{100}$ is usually measured with 100-mm ionization chamber in a 15-cm height PMMA cylindrical phantom with a diameter of 16 cm (head section) or 32 cm (chest section). Phantom has one central and four peripheral holes for inserting the chamber."

1.2.2.2 *Monte Carlo code validation*

MC code was based on Geant4 toolkit 10.00 (Agostinelli *et al*, 2003). It was developed by Dr. C. Fedon, Università di Trieste, Italy, within the SYRMA-CY collaboration (Fedon, 2016). The G4EmLivermorePhysics library were used for the particle transport, according to Fedon *et al* (2015) for applications in breast dosimetry. The code was validated with a direct comparison with data extracted from the literature (Boone 2002, Boone *et al* 2004, Mittone *et al* 2014a), in terms of mammographic normalized glandular dose coefficients (DgN), and ad hoc

experimental data, in terms of CTDI. In this thesis, we show the results of the comparison with CTDI measurements. The validation with literature data is reported in Mettivier *et al.* (2015).

In order to perform the CTDI measurements, a Radcal ionization chamber (mod. 10X6-3CT) connected with the dosimeter Accu-Pro was used (Radcal, Monrovia, CA, USA). The dosimeter provides the exposure time and the air kerma value corrected for temperature, pressure and calibration factors. The ionization chamber is a cylinder with an active volume of $3cm^3$ (142-mm length, but only 100-mm active, and base area of $0.3cm^2$). The nominal energy range is from 35 to 150 keV where the accuracy is ±5% as indicated by the manufacturer. During the measurement, the phantom rotated by 360 deg with a speed of 3°/s. The measurements were carried out in four different homogeneous PMMA cylinders with a diameter of 8, 10, 12 and 14 cm and a height of 15 cm. The energy was varied from 8 to 40 keV. Figure 1.11 shows the comparison between the simulated (close symbol) and measured (open symbol) ratio of CTDI values measured in the centre of the phantom to the air kerma at the scanner isocenter. The agreement is in the order of 5%.
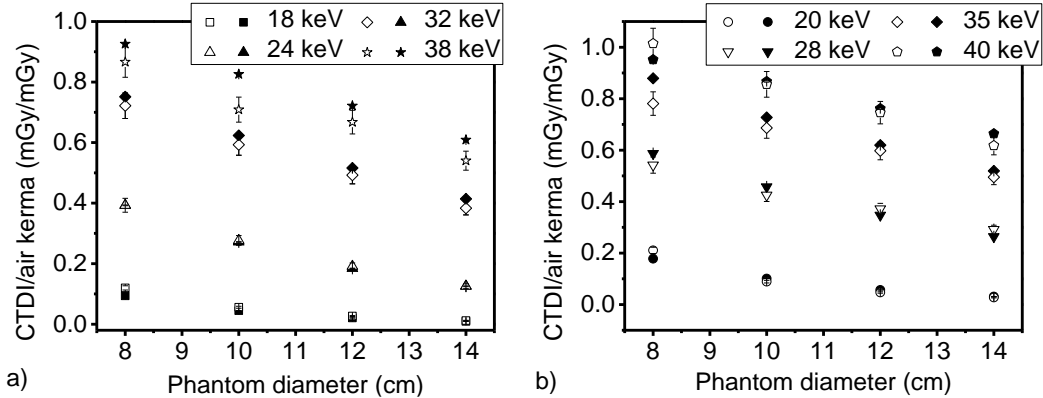
Figure 1.11: Comparison between the simulated (close symbol) and measured (open symbol) ratio of CTDI values at the center of the phantom and in air at 18, 24, 32 and 38 keV in (a) and 20, 28, 35 and 40 keV in (b). (from Mettivier *et al*, 2016)

1.2.2.3 Dose Assessment

By using the validated MC code, the dose was evaluated in cases, which matched the characteristics of the SR beam specifications. A sketch of the simulated setup is reported in Figure 1.12. The radiation field shape was a rectangular one, with a fixed

width of 15 cm and a variable dimension *w* according to the case studied. The samples had a cylindrical shape (diameter = d) with a height *h* of 1.5 times the sample's radius, as in Boone *et al* (2004), and was composed of a homogeneous mixture of adipose and glandular tissues. A water box (with a volume of 13.5 dm^3) was added for simulating the body of the patient. The skin thickness and the glandular fraction by weight used in this study were 1.45 mm (Huang *et al,* 2008, Shi *et al,* 2013) and 0%, 50% and 100%, respectively. We used the elemental composition reported in Hammerstain *et al.* (1979).
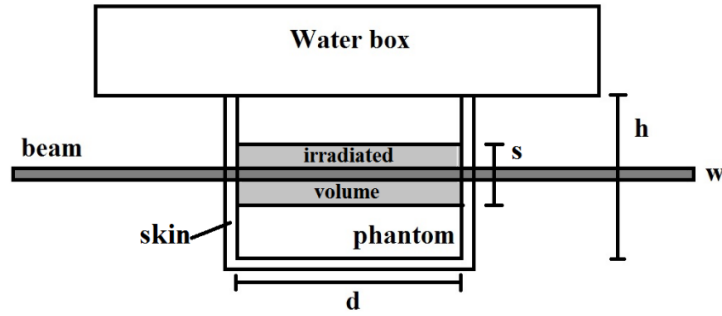
Figure 1.12: *S*ketch of the simulated setup. The radiation field shape was set with a fixed width of 150mm and a variable dimension w according to the case study. The samples had a cylindrical shape with a diameter d and a height h. The dimensions of the irradiated volume are π(d/2)^2 × s where s is variable according to the case studied. A water box (with a volume of 13.5 dm^3) was added for simulating the body of the patient. The skin thickness was 1.45 mm. (form Mettivier *et al*, 2016)

The dimensions of the irradiated volume were calculated as *π(d/2)^2* × *s* where *s* is variable according to the case studied. A CT scan simulation consisted of a rotation of the phantom from 0 to 360 deg with a 1 deg step; for each projection image up to 1 million photon histories were generated. We evaluated the dose, in terms of MGD, MGD$_V$ and MGD$_t$, in the case of partial breast irradiation fixing the height *w* of the beam to 3 mm. In this case, the vertical dimension, *s*, of the irradiated breast volume was varied from 3 to 87 mm by translating vertically the beam with a step of 3 mm. This is the case closest to the SR-BCT scan conditions in the SYRMA-CT project. The photon fluence was kept constant and the energy was varied from 8 to 50 keV at 1 keV steps. In addition, we calculated the normalized glandular dose coefficient *DgN$_{CT}$* defined as:

$$DgN_{CT} = \frac{MGD}{K_{iso}} \qquad (1.17)$$

where K_{iso} is the air kerma at isocenter. In particular, we estimated the DgN_{CT}, DgN_{CTv} DgN_{CTt} to obtain the MGD, the MGD_v and the MGD_t values, respectively, from the measurement of the air kerma at the scanner isocentre. The sample had a cylindrical shape with a diameter ranging from 8 cm up to 16 cm with a glandular fraction of 0, 50%, and 100% by weight. Since SYRMA-CT collaboration plans to irradiate a breast section of height 3 cm by translating vertically ten times the patient bed in 0.3-cm step corresponding to beam size, the DgN_{CT} values were calculated for a 3-cm high (s = 3 cm, w = 3 mm) irradiated volume.

Figure 1.13 shows the MGD whole breast, the MGD_v and the MGD_t for a 12 cm breast diameter (h = 9 cm) with a glandular fraction of 50% at a fixed energy of 38 keV (one of the energy values that will be adopted in the SYRMA-CT project) as a function of the height s of the irradiated volume. We observe a linear dependence of the MGD whole breast on the height of the irradiated volume, due to the linear increase of the deposited energy with the increasing vertical dimension of the irradiated volume. On the other hand, the MGD_v increases with a sub-linear trend with the increasing vertical dimension of the irradiated volume, because the deposited energy increases together with the glandular mass of the irradiated volume.
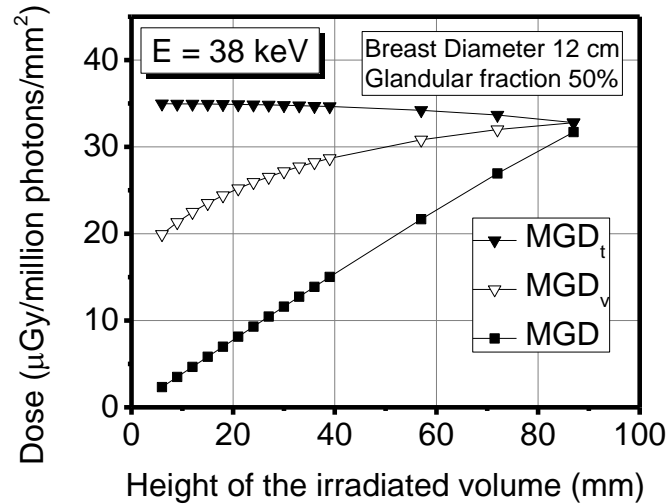
Figure 1.13: The MGD to the glandular mass present in the whole breast (solid square), or in the irradiated volume (open down triangle) or in the irradiated volume adding the contribution from scatter dose (close down triangle) for a 12-cm diameter breast phantom with a glandular fraction of 50% varying the dimension of the irradiated volume with a 3 mm-height beam. The photon energy of the monoenergetic beam was 38 keV. (from Mettivier et al, 2016)

For the MGD$_t$, the energy is deposited throughout the whole breast but the glandular mass used in the calculation of the corresponding dose is that of the irradiated volume. This dose MGD$_t$ is almost constant with a little decrease with the vertical dimension of the irradiated slice since as the irradiated area approximates the size of the entire breast, the energy delivered outside the slice is gradually smaller. The DgN$_{CT}$ in the case s = 3 cm with a w = 0.3 cm height beam is reported in Figure 1.14, Figure 1.15 and Figure 1.16. Figure 1.14 (a)–(c) show the DgN$_{CT}$ coefficients, which will be used to calculate the MGD to the whole breast for a breast diameter from 8 to 16 cm at 0%, 50% and 100% glandular fraction, respectively. Figure 1.15 (a)–(c) and Figure 1.16 (a)–(c) show the DgN$_{CTv}$ and DgN$_{CTt}$ coefficients, needed for calculating the MGD$_v$ and MGD$_t$ for a slice of 30mm height (breast diameter varied from 8 to 16 cm, glandular fraction of 0%, 50% and 100%, respectively).
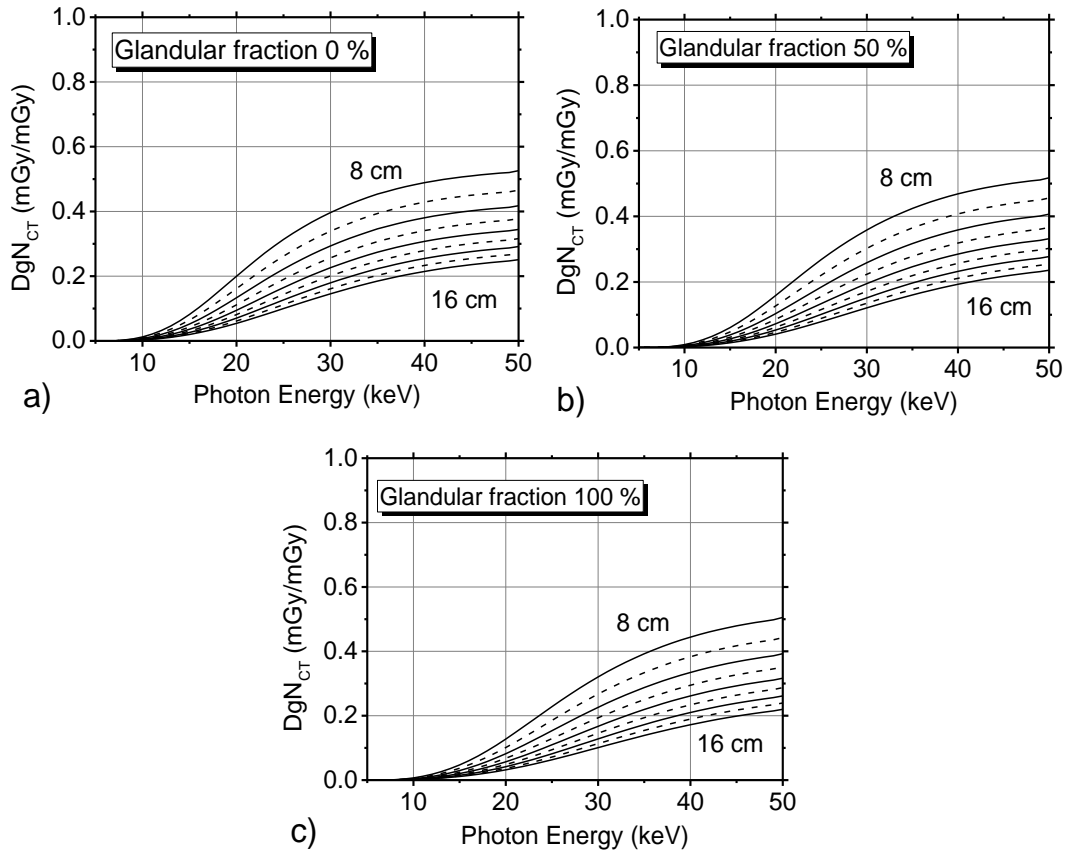
Figure 1.14: DgN$_{CT}$ coefficients to calculate the *MGD* (a, b, c) in the case of a 3 mm-height beam irradiating a 30 mm-height slice for a breast diameter from 8 to 16 cm in 1-cm step, and a glandular fraction of 0% (a), 50% (b) and 100% (c). The energy was varied from 8 to 50 keV with 1 keV step; data were represented as lines for ease of visualization. (from Mettivier *et al*, 2016)

All DgN coefficients - DgN$_{CT}$, DgN$_{CTv}$ and DgN$_{CTt}$ – increase by increasing the photon energy of the incident beam, and they decrease by increasing the breast diameter at the chest and by increasing the glandular fraction. Moreover, DgN$_{CT}$, DgN$_{CTv}$, DgN$_{CT}$ values increase up to 0.5 mGy/mGy, to 0.9 mGy/mGy and 1.0 mGy/mGy, respectively. For fixed air kearma, these values produce low level of MGD for the partial breast irradiation and higher value of MGD$_t$ and MGD$_v$. This behaviour indicates that the use of the parameter MGD could produce an underestimate of the risk from radiation in the case of partial irradiation, because the energy deposition occurs in a limited area of the organ resulting in a higher absorbed dose in that area.
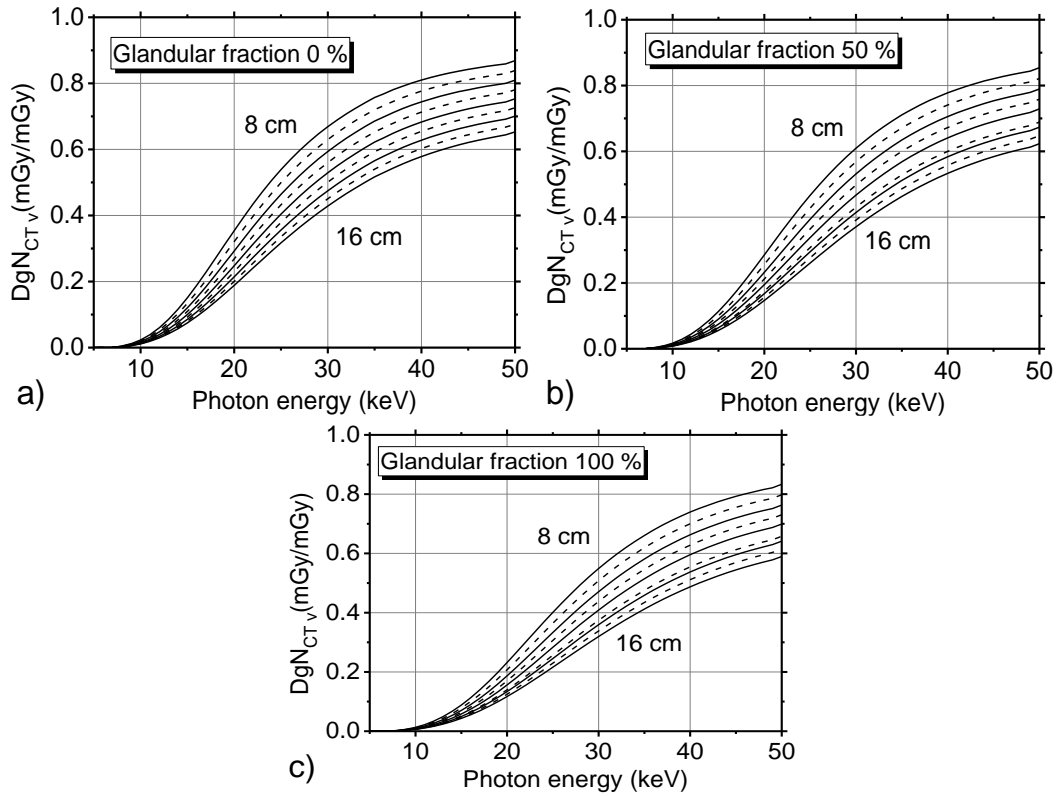
Figure 1.15: DgN$_{CT}$ coefficients useful to calculate the *MGD$_v$* (a, b, c) in the case of a 3 mm-height beam irradiating a 30 mm-height slice for a breast diameter from 8 to 16 cm in 1-cm step, and a glandular fraction of 0% (a), 50% (b) and 100% (c). The energy was varied from 8 to 50 keV with 1 keV step; data were represented as lines for ease of visualization. (form Mettivier *et al*, 2016)

Figure 1.16: DgN$_{CT}$ coefficients to calculate the MGD_t (a, b, c) in the case of a 3 mm-height beam irradiating a 30 mm-height slice for breast diameter from 8 to 16 cm in 1-cm step, and a glandular fraction of 0% (a), 50% (b) and 100% (c). The energy was varied from 8 to 50 keV with 1 keV step; data were represented as lines for ease of visualization. (form Mettivier *et al*, 2016)

1.3 Imaging Performance on phantom and breast samples

This paragraph of the thesis presents the results of the first imaging performance assessment reported by the SYRMA-CT collaboration (including my contribution to data analysis and manuscript preparation/revision). This work resulted in the publication of the following paper in international scientific journals. Here, we describe this work as illustrated in the corresponding papers.

- Sarno, A., Mettivier, G, Golosio, B, Oliva, P, Spandre, G, Di Lillo, F, Fedon, C., Longo, R., Russo, P. (2016c) Imaging performance of phase-contrast breast computed tomography with synchrotron radiation and a CdTe photon-counting detector. Phys. Med. **32**(5), 681–690.
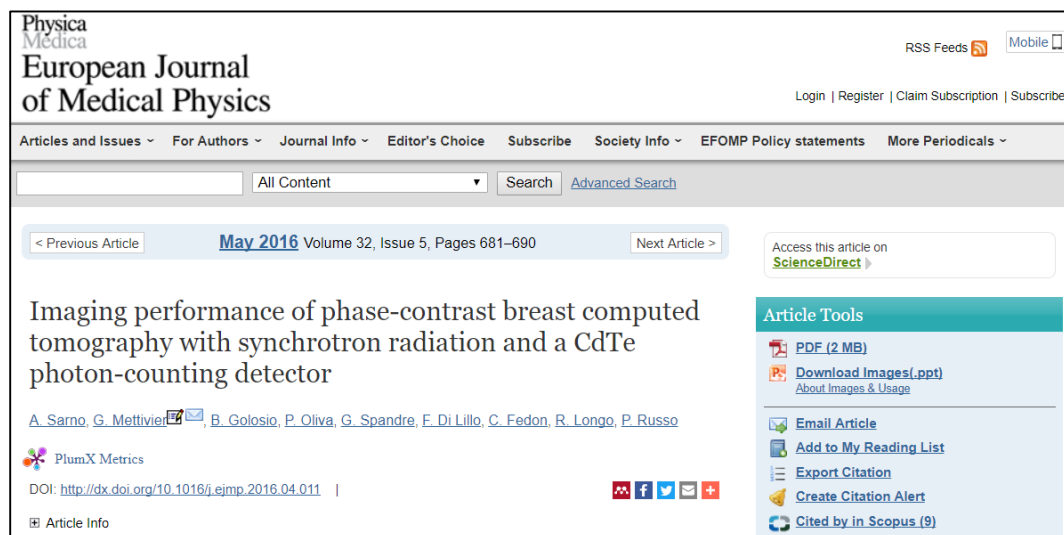
- Longo, R., Arfelli, F., Bellazzini, R., Bottigli, U., Brez, A., Brun, F., Brunetti, A., Delogu, P., Di Lillo, F., Dreossi, D., Fanti, V., Fedon, C., Golosio, B., Lanconelli, N., Mettivier, G., Minuti, M., Oliva, P., Pinchera, M., Rigon, L., Russo, P., Sarno, A., Spandre, G., Tromba, G., & Zanconati, F. (2016). Towards breast tomography with synchrotron radiation at Elettra: first images. *Phys. Med. Biol.* **61**(4), 1634–1649.
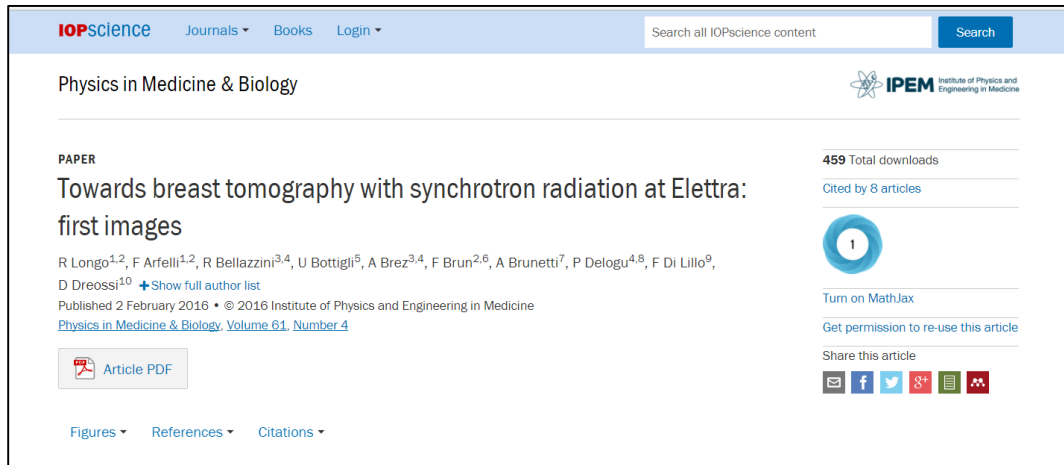
1.3.1 Evaluation of MTF and NPS of system

A system is defined linear when the response to a linear combination of stimuli with given coefficients is equal to the linear combination of the response to each individual stimulus, with the same coefficients. A noteworth application of this description is the analysis of a linear system to an arbitrary input in terms of its Fourier components. In order to evaluate the spatial resolution and the noise characteristics of our phase-contrast BCT system, we assume the applicability of linear system analysis theory for phase-contrast imaging. The high-resolution detector of the SYRMA-CT system, and the practical absence of penumbra due to the almost parallel beam geometry, contribute to produce high-resolution CT scans over a 180-deg angular span. The spatial resolution of the SYRMA-CT scanner was evaluated by measuring the system MTF; a limiting spatial frequency was evaluated at 10% MTF value ($MTF_{0.1}$). A sharp polymethylmethacrylate (PMMA) edge (for which $\delta(E) = 1.845 \times 10^{-7}$ and $\beta(E) = 1.219 \times 10^{-11}$ @ E = 38 keV (XOP 2.3), where δ and β are the component of the refractive index of the material ($n = 1 - \delta + j\beta$); thickness = 2 mm; height = 90 mm) was imaged in order to evaluate the system edge spread function (ESF), from which the line spread function (LSF) of the system was evaluated, by numerical differentiation. In order to reduce the noise, in the case of the MTF evaluation with the PMMA edge, the ESF curves have been averaged over 10 consecutive rows. The PMMA slab introduced little attenuation but sizeable phase shifts in the X-ray beam. Then, the system MTF (normalized to the value at zero

43

spatial frequency) was computed via numerical Fourier transform. It is worth noting that the fringes on the phase-contrast image of the PMMA edge (determining the edge enhancement effect typically observed in in-line phase-contrast imaging) may distort the MTF curves derived in the above way, introducing an artifact (i.e. normalized MTF values greater than 1) similar to the one occurring in CT reconstruction with the use of some kernels, characterized by undershoots in the kernel curve, see, e.g., Boone (2001b). The system MTF was evaluated also by using a highly attenuating object, a 50-μm diameter tungsten wire placed parallel to the rotation axis, at 50 mm radial distance from the axis, slightly tilted (2 deg) with respect to the rotation axis in order to obtain the presampled LSF. This technique is commonly used for spatial resolution assessment in cone-beam breast CT (Kwan *et al*, 2007, Mettivier *et al*, 2011a). The evaluation of the system MTF was carried out with two reconstruction voxel sizes ($60 \times 60 \times 60$ μm^3 and $120 \times 120 \times 120$ μm^3, respectively). This voxel size is smaller than that usually used in BCT (between 200 μm and 400 μm). This choice is related to the necessity to visualize the edge enhancement effects of SR propagation, which require a pixel size much less than 200-μm. On the other hand, the high efficiency of the single photon counting detector and its superior SNR performance with respect to energy integrating detectors, permit to investigate the performance of our system in such high resolution conditions.
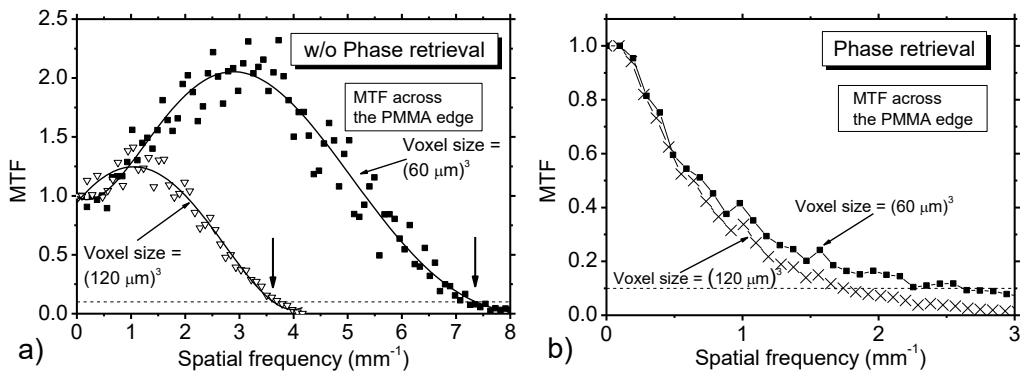
Figure 1.17: MTF curves evaluated on the images without phase retrieval (a) and with phase-retrieval (b), evaluated across the PMMA edge, with voxel size of $(60 \text{ μm})^3$ and $(120 \text{ μm})^3$ obtained with 720 projections equally spaced over 180 deg rotation scan. The dashed horizontal line indicates the 10% MTF value. (from Sarno *et al*, 2016c)

Figure 1.17 shows the system MTF in the images obtained without phase retrieval (Figure 1.17a) and with phase retrieval (Figure 1.17b), evaluated using the PMMA

edge. The curves were obtained from 720 projections equally spaced over a 180-deg scan and with an isotropic voxel of $(60 \ \mu m)^3$ and of $(120 \ \mu m)^3$. The edge enhancement effects cause an increase in the signal, as demonstrated in (Figure 1.17a). Such effects determine MTF curves which exceed the normalization value at zero spatial frequency. Due to the system spatial resolution reduction, such a phenomenon reduces as the voxel size increases from $(60 \ \mu m)^3$ to $(120 \ \mu m)^3$. Honda *et al* (2006) showed a similar result in polychromatic propagation based phase-contrast mammography, related to an ''improvement of sharpness caused by the edge effect'' (Honda *et al*, 2006). Figure 1.18 shows system MTF curves for the images without phase retrieval (evaluated with the method of the thin tungsten wire) not influenced by the phase effects. In these curves the limiting frequency at $MTF_{0.1}$ is 6.7 mm^{-1} with voxels of $(60 \ \mu m)^3$; it reduces to 2.5 mm^{-1} (evaluated over the PMMA edge) when a Paganin filter was applied to the projections (Figure 1.17b).
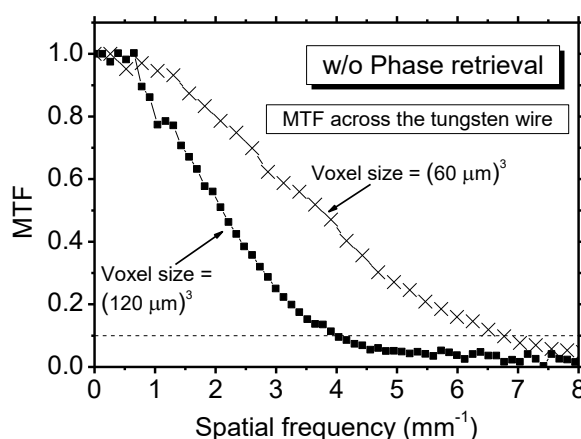
Figure 1.18: MTF curves for the images without phase retrieval, evaluated over the thin tungsten wire, with voxel size of $(60 \ \mu m)^3$ and $(120 \ \mu m)^3$ and with 720 projections equally spaced over 180 deg rotation scan. The dashed lines indicates the 10% MTF value. (from Sarno *et al*, 2016c)
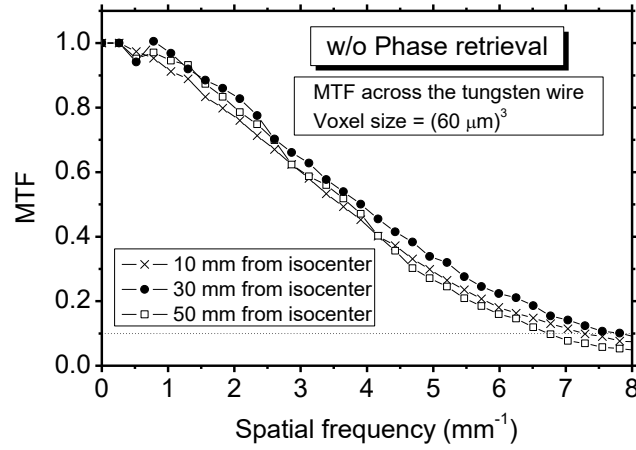
Figure 1.19: MTF curves for the images without phase retrieval, evaluated over the thin tungsten wire, with voxel size of $(60 \ \mu m)^3$ and 720 projections equally spaced over 180 deg rotation scan at 10 mm, 30 mm and 50 mm from the scanner isocenter. (from Sarno *et al*, 2016c)

Increasing the voxel size to $(120 \ \mu m)^3$ reduces the limiting spatial frequency both in the images without phase retrieval (evaluated with the tungsten wire) and with phase retrieval (evaluated over the PMMA edge) down to 4mm^{-1} and 1.7 mm^{-1}, respectively. However, the frequency at $MTF_{0.1}$ evaluated with the method of the thin tungsten wire (6.7 mm^{-1} for a voxel size of $(60 \ \mu m)^3$) does not differ significantly from that obtained with the PMMA edge (7.2 mm^{-1}); for a voxel size of $(120 \ \mu m)^3$ the limiting frequencies are 4 mm^{-1} and 3.8 mm^{-1}, respectively. Figure 1.19 shows the MTF curves for the tungsten wire, for the images without phase retrieval, at 10 mm, 30 mm and 50 mm from isocenter. The curves do not significantly differ from each other, and the slight difference can be attributed to the uncertainty in the evaluation.

The common metric for the evaluation of noise properties in attenuation based CT imaging is the (3D) NPS, which describes the spatial decomposition of noise variance in an image as a function of the spatial frequency, thus expressing the noise transfer property of the system. For the experimental determination of the NPS a scan was performed of a homogeneous mammographic phantom ($\delta(E) = 1.619 \times 10^{-7}$; $\beta(E) = 0.697 \times 10^{-11}$; @ E = 38 keV (CSIRO)), a CIRS phantom BR 50/50 mod. 014AD simulating a 50/50 breast tissue (i.e. a 50% glandular, 50% adipose tissue) (CIRS Inc., Norfolk, VA, USA). The 1D coronal NPS was evaluated as indicated in Yang *et al* (2008). The 2D NPS was estimated by the 2D fast Fourier transform from a region of interest (ROI), which did not include any target, in the coronal view.

46

Then, the 1D noise power spectrum was computed by radially averaging the 2D NPS. Pixel values in phase-contrast CT slices represent the attenuation coefficient (proportional to the local value of b) of the imaged object, and the pixel value of images after phase retrieval is proportional to δ. Then, normalized NPS (NNPS) curves were evaluated, by dividing the NPS curves by the square root of the mean signal value in the ROI where the NPS was evaluated. These curves do not depend on the signal units of measurement, so permitting to compare noise power spectrum in the images obtained with and without phase retrieval. Figure 1.20 shows the NNPS curves evaluated on the images without phase retrieval (Figure 1.20a) and with phase retrieval (Figure 1.20b). Such curves were evaluated with an image voxel size of (60 μm)^3 as well as for a voxel of (120 μm)^3. Since the (raw processed) detector pixel pitch is 30 μm, the corresponding signal bandwidth extends up to 16.7 mm^{-1} (Yang *et al*, 2008), and in the case of reconstructed coronal pixel pitch of 60 μm and 120 μm, the sampling theorem indicates that signal aliasing may be present, producing signal spectra distortions. This effect was observed in the NNPS curves in the case that the Paganin filter is not applied, where the signal deviates significantly from zero for the highest frequencies (Figure 1.20a). Such a filter is a low-pass filter, which decreases signal noise as well as the influence of aliasing (Figure 1.20b). The voxel size has strong influence on NNPS for the images without phase retrieval: indeed, the maximum of the curve with a voxel size of (120 μm)^3 is less than half of the maximum of the curve related to a voxel size of (60 μm)^3. The voxel size had weaker influence on NNPS obtained with phase retrieval. In this case, the NNPS curves show a drastic reduction in the noise level in comparison to that in images obtained without phase retrieval. For a voxel size of (60 μm)^3, the maximum of the NNPS curve in the images without phase retrieval is more than one order of magnitude greater than the maximum of the curve with phase retrieval. Moreover, the first curve presents a maximum at 3 mm^{-1}, and it reduces to about 1mm^{-1} after the Paganin filter (as a result of spatial filtering). The noise in phase retrieval imaging, being less prominent at high spatial frequencies than in the case of the images without phase retrieval, may better fit the need of detecting smaller lesions, and balance the reduction in the system spatial resolution due to the Paganin filtering.
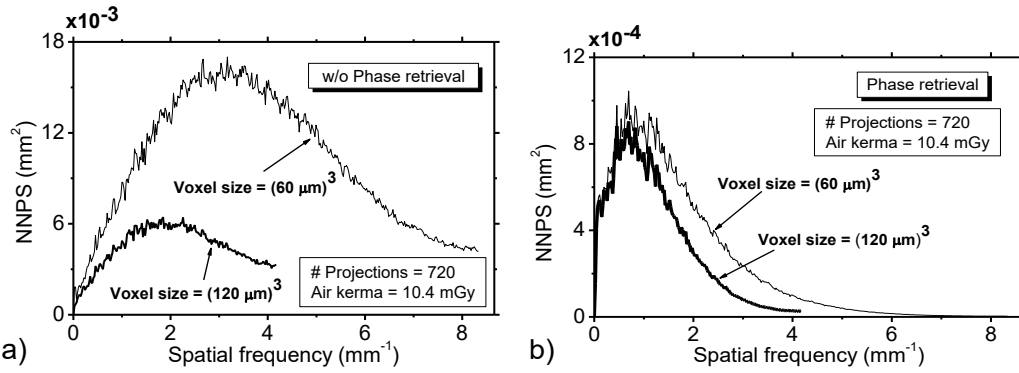
Figure 1.20: NNPS in the images without phase retrieval (a) and with phase retrieval (b). They were evaluated both with a voxel size of $(60\ \mu m)^3$ and of $(120\ \mu m)^3$ and the reconstructions were performed from 720 projections equally spaced over a 180-deg rotation scan. Air kerma at isocenter = 10.4 mGy. (from Sarno *et al*, 2016c)

1.3.2 Imaging of breast specimens

Tomographic data sets were acquired from breast tissue specimens in order to perform a preliminary evaluation of PhC breast CT images of potential clinical interest. Two breast tissues (sample 1 and sample 2) containing cancer were studied. Both of them were fixed in formalin and sealed in a vacuum bag. This work was carried out following the Directive 2004/23/EC of the European Parliament and of the Council of 31 March 2004 on setting standards of quality and safety for the donation, procurement, testing, processing, preservation, storage and distribution of human tissues. The images presented in this study were acquired in order to guide the pathologist in the localization of the lesions for the histological preparation, according to the standard procedures of the Pathology Unit of the Academic Hospital of Cattinara, Trieste University, accredited by JCI (Joint Commission International). The samples were prepared from specimens of breast lumpectomy and were derived from surgical material sent to the Pathology Unit according to local guidelines for histological examination.

Sample 1 contains an infiltrating ductal carcinoma, about 1.5 cm diameter. It is 8 mm thick and it was embedded in agar gel inside a plastic cup in order to obtain an object with dimension and attenuation comparable to that of a breast section. The diameter of the holder is about 9.4 cm. Acquisition parameters were: air kerma rate 0.52 mGy s^{-1}, 1200 projections equally spaced over 180 degrees, 50 ms per projection, MGD$_v$ equal to 23 mGy evaluated with a MC conversion factor 0.73 mGy

48

mGy^{-1}. Sample 2 contains a large (2.5 cm diameter) solid papillary carcinoma (poorly differentiated, G3 grade). Sample dimensions are about 89 mm × 36 mm, 5 mm thickness. Acquisition parameters were: air kerma rate 0.36 mGy s^{-1}, 1200 projections equally spaced over 180 degrees, 50 ms per projection, MGD$_v$ equal to 17 mGy evaluated with a MC conversion factor 0.77 mGy mGy^{-1}. For both samples, we selected an acquisition time of 50 ms per and a detector acquisition rate of 20 frames/s – close to the real conditions of the clinical trial. The imaging was performed at "high dose values" (around 20 mGy in terms of MGD$_v$), by selecting a dose rate for Sample 1 – which was fixed in agar gel – higher than for Sample 2 in order to have the same signal on the detector.

We used two reconstruction algorithms: a standard FBP algorithm and an iterative SART algorithm. FBP reconstruction on datasets with a relatively large number of projections was used as a gold standard to evaluate the performance of other reconstruction algorithms with a reduced number of projections and phase-retrieval pre-processing. The SART algorithm has been successfully applied to a wide range of CT applications (Camerani *et al*, 2004, Golosio *et al*, 2004, Cauzid *et al*, 2007); it is relatively fast compared to other iterative algorithms, and its convergence properties have been well studied (Kak and Slaney 1988). In the SART algorithm, the iterative corrections are made angle-by-angle, i.e. for each angular view, the corrections are evaluated and applied simultaneously to all rays of the projection. One iteration is considered to be completed when all the projections have been used. We used a random ordering for the projections in order to avoid systematic errors in the reconstruction. A few iterations are sufficient for the algorithm to converge. The reconstructions presented in this work were made using five iterations. The correction was multiplied by a relaxation factor, which grows linearly from zero to a maximum in the first few projections used by the reconstruction algorithm (the first 10 in this work) and decreases linearly from this maximum to zero when the number of projections increases. The relaxation factor suppresses residual oscillations, ensuring stability and convergence of the iteration (Golosio *et al*, 2004). A bilateral filter was combined with the iterative reconstruction in order to improve image regularization. This type of filter takes two parameters: a spatial filter parameter, α_d, which controls the amount of smoothing differences in

coordinates, and a range filter parameter α_r, which accounts for smoothing differences in intensities. In this work α_d is expressed in pixel units, while α_r is expressed in cm^{-1}. The latter are the same units used for the linear absorption coefficient distribution obtained by the tomographic reconstruction algorithms. In order to exploit the phase information carried out by the projections, a phase retrieval filter following the Homogeneous Transport of Intensity (TIE-Hom) Algorithm (Paganin et al, 2002) was applied prior to the actual reconstruction, with a fixed value of the δ/β ratio, namely 2508. This value was extracted from a publicly available database (https://ts-imaging.net/Services/Simple/ICUtilXdata.aspx) for the adipose tissue at 38 keV. The projections obtained by applying the phase retrieval algorithm were normalized to the same average intensity as the projections without phase retrieval. The phase retrieval pre-processing were applied to the data sampled at 60 μm pixel size, even if the image was reconstructed with 120 μm pixel size, in order to maximize the effectiveness of the algorithm, which is based on edge enhancement signals.

In Figure 1.21, image reconstructions of sample 1 are presented. Figure 1.21a has been obtained with the FBP algorithm by using 1200 projections and a MGD_v of 23 mGy. The voxel of the reconstructed images is $(120\ \mu m)^3$, as a good compromise between spatial resolution and signal-to-noise ratio. The black details inside the object are air bubbles due to the folding of the plastic bag containing the sample; edge-enhancement effects are visible at the air–plastic foil interface. Figure 1.21b shows the FBP reconstruction of 300 projections, obtained by reducing the MGD_v (about 6 mGy) of a factor 4 with respect to Figure 1.21a. Figure 1.21c shows the same 300-projections data set reconstructed by means of SART ($\alpha_d = 4$ and $\alpha_r = 0.2$). The image in Figure 1.21d was obtained by applying a phase retrieval filter prior to using the same SART algorithm used in Figure 1.21c. Images reconstructed using SART present lower noise and a preserved spatial resolution. In contrast to Figure 1.21 a–c, in the phase-retrieved image (Figure 1.21d) the glandular tissue appears brighter than the agar gel surrounding the sample. As expected, the phase-retrieved image does not show edge enhancement effects, but the noise is significantly reduced. The conventional mammography of sample 1, before agar gel inclusion, is presented in Figure 1.22 to show the fine parenchymal structures present in the

sample. They are visible in both digital mammography and CT images. However, in the latter, no overlapping features are present.
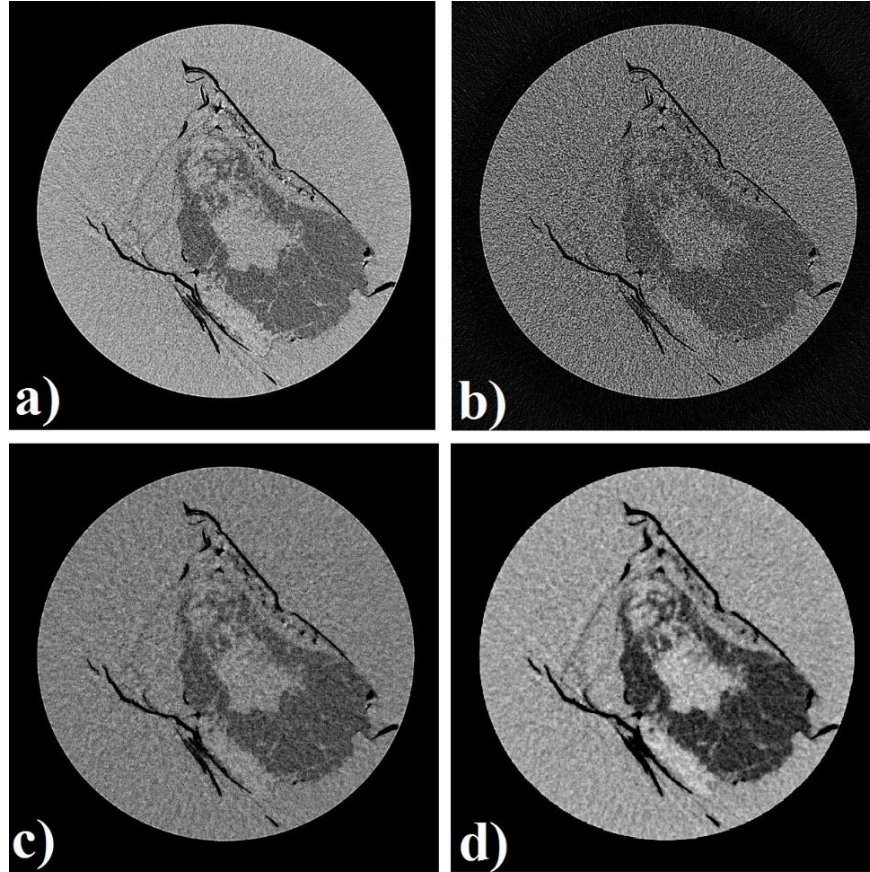
Figure 1.21: Sample 1(diameter: 9.4 cm).(a) FBP reconstruction of 1200 projections and (b) 300 projections, (c) SART (α_d = 4 pixel^{-1}, α_r = 0.2 cm^{-1}) reconstruction of 300 projections, (d) phase retrieved SART (α_d = 4 pixel^{-1}, α_r = 0.2 cm^{-1}) reconstruction of 300 projections (from Longo *et al*, 2016).
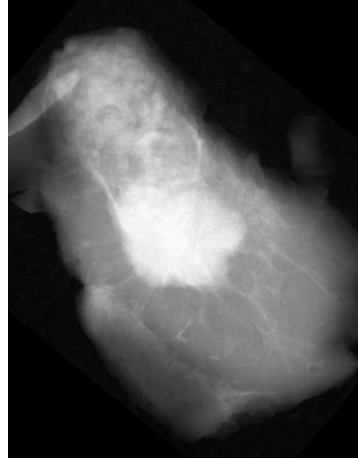
Figure 1.22: Digital mammography (planar image) of sample 1 (from Longo *et al*, 2016).

Sample 2 was studied without inclusion in the agar-gel. The MGD_v was about 17 mGy for 1200 projection over 180 degrees. According to Zhao et al (2015), in clinical breast CT, even if the voxel size is smaller than 1 mm, the radiologist adjusts the slice thickness during the image evaluation according to the diagnostic requirements, up to about 2 mm. In order to evaluate the potential clinical application of our low-dose images, 0.84 mm thick slices were obtained by adding 7 images from the sample 2 data sets. In Figure 1.23 the results are presented for the FBP reconstruction from 1200 phase-retrieved projections (a) and for a low dose reconstruction obtained by applying the SART technique on 300 phase retrieved projections (b) with a dose reduction of a factor 4 (MGDv is 4.25 mGy). Ring artefacts are visible due to the gaps between the 8 sensors of the PIXIRAD-8 detector, which were not perfectly corrected by the seaming procedure in a couple of cases. Figure 1.23c shows the planar image of the specimen obtained at a clinical mammographic unit; the nodule thickness in the sample in not constant, therefore the contrast modulation inside the cancer in the mammographic image is due to its irregular shape and not to any density inhomogeneity of the nodule.
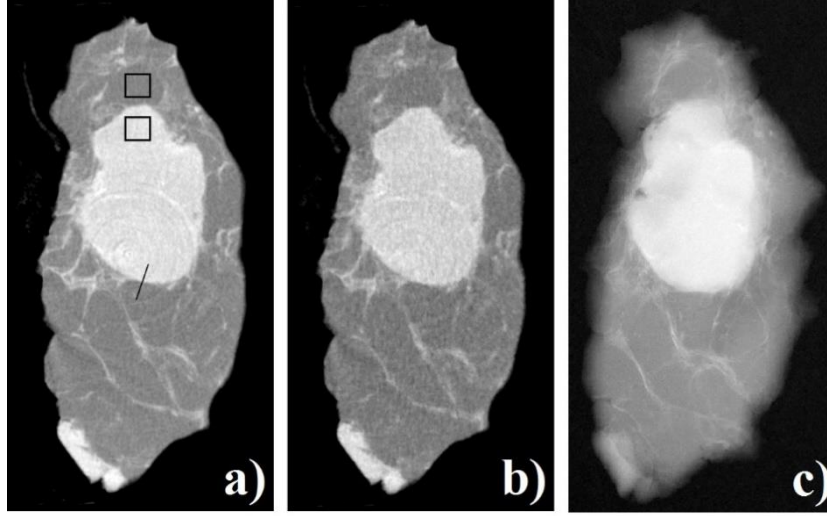
Figure 1.23: Images of 0.85 mm thick slices of Sample 2 obtained (a) from FBP reconstruction of 1200 phase retrieved projections and (b) SART reconstruction of 300 phase retrieved projections (α_d = 2 and α_r = 0.05). (c) Planar image obtained from the 5 mm-thick sample at a clinical mammographic unit. In (a) the ROIs for CNR and C assessment are outlined together with the line over which the profiles in Figure 1.24 are evaluated. (from Longo *et al*, 2016)

In order to quantify the effect of the dose reduction and the application of the iterative reconstruction, contrast (C) and contrast-to-noise ratio (CNR) values were calculated in Figure 1.23a and Figure 1.23b. The contrast and CNR were evaluated according the following definition:

$$C = \frac{|S_1 - S_2|}{S_2} \tag{1.18}$$

$$CNR = \frac{|S_1 - S_2|}{\sqrt{\frac{\sigma_1 + \sigma_2}{2}}} \tag{1.19}$$

where S is the average voxel value in the selected region of interest (ROI) and σ2 is the signal variance in the same region. The subscript numbers indicate the two ROI between which C and CNR were evaluated.

Moreover, the possible loss in spatial resolution, due to the reduction in projection in the SART image, has been investigated by measuring the signal profiles at the boundary of the lesion in both image reconstructions. In Figure 1.23a, the ROIs selected for the CNR and contrast evaluation are outlined. The contrast and the CNR for the FBP reconstruction with 1200 phase retrieved projections (Figure 1.23a) are 0.28 and 18 respectively, while, for the SART reconstruction with 300 phase retrieved projections (Figure 1.23b), C = 0.29 and CNR = 13, indicating that the

contrast is constant while a reduction of 30% of CNR is observed with a dose sparing of 75%.
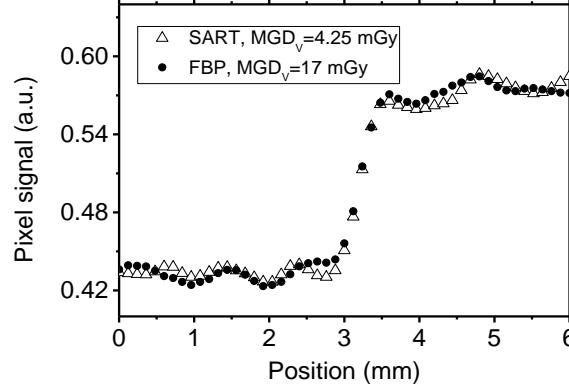
Figure 1.24: Profiles across the line in Figure 1.23a, obtained both with FBP reconstruction from 1200 projections and a MGD_V of 16.6 mGy and with SART algorithm ($\alpha_d = 2$ pixel^{-1}, $\alpha_r = 0.05$cm^{-1}) from 300 projections and a MGD_V of 4.2 mGy. Voxel size = $(120 \mu m)^3$ (from Longo *et al*, 2016).

Figure 1.24 shows the signal intensity profiles of the images (evaluated across the line in Figure 1.23a for both the FBP reconstruction with 1200 phase retrieved projections (Figure 1.23a) and for the SART reconstruction with 300 phase retrieved projections (Figure 1.23b); they presented a FWHM of 420 μm and the results were quite similar. These results suggest that the SART technique is a very promising candidate for the tomographic reconstruction of the SYRMA-CT images.

1.4 Discussion

1.4.1 Dosimetry in SR-BCT

In SR-BCT exam, the limited vertical dimension of the SR beam and the necessity to translate and rotate the patient pose practical limits to the efforts made to achieve the in vivo exam of the female breast, related to the duration of the exam and to the discomfort for the patient. In order to overcome these limitations the SYRMA-CT collaboration plans to image only a fraction of the pendant breast, by investigating only regions where a suspicious lesion has been previously located. This strategy has important dosimetric consequences. The use of the MGD in the case of the irradiation of a limited fraction of the breast could lead to an underestimation of the delivered dose. The value of this underestimation depends on the dimensions of the irradiated breast: specifically, it increases with the decrease of the irradiated volume up to 97% in the case of irradiation of a single slice of 3mm height. On the basis of these results, we introduced two new MGD parameters related only to the irradiated volume: MGD_v and MGD_t. The MGD_v is defined as the ratio between the deposited energy and the glandular mass in the irradiated volume, whilst the MGD_t is defined as the ratio between the deposited energy in the glandular mass of the whole breast and the glandular mass in the irradiated volume. The use of MGD_v and MGD_t is intended to estimate absorbed dose in the glandular tissue. We noted that the MGD_t is almost independent of the height of the irradiated volume and that it assumes values similar to the MGD value for the whole breast irradiation. In addition, we point out the close proximity between the MGD_t and the CTDI concept. Indeed, in whole body CT the $CTDI_{100}$ is evaluated in single axial scan with an ion chamber which integrates the dose along the z-axis over a length of 100mm; similarly, in the software evaluation of the MGD_t parameter the energy deposited by scattered radiation outside the irradiated volume is attributed to the glandular mass in this volume, as an additional contribution to the dose. On the other hand, the proposed MGD metric can be interpreted as an actual dose value to the glandular breast, while $CTDI_{100}$ does not represent the dose in the patient body. The parameter MGD_v was also proposed by Sarno et *al.* (2017b) as dose metric in spot compression

mammography with X-ray tube which is employed as diagnostic exam in patient with suspicious lesion.

SYRMA-CT collaboration plans to use TLDs and radiochromic films for beam and phantom dosimetry. We performed a characterization of radiochromic film XR-QA2 and TLD GR-200A for the irradiation with a monoenergetic X-ray beam in the range 18–40 keV. This work showed that dose response curves of XR-QA2 films exposed to monoenergetic (as well as polyenergetic) X-ray beams exhibit a significant dependence on photon energy, with film sensitivity ranging from a minimum of 0.0127 to a maximum of 0.0219 at 10 mGy air kerma in air, in the range of HVL values from 0.55 to 6.1 mm Al photon and corresponding effective energies from 18 keV to 46 keV. A significant variation of the response for even the very same batches of the film was also observed. These findings, also compared with the reported experience of different groups in the evaluation of the response of XR-QA2 radiochromic films, indicate the opportunity of a batch-specific, beam-quality dependent characterization of these films for their use in high accuracy, high precision reference dosimetry. The response of GR-200A TLDs to monochromatic x-rays in the range 18-40 keV showed a strong dependence on the energy. In particular, an increment of the air kerma response relative to ^{60}Co with a plateau at energy higher that 32 keV was observed. Data in the range 29-40 keV reported in this work will be updated in the next months when a calibration of IOC chamber on SYRMEP beamline with reference to the primary standard of INMRI-ENEA (Italian National Institute for Ionizing Radiation Metrology) will be performed at energy higher than 28 keV.

The dosimetric results reported in this thesis represent most of the work of the dosimetry group in the SYRMA-CT project. The new dose metrics will be used as dose reference in the examination protocol for the clinical trial. The radiochromic film characterized in this thesis will be used to provide a quantitative evaluation of the beam dosimetry before perfoming exam, as a part of the quality control procedure. Moreover, we are now testing the use of such radiochromic film for off-line dose monitoring after the exam, by recording beam variations during the breast irradiation. A piece of radiochromic film positioned in a circle around the breast – hanging in an acrylic tube or hosted in a breast holder – will record the history of the

full irradiation scan. In addition, the periodically quality assurance control will also include the evaluation of the dose distribution in phantoms which will be performed will be performed with TLD characterized in this thesis.

1.4.2 Imaging performance of SR-BCT

The combination of the fine pixel pitch, the high resolution X-ray detector embodied in the SYRMA-CT scanner, the high-spatial coherence monochromatic X-ray beam and the large distance between scanned object and detector plane (about 2 meters), permitted to detect phase-contrast effects produced by X-ray beam refraction in free-space propagation based imaging. No phase-contrast effects were present in CT slices of a breast specimen in a previous study at ELETTRA with the same geometry: this was attributed to the larger pixel pitch (200 μm) of the detector used in that previous study, which hindered the visibility of the signal overshoot and undershoot at object edges (Pani *et al*, 2004). In this work, with a 60- μm pitch detector, reconstruction voxel size of 60 μm and 120 μm side preserved the phase-contrast information. In previous investigations at ELETTRA with monochromatic SR film-screen mammography, propagation-based phase-contrast imaging showed higher contrast detail visibility than conventional mammography at a comparable or lower dose (Castelli *et al*, 2007). In this new SR setup at ELETTRA, the fine pitch featured by the single-photon counting detector determined a spatial resolution as high as 6.7 mm^{-1} at 10% MTF, in slices with voxel size of (60 μm)3 reconstructed via FBP algorithm and without phase retrieval. This system spatial resolution is significantly higher than that of polychromatic cone-beam BCT scanners (Sarno *et al*, 2015), and compares well with the 5.6 mm^{-1} limiting frequency of the helical BCT scanner developed at University of Erlangen equipped with a high-resolution single-photon counting detector (Steiding *et al*, 2014). The spatial resolution limit of the SYRMA-CT setup reduced to 2.5 mm^{-1} when a Paganin filter was applied on the projections, in the application of the phase retrieval algorithm. The edge enhancement effects seen in phase-contrast images of test objects increased the MTF curve to values higher than its zero frequency value; Honda *et al* (2006), in propagation-based phase-contrast mammography, related a similar effect seen in

their images to an improvement of the edge sharpness of the object in projected images due to the phase effects. The Paganin filter reduced drastically the image noise: the NNPS curves for images without phase retrieval had a maximum value several times greater than that in phase retrieval images. The voxel size had weak influence on noise in images obtained with phase retrieval. The NNPS curves in the images without phase retrieval reached their maximum value at about 3 mm^{-1}; on the other hand, the curves in the images with phase retrieval had their maximum at 1 mm^{-1}, balancing in part the reduction of the system spatial resolution due to the Paganin filter.

The first images of the SYRMA-CT collaboration on a breast specimen of about 9 cm in diameter indicate that clinical PhC breast CT with SR is technically feasible. An uncompressed breast diameter of 9–10 cm at chest wall corresponds to a compressed breast thickness of about 2 cm, for which the MGD for two-view mammography is 1–2 mGy (Boone *et al*, 2005). Hence, the minimum dose level (MGD$_v$ about 4 mGy) attained in this study is only 2–4 times higher than that of a two-view mammography for a 2 cm compressed breast. Noticeably, a MGD about 7 times higher than that of a two-view mammography has been reported for a 2 cm compressed breast in a polychromatic cone-beam CT clinical prototype (Sechopoulos *et al*, 2010).

The imaging study reported in this thesis was carried out at 38 keV showing the high performance of SYRMA-CT/3D setup in terms of spatial resolution and noise characterization and the improvement obtained with the SART technique for the tomographic reconstruction. It represents the start point of the optimation of the exam parameters for the future clinical trial. In order to obtain the highest image quality with the lowest possible dose, the SYRMA-3D collaboration is now studying the performance of the PhC-BCT setup, in terms of hardware – such as detector, bed setup – (Sarno *et al*, 2016c, Delogu *et al*, 2017a, Delogu *et al*, 2017b) and software – such as reconstructyion algorithm (Fardin *et al*, 2016, Sarno *et al*, 2017c). Nesterets *et al* (2015) and Baran *et al* (2017) have recently reported on the parameters optimization in propagation-based PhC-CT with synchrotron radiation, using setups different from that of SYRMA-CT/3D. Nesterets *et al* (2015) in a study on cylindrical phantom at 35, 45, and 50 keV showed that it is possible to detect the

phase effects also using a detector with relatively large pixel size: this results from the adoption of long sample-to-detector distances up to 5 m. They also report that the energy which optimizes the image quality, in terms of Contrast-to-Noise Ratio per unit of dose and the FOM ("*the ratio of the CNR per unit dose to FWHM of the material boundaries*"), depends on the analysed materials. Successively, Baran *et al* (2017) found that the propagation-based technique gives significant promise for low-dose BCT on patient when employing a photon energy of 32 keV, a sample-to-detector distance of 9 m and TIE-Hom phase retrieval pre-processing combined with iterative CT reconstruction algorithms. The projections are acquired with a conventional-flat panel detector (pixel size about 100 μm) or a high-resolution CCD TDI sensor coupled to a CsI scintillator (pixel size about 54 μm) (Baran *et al* 2017). Our setup for clinical trial provides a maximum sample-to-detector distance of 2 metres which may reduce the image quality according to Baran *et al.* (2017); on the other hand, the setup includes a single-photon counting detector with a high spatial resolution (60 μm) and high efficiency, which is expected to improve the imaging performance of the system.

It is important to take into account that PhC techniques different from propagation-based imaging (PBI) – such as analysed-based imaging (ABI), grating interferometry (GI) or edge illumination (EI) – are also under investigation for breast imaging by using a synchrotron radiation source or an X-ray tube. The analyser-based PhC technique (which uses an analyser crystal between sample and imaging detector, Coan *et al*. 2013) showed good performance for breast imaging (Ando *et al*, 2008), providing images comparable to those obtained from histopathology slice (Coan et *et al*, 2013, Kerilainen *et al*, 2008, Sztrókay *et al*, 2012) and with an imaging dose comparable to that of two-view mammography (Coan et *et al*, 2013, Zhao *et al*, 2012). Although previous studies were performed with synchrotron radiation, images with high contrast at low doses can also be obtained with a laboratory-based X-ray source (Coan *et al*, 2013). GI uses a Talbot grating interferometer and was investigated for breast imaging with a synchrotron source (Sztrókay *et al*, 2013, Willner *et al*, 2014) as well as with an X-ray tube (Willner *et al*, 2014, Stampanoni *et al*, 2011, Grandl *et al*, 2013). This technique permits to obtain three different kind

of images – absorption, refraction and scattering images. The combination of these images may produce an improvement in the detection of mammographic lesions (Coan *et al*, 2013, Stampanoni *et al*, 2011). However, the critical issue of this technique is the dose to the organ that is still much larger than that of the conventional two-view mammography. Also the EI technique is based on the use of grids (coded apertures), but it is not an interferometric technique – the sample is irradiated with a narrow beam and an absorption edge is placed in front of the detector (Coan *et al*, 2013). The first studies of this technique (Olivo *et al*, 2013, Szafraniec *et al*, 2015) on phantom and breast specimens for 2D imaging showed an improvement of the image quality with respect to the images from conventional exams at comparable dose level.

Although all these PhC techniques showed good results in terms of image quality, we notice that most literature reports were performed either on phantoms or on ex-vivo specimens, rather than *in vivo*. Moreover, ABI and GI techniques need to resolve critical issues such as the more complicated setup and, in the case of the GI, the dose to the organ for a possible clinical application. On the other hand, the EI technique seems to give good promise for future clinical application, but only 2D imaging has been investigated so far. In this scenario, PBI is the only technique which kas been validated on a clinical trial on mammography exam (Castelli *et al*, 2011, Longo *et al*, 2014) and a planned clinical trial program on breast computed tomography.

PART II

Breast Rotational Radiotherapy with Synchrotron Radiation

The feasibility study of breast cancer rotational radiotherapy with synchrotron radiation has been a major part of my activity during the second half of the PhD thesis work. This work resulted in the publication of the following two papers in international scientific journals. Here, we describe this work as illustrated in the corresponding papers.

- Di Lillo, F., Mettivier, G., Sarno, A., Castriconi R., & Russo, P. (2017a). Towards breast cancer rotational radiotherapy with synchrotron radiation. *Phys. Med.* **41**, 20–25

- Di Lillo, F., Mettivier, G., Castriconi, R., Sarno, A., Hausermann, D., Hall, C, Stevenson, A.W., Russo, P. (2017b) *Synchrotron radiation external beam rotational radiotherapy of breast cancer: proof of principle.* J Synchrotron Rad, under review.

In addition, some results obtained during my co-supervision of the M.Sc. thesis in Physics of Dott. Paolino Alberto De Lucia "Kilovoltage Rotational External Beam Radiation Therapy (kV-EBRT) for breast cancer treatment" 2015 are presented. (De Lucia, 2015)

2.1 Conventional radiotherapy

Breast cancer is the most common malignancy in woman (Torre *et al*, 2016). The standard care after breast-conserving surgery includes postoperative radiotherapy to remove any cancer cells that may be left in the breast. The commonly used technique for breast cancer is megavoltage photon 3D-conformal radiotherapy (3D-CRT), using a medical linear accelerator: the therapy (45 to 50 Gy in 25 fractions of 1.8 to 2 Gy) is normally delivered with two opposed tangential fields to encompass the breast, often including part of the underlying chest wall and the lower axilla. The treatment planning consists in designing the radiation fields on the basis of CT data sets from the individual patient (Cox & Kian Ang, 2010). In order to reduce troubles due to the patient repositioning, marks are placed on the patient after CT scan to identify the isocentre of the irradiation field. The effectiveness of the breast radiotherapy strongly depends on the dosimetry. The 3-D treatment planning systems are also able to include the contribution of the scattered radiation into the dose calculation providing an accurate dose model. During the treatment, the patient is usually in a supine position. However, radiotherapy in prone position can be evaluated for patients with a large breast (Merchant *et al*, 1994; Kirby *et al*, 2010; Lymberis *et al*, 2012). X-ray irradiation with 6-MV X-ray beam produces a so called buildup effect whereby the dose to the surface tissue layers several millimeters below the skin is reduced to a fraction of the maximum dose at depth in the tissue, so avoiding skin tissue complications after therapy. After the conventional radiotherapy treatment, a radiation boost can be delivered with electron or photon beams in order to reduce the risk of local recurrence (Cox & Kian Ang, 2010). Patients who undergo a breast-conserving surgery are treated with a boost to the tumour bed delivering doses ranging between 10 and 16 Gy depending on the status of the surgical margins (Cox & Kian Ang, 2010). For patients who undergo mastectomy, an additional boost of 60 Gy is delivered to the chest wall (Cox & Kian Ang, 2010).

One of the critical issues of breast radiotherapy is the associated increased rate of ischemic heart desease, especially in patients treated for left-sided breast cancer (Darby *at al*, 2013; Manna *et al*, 2016, Henson *et al*, 2013). With improved survival, more patients will be at risk for long-term radiation-induced toxicity, thus making it

even more important to reduce the dose to all organs at risk. As the rate of the ischemic heart disease is proportional to the mean heart dose, the goal is to reduce the dose to the heart as much as possible. Intensity modulated radiotherapy (IMRT) with photons has been investigated in order to improve the dose homogeneity and to minimize doses to surrounding organs at risk with both fixed and rotating beams. Then, photon planning using 3D-techniques, deep inspiration breath-hold, and prone position are implemented to minimize cardiopulmonary dose for patients. However, the radiation dose to the heart remains relatively high, even with the use of advanced photon-based techniques (Mast *et al*, 2014). Due to its ballistic physical characteristics (high dose localization and high cell-killing effect at the Bragg peak of the energy deposition curve), proton beam radiotherapy (PBT) may eventually enable a further decrease of the dose to the heart. A proton beam is characterized by a dose distribution that is finite and adjustable in depth depending on the beam energy. For this reason, PBT is increasingly being investigated to treat breast cancer showing a considerable reduction of the mean heart dose with respect to 3D-CRT and IMRT (MacDonald, 2016). To address the question of whether proton therapy can meaningfully decrease radiation-induced cardiovascular toxicities in breast cancer, in early 2016 started the Patient-Centered Outcomes Research Institute-funded Radiotherapy Comparative Effectiveness (RadComp): a pragmatic randomized trial of proton therapy versus photon therapy for patients with nonmetastatic breast cancer (Verma *et al*, 2016).

In the last decades, new radiotherapy techniques based on the orbital rotation of the Megavoltage X-ray beam – such as IMRT tomotherapy, Intensity Modulated Arc Therapy (IMAT) or Volumetric-Modulated Arc Therapy (VMAT) – have been developed (Khan and Gibbson, 2014). The geometry of these systems is similar to that of the CT scan. The accelerator head is on a rotanting gantry and rotate around the axis of the longitudinal axis of the patient treatment. In IMRT tomotherapy, the patient is treated slice-by-slice, as in a CT imaging exams; the intensity modulation is produced by means of a Multi Leaf Collimator (MLF) with a specific design and the couch can be stationary during the irradiation of a single slice or can continuously translate during the treatment (Khan and Gibbson, 2014). The latter, called helical tomotherapy, was introduced by Mackie *et al* (1993) and is more utilized than the

static-based technique nowdays. Whilst the IMRT tomotherapy adopted a fan beam, IMAT and VMAT technique employ a cone beam permiting to irradiate the whole volume instead of slice-by slice. IMAT (Yu, 1995) is based on the overallapping of the delivery from multiple arcs to obtain the intensity modulation (Rao *et al*, 2010). However, the introduction of a new generation of linear accelerator which permits to change the MLC leaf position, dose rate and the speed of rotation of the gantry (Rao *et al*, 2010) has allowed to introduce a new method, called VMAT (Otto, 2008), to deliver the prescribed radiation dose with a single arc (Rao *et al*, 2010). These rotational radiotherapy techniques have shown to provide a more precise dose distribution with a major sparing of the healthy tissue. In particular, the studies on the use of tomotherapy for breast cancer treatment have demonstrated the possibility of reducing the dose to the heart (Coon *et al*, 2010, Gonzalez *et al*, 2006) in the case of left-sided whole-breast irradiation. In addition, for accelerated partial breast irradiation (APBI) Rault *et al* (2016) showed that IMRT tomotherapy provides a more efficient spare of the non-target breast tissue volume and an improvement in the cosmetic result with respect to the 3D-CRT. Moreover, in the last years a particular attention is on the use of VMAT for breast cancer treatment. Recent studies have carried out a significant reduction of the dose to healthy tissue (Fogliata *et al*, 2017) and a significant improvement in target coverage and conformity with respect to IMRT (Moorthy, 2016). However, Fogliata *et al* (2017) also reported that the spare of the normal tissue occurs with some "high dose spillage" (Fogliata *et al*, 2017) requiring additional studies to provide the optimal balance and reduce future late toxicity and secondary cancer induction risk (Fogliata *et al*, 2017).

A recent study on phantom and breast patients (Breitkeutz *et al*, 2017) – based on Monte Carlo simulations – showed the feasibility of kilovoltage arc-therapy (KVAT) with 200-kV X-ray beam in both supine and prone positions. However, the quality of dose distributions obtained were lower than those obtained with VMAT plans (Breitkeutz *et al*, 2017). The study also showed the improvement of the dose distribution for the prone breast phantom with respect to the supine position because of the increment of the treatment angle (Breitkeutz *et al*, 2017).

2.2 Kilovoltage external beam radiotherapy with an orthovoltage X-ray tube

In 2012, in a pioneering paper (Prionas *et al*, 2012), J. Boone and his team at University of California Davis set forth the idea of performing external-beam rotational radiotherapy (kV-EBRT) of the breast cancer with an orthovoltage X-ray tube. kV-EBRT requires a dedicated setup employs an orthovoltage X-ray tube operating at 320 kVp and rotating in full circles around the breast, rather than a megavoltage X-ray beam from a medical linac irradiating the breast with two tangential beams, as in conventional breast radiotherapy with photons. The technique could be implemented on the rotating gantry of a cone-beam computed tomography scanner dedicated to the breast (Sarno *et al*, 2015), e.g. as realized by the Davis group and operating at 80 kVp, thus providing precise 3D localization of the tumour mass in the breast volume. The advantages of the kV-EBRT technique with respect to conventional radiotherapy were described as a simplified and more economical setup (which also does not require a bunker), the potential for reduced patient repositioning error and improved treatment accuracy in fractionated radiotherapy, the use of a prone rather than a supine patient position. The well-known effect of absorbed dose build-up of such 6–10 MV photon beams – which assures dose sparing to the surface tissues in conventional radiotherapy, with a maximum dose at 15 mm below the zero-depth layer in tissue at 6 MV – is much reduced for the 320 kVp X-ray beam adopted in Boone's setup. Indeed, for orthovoltage X-ray beams the nominal depth of maximum dose beneath the patient's surface is zero (Podgorsak 2005). On the other hand, for 6 MV X-ray photons the dose buildup effect produces a surface dose as low as 15% of the maximum depth dose (Podgorsak 2005). Despite the practical unavailability of the buildup region for kilovoltage photons, the principle of rotational summation leads to higher dose at the tumour site – where the axis of rotation of the gantry is positioned – by suitably collimating the beam, substantial skin tissue sparing could be obtained. Indeed, the summation of the dose deposited by the collimated X-ray beam irradiating the breast from a plurality of angles in a full rotation results in a dose distribution peaked at the centre of rotation. The width and shape of the peak depend on the beam collimation on the horizontal plane (and

to some extent also on the vertical plane), while the vertical collimation determines the extent of the longitudinal height of the irradiated target (in the direction from chest wall to nipple). In their feasibility study, (Prionas *et al,* 2012) obtained via MC simulations a dose ≤ 5% of target dose deposited at 4 cm from the treatment field (along the chest wall-to-nipple direction) for a 2-cm z-collimated treatment beam centred in the middle of a 14-cm diameter breast, for whole breast irradiation or partial breast irradiation. However, there are some limits of this technique related to the relatively low dose rate available at practical distances (50−100 cm) from the collimator units of an orthovoltage tube (in the order of 1 Gy/min) and to the thick lead collimator for a 320 kVp beam, which introduces penumbra and scatter.

2.2.1 *Experimental Validation of kV-EBRT*

The technique of kV-EBRT with orthovoltage X-ray tubes has been validated experimentally at 120 kVp by the team of Prof. Boone (Prionas *et al*, 2012). Following the work of the Davis' group, we carried out an experimental validation at 300 kVp (De Lucia, 2015) by using an orthovoltage X-ray tube (Siemens Stabilipan 2) available at the Department of Physics "E. Pancini" of Università di Napoli Federico II. We measured the radial dose profiles in a PE cylindrical phantom (diameter of 14 cm and height of 15 cm) with a 100-mm pencil ionization chamber (mod. 20x6-3CT, Radcal Corp., Monrovia, CA, USA) tuning the collimation of the X-ray beam. The phantom had 1.3 cm-diameter holes drilled at different distances from the cylinder axis, for allocating the pencil chamber (Figure 2.1). The X-ray tube operated at 300 kVp, 12 mA and the X-ray beam was filtered with 1 mm Al, 0.25 mm Cu, 1.2 mm Sn, 3.12 mm Cu. For this spectrum, we measured a half value layer (HVL) of 4.25 ± 0.009 mm Cu and an air kerma rate free in air of 0.0330 ± 0.0001 Gy/min at the isocenter (@ 94.5 cm from the focal spot). The radial profiles were measured collimating the X-ray beam at 10 cm along the direction of the cylinder axis and at 1 cm, 3 cm, 7 cm or 14 cm in the rotation plane. The experimental results were compared with that obtained via Monte Carlo (MC) simulations. We reproduced the experimental irradiation geometry with a MC code developed in house, based on Geant4 toolkit (version 10.00). A complete description of the MC is reported in Section 2.4. In De Lucia (2015), the author shows, by using a MC code

different from that used in this work, that the X-ray beam produced by the orthovoltage X-ray tube working at 300 kVp produces the same dose distribution in the PE phantom obtained with a monoenergetic X-ray beam of 175 keV. On this account, we simulated a rectangular X-ray source that generated a monoenergetic beam of 175 keV. The sizes of the X-ray source were varied according to the simulated case. The rotational irradiation was reproduced by rotating the source along a 360° circle, in step of 1°, around the phantom. Figure 2.2 shows the comparison between the radial dose profiles measured with the 100-mm pencil chamber (symbol) and those evaluated via MC simulation (line) for beam collimation of 1, 3, 7 and 14 cm. Different beam collimations produce different shapes of the radial profile. In particular, whilst a cup-shaped dose distribution results for irradiation with the 14-cm wide beam, a dose distribution peaked at the centre of rotation is obtained with a beam collimated at 1cm. The simulations agree with the measurements for beam collimation of 14 cm and 7 cm with maximal relative difference of 6%. However, significant discrepancies, up to 30%, were estimated for 1-cm collimated beam. De Lucia shows similar results in his study (De Lucia, 2015). Table 2.1 reports the mean percentage difference in the dose distribution between measurements and MC simulations estimated in this study and in (De Lucia,2015). These values are comparable for each beam collimation.
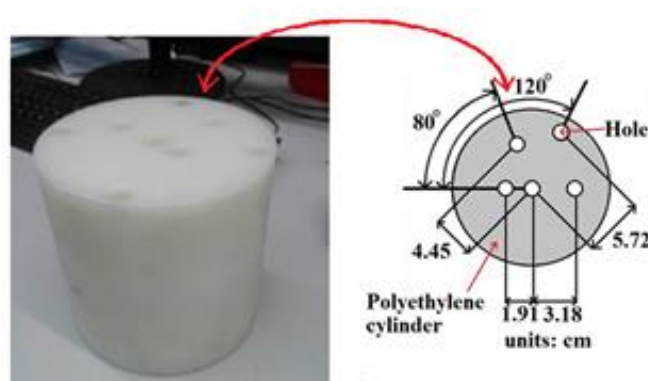
Figure 2.1: Photo and scheme of the polyethylene cylindrical phantom with five cylindrical holes at various radial distances for hosting a 100-mm long ion chamber. (from Di Lillo *et al.* 2017b)

The discrepancy between measurements and simulations could be due to a misalignment of the cylindrical phantom with respect to the X-ray beam during the experiment. In this case, a different dose distribution is measured in the phantom. This effect is amplified in the case of the collimated beam in which the centre of rotation coincides with the position of the maximum doseIn addition, both MC codes were validated with additional tests (De Lucia, 2015, Section 2.4) confirming their good performance. Please note that the MC simulations have been carried out in parallel beam geometry.
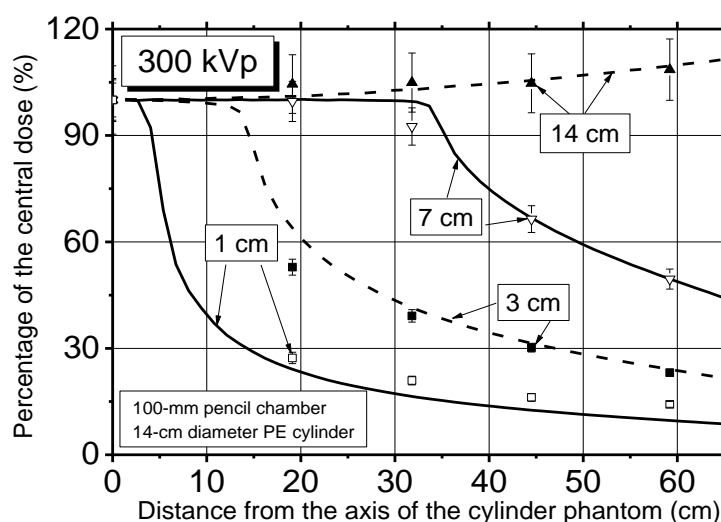
Figure 2.2: Comparison between the measured (symbols) and simulated (lines) relative air kerma in a 14-cm diameter polyethylene cylindrical phantom for beam width of 1, 3, 7 and 14 cm. For the MC simulation, the dose distribution was evaluated by integrating the dose along 100 mm in the direction of the cylinder axis.

Table 2.1: Mean percentage difference in the dose distribution between measurements and MC simulations evaluated in this work and in (De Lucia, 2015).

Collimation of X-ray beam (cm)	Mean Percentage Difference (%)	
	This work	De Lucia, 2015
15	2 ± 1	2 ± 1
7	3 ± 2	3 ± 3
3	6 ± 4	8 ± 6
1	21 ± 7	18 ± 8

2.3 SR³T: Synchrotron Radiation Rotational Radiotherapy for breast cancer

The orthovoltage X-ray tube used for kilovoltage external beam radiotherapy provides a polychromatic X-ray beam with moderately low flux (yet adequate for conventional dose fractionation strategies), e.g. ≤ 1 Gy/min at 50 cm from the source (Prionas *et al*, 2012). A polychromatic as well as monochromatic X-ray beam with higher flux (also suitable for hypofractionated dose delivery, a technique under extensive clinical investigation (De Rose *et al*, 2016)) can be obtained by using a synchrotron radiation source. Indeed, the SR may provide a monoenergetic (as well as a polyenergetic) X-ray beam with higher flux and lower energy (down to a few tens of keV) with respect to the orthovoltage X-ray tube. Experimental research on SR radiotherapy (SRT) is currently only possible at few facilities in the world, with the Australian Synchrotron (AS, Melbourne, Australia) and European Synchrotron Radiation Facility (ESRF, Grenoble, France) having active programs for developing clinical applications. Three methods are under investigations: the stereotactic radiotherapy (SSRT), the mini-beam (MBRT) and the micro-beam radiotherapy (MRT). SSRT (Bräuer-Krish *et al*, 2015, Renier *et al*, 2008, Edouard *et al*, 2010) employs a highly conformal irradiation geometry combined with a dose-enhancement effect due to the injection of a high-Z element in the target. A clinical trial of this technique for brain cancer treatment is ongoing at ESRF by using a monochromatic X-ray beam at 80 keV with a dose rate of about 1 Gy/s. MBRT (Prezado *et al*, 2009a, Prezado *et al*, 2009b, Prezado *et al*, 2011, Prezado *et al*, 2012, Deman *et al*, 2012, Martinez-Rovira *et al*, 2014, Prezado *et al*, 2015) and MRT (Slatkin *et al*, 1992, Bravin *et al*, 2015, Grotzer *et al*, 2015, Crosbie *et al*, 2013, Martinez-Rovira *et al*, 2010, Martinez-Rovira *et al*, 2011, Martinez-Rovira *et al*, 2012a, Martinez-Rovira *et al*, 2012b, Poole *et al*, 2017) use a geometric irradiation effect called *spatial fractionation* of the total dose delivery, whereas conventional radiotherapy adopts *temporal fractionation* (e.g. 50 Gy in 25 fractions for breast irradiation in the adjuvant radiotherapy of breast cancer). Temporal fractionation can be used in addition to spatial fractionation in MRT (Serduc *et al*, 2009). While MRT employs a polychromatic SR beam segmented into micro-beams of typical size in

the range 25-50 μm, in MBRT a monochromatic X-ray beam divided into mini-beams of size 500-600 μm irradiates the target. At present, preclinical studies on MRT are ongoing at ESRF and AS, and preliminary experiments are underway at the Canadian Light Source (CLS). Although several small animal models have been used (mice, rats, rabbits, and piglets), nearly all preclinical SRT studies to date have focused on brain tissue. On the other hand, a pilot study on the monochromatic micro-beam therapy (m-MRT) technique applied to treat breast cancer tissue and cell samples was carried out at CLS recently (Wysokinski *et al*, 2016) showing a slowing down of the tumour growth implanted in mice and cancer cell apoptosis generated by m-MRT irradiation at 60 and 100 keV. The availability of world-class facilities and the associated expertise of the investigators enable studies that have the potential to substantially improve SRT for cancer and advance our understanding of fundamental tumour biology.

In this work, we envisage the possibility of the use of the SR (De Lucia *et al*, 2016, Di Lillo *et al*, 2016b, Di Lillo *et al*, 2017a,b) for breast cancer treatment with a rotational irradiation geometry similar to that of kilovoltage external beam rotational radiotherapy with an orthovoltage X-ray tube (Prionas *et al*, 2012). In SR rotational radiotherapy (SR^{3}T), the patient is lying prone on a rotating/translating bed, with the breast hanging from a hole in the bed, while the SR beam (suitably collimated in the horizontal and vertical directions) irradiates the organ, incident from a plurality of azimuthal angles (Figure 2.3). A full rotation of the bed around a vertical axis centred at the tumour site permits to deliver the highest dose at isocentre and a reduced dose at the entrance and exit surfaces. A combination of successive horizontal and vertical translations of a robotized bed, interleaved by 360° rotations, permits to fully irradiate the tumour volume. Whole breast as well as partial breast irradiations can be performed with multiple rotation by tuning the beam collimation. Since dose rates largely exceeding 10 Gy/min (considered adequate for breast radiotherapy) can be obtained at SR sources, irradiation of the tumour (partial irradiation) or of the whole organ (total irradiation) of the female breast for total doses in the order of tens of grays can be performed in one or a few fractions.

71
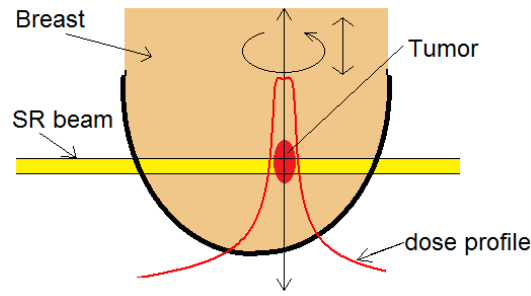
Figure 2.3: Sketch of SR-EBRT. The patient is lying prone on a bed with her breast hanging from a hole. The bed is rotating around a vertical axis centered at the tumor site, while the collimated X-ray beam from a synchrotron radiation source irradiates the tumor. The bed is then translated vertically and horizontally and additional rotational scans are performed, in order to conform the treatment to the tumor volume. A dose enhancement can be obtained by using a radiosensitizer (e.g. gold nanoparticles or iodinated solutions). (by courtesy of P. Russo)

SR^{3}T will employ a monochromatic X-ray beam with energy in the range $60-120$ keV. Rotational summation at the tumour (where the axis of rotation is positioned) will produce dose summation up to the prescribed level in the target tumour tissue, while the dose to the skin would be limited to levels in the order of 1/10 of the tumor dose. At the same time, low dose levels may be delivered to healthy internal organs and tissues (including lung, heart, carotid arteries) due to the limited photon scatter dose toward the chest wall (estimated at less than 5% of the tumour dose in Prionas et al, 2012 for a 320 kVp beam). The 3D localization of the tumour before as well as during the RT procedure with SR can be performed via parallel beam computed tomography (CT) imaging of the transmitted X-ray beam with the patient in prone position on the robotized support (Lindfors *et al*, 2008; O'Connell *et al*, 2010; Russo *et al*, 2010; Mettivier *et al*, 2011b; Sarno *et al*, 2015). This will implement SR breast CT (Longo *et al*, 2016; Mettivier *et al*, 2016, Sarno *et al*, 2016c) for the needs of image guided radiotherapy of breast cancer. The use of X-ray beam at energies lower than 120 keV, on the other hand, will permit to use an iodinated contrast medium (commonly adopted clinically for contrast enhanced digital mammography) or other radiosensitizers (e.g., gold nanoparticles, Lin *et al*, 2015) for realizing contrast-enhanced breast CT as well as dose-enhanced radiotherapy. This technique exploits the increase of the absorbed energy in the tumour where the iodinated agent accumulates.

In the following sections, we illustrate the results of the feasibility study of SR^{3}T performed at Australian Synchrotron, Melbourne, Australia and the European Synchrotron Radiation Facility, Grenoble, France.

2.4 *Monte Carlo simulations for SR^{3}T*

We simulated the irradiation of a homogeneous phantom with SR^{3}T technique. Simulation were performed with the GEANT4 toolkit (version 10.00). The MC code used in this work is based on a previous version developed for breast dosimetry in mammography (Sarno *et al*, 2016a,b) and digital tomosynthesis (Sarno *et al*, 2017d) by Dr. A. Sarno during his PhD work (Sarno, 2017a). This code was modified by implementing the rotation of the X-ray source and the event position scoring. The parallel and monoenergetic X-ray beam was generated from a rectangular source of variable size tuned on the basis of the simulated cases. The source performed a rotation of 360°, in step of 1°, around a PE (density = 0.9325 g/cm^3) or a PMMA (density = 1.19 g/cm^3) cylindrical phantom (14-cm diameter, 15-cm height). We scored the energy deposited in the phantom produced by interactions of both primary and secondary photons (scattered photons, fluorescent and bremsstrahlung photons), as well as the energy deposited by the electrons produced at the photon interaction (multiple scattering included). The event position was also recorded. The scoring resolution was $1 \times 1 \times 1$ mm^3. The simulation output was a 3D matrix obtained by associating the energy absorbed by the phantom to the event position. Albeit the validation of the main part of the code is reported in (Sarno *et al*, 2016b), additional tests were performed to validate this last version. In particular, we performed a comparison with literature data reported by Prionas *et al* (2012) simulating the irradiation of a PE cylindrical phantom (diameter of 14 cm and height of 9 cm) with a monoenergetic laminar beam at 178 keV collimated at 14 cm $\times$ 0.1 cm (H $\times$ V). The cylinder axis was positioned along the vertical direction. The radial dose profile evaluated in the irradiated slice was taken into account for the comparison. Figure 2.4 shows the comparison of the radial dose distribution in a 14-cm PE cylindrical phantom obtained for a beam width of 14 cm at 178 keV via our code and that reported by Prionas et al. (2012). A maximum deviation of 2% was observed. In the

following sections, we also report a comparison between the results from simulations and experimental data. Please note that the MC simulations of this work have been carried out in parallel beam geometry.
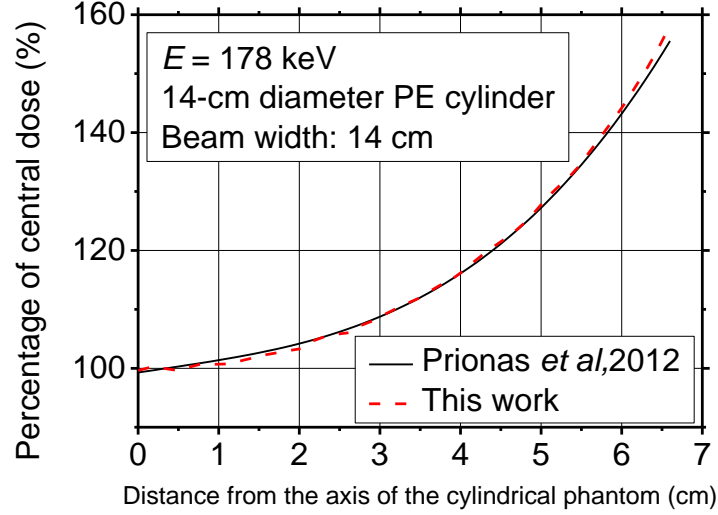
Figure 2.4: Comparison between dose distributions (percentage dose versus radial distance) in a 14-cm diameter PE cylinder obtained via MC simulation in this work (dashed red line) and that reported by (Prionas et al., 2012) (continuous black line). (from Di Lillo *et al.* 2017a)

2.4.1 Skin sparing effect

The MC code was employed to investigate the feasibility of using a monoenergetic X-ray beam with energy down to 60 keV. In particular, the skin sparing effect was evaluated by using a monoenergetic beam at 60, 80, 100, 120, and 175 keV (this last being the depth-dose effective energy of the orthovoltage X-ray beam available at our Department's irradiation facility, close to the 178-keV effective energy simulated in the Davis' study (Prionas *et al*, 2012)). The simulations reproduced the irradiation of the PE cylindrical phantom (of 14 cm diameter and 15 cm height) - simulating the pendant breast with a diameter equal to the average diameter at chest wall of the uncompressed breast (Boone *et al*, 2005) - with the X-ray beam collimated at 150 mm × 6 mm (H × V) and the centre of rotation along the phantom longitudinal axis. A possible skin sparing effect was evaluated in terms of periphery-to-centre dose ratio in the cylindrical phantom. Figure 2.5a and Figure 2.5b show the dose distribution obtained via MC simulation in a 14-cm diameter PE cylinder with X-ray beam of size 15 mm × 6 mm (H × V) at different energies in the range 60−175 keV and the periphery-to-centre dose ratio vs. the photon energy, respectively. The radial

dose distributions were normalized at their respective maximum, which occurs at the axis of rotation. At each energy the shape of the radial dose distribution for the collimated beam (peaked at the centre of rotation) changes (figure 2.5a). In particular, an exponential decrement of the periphery-to-centre dose ratio can be observed by increasing the photon energy (figure 2.5b), from a value of about 13.5 % at 60 keV down to 10.5 % at 175 keV. From these data, we derived that for a tumour positioned at the phantom centre, the tumour-to-skin dose ratio would be 9.5 at 175 keV and 7.4 at 60 keV photon energy.
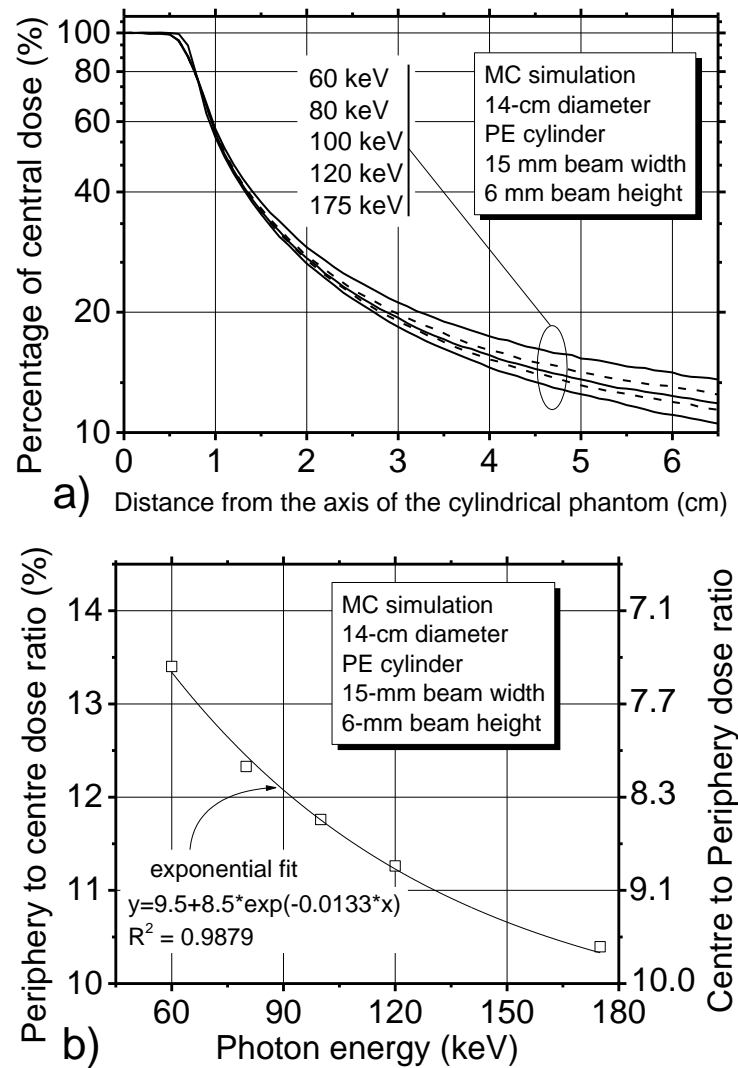
Figure 2.5: Radial dose distribution in a 14-cm PE cylindrical phantom obtained with a collimated beam (15 mm × 6 mm) at 60, 80, 100, 120 and 175 keV (a) and corresponding periphery-to-centre dose ratio as a function of photon energy (b). (from Di Lillo *et al.* 2017a)

2.5   Measurements at Australian Synchrotron

Australian Synchrotron (AS) is a third generation synchrotron facility with a circumference of 216 m operating in "top-up" mode at a nominal electron energy of 3 GeV and a ring current of 200 mA. The rms electron beam size in the straight sections is 320 μm horizontally and 16 μm vertically, corresponding to a Gaussian FWHM of 754 μm and 38 μm, respectively (Stevenson *et al*, 2010, Stevenson *et al*, 2017). The experiments were conducted at Imaging and Medical Beamline (IMBL) of AS. IMBL produces a fan beam of polychromatic radiation from a superconducting multi-pole wiggler (SCMPW) with 60 pole pairs (52 mm period) and a peak magnetic field of 4.0 T (Pelliccia *et al*, 2016). A double-crystal Laue monochromator (DCLM), with the centre at a distance of 16.2 m from the source, is used to select the single energy up to 120 keV (Stevenson *et al*, 2012). IMBL has six hutches: 1A, 2A, and 3A are the "optics" or beam-conditioning hutches, and 1B, 2B, and 3B are the experimental hutches. In each hutch, it is possible to work with monochromatic or pink photon beam.

The measurements were performed in the hutch 3B, situated in a dedicated satellite building providing a source-to-sample distance of approximately 140 m. In this hutch the SR beam, which can reach the size of 500 mm × 40 mm (H × V), has a divergence of 3.8 mrad in the horizontal direction and 0.3 mrad in the vertical direction. The magnetic field of SCMPW was 3.0 T.

2.5.1   First feasibility study at 60 keV

We carried out a first feasibility study of SR^{3}T at a single photon energy of 60 keV. In particular, we performed Monte Carlo simulations and measurements on phantoms for evaluation of radial dose profiles, "skin-to-tumor" dose ratio, and non-uniform dose distributions (dose painting applications). A variety of different dosimeters was used: ionization chamber (IC), radiochromic films and thermoluminescence dosimeters (TLDs).

2.5.1.1   Dosimeters calibration and beam uniformity assessment
As dosimeters for air kerma measurements performed free-in-air or in phantom, we used a 100-mm long pencil ionization chamber (mod. 20X6-3CT, Radcal Corp.,

Monrovia, CA, USA, readout by a Radcal 2026C dosimeter), radiochromic films (GafChromic® EBT3 and XR-QA2, Ashland, KY, USA) and TLD-100 LiF thermoluminescence dosimeters.

The response of the pencil ionization chamber (IC) in the monoenergetic laminar beam at 60 keV was calibrated in terms of air kerma in air with reference to a free-in-air parallel-plate ionization chamber (model ADC IC-105) employed at the IMBL beamline (Crosbie *et al*, 2013, Stevenson *et al*, 2017). For calibration, the pencil chamber was scanned vertically through the SR beam at a constant speed (Prezado *et al*, 2011) and temperature as well as pressure correction was applied. The parallel chamber operated at 2 kV without any windows. In order to obtain different air kerma rate, layers of copper with different thicknesses attenuated the intensity of photon beam. We estimated that the contribution of the $\lambda/3$ (180 keV) for SCMPW (3.0 T) was in the order of 1%.
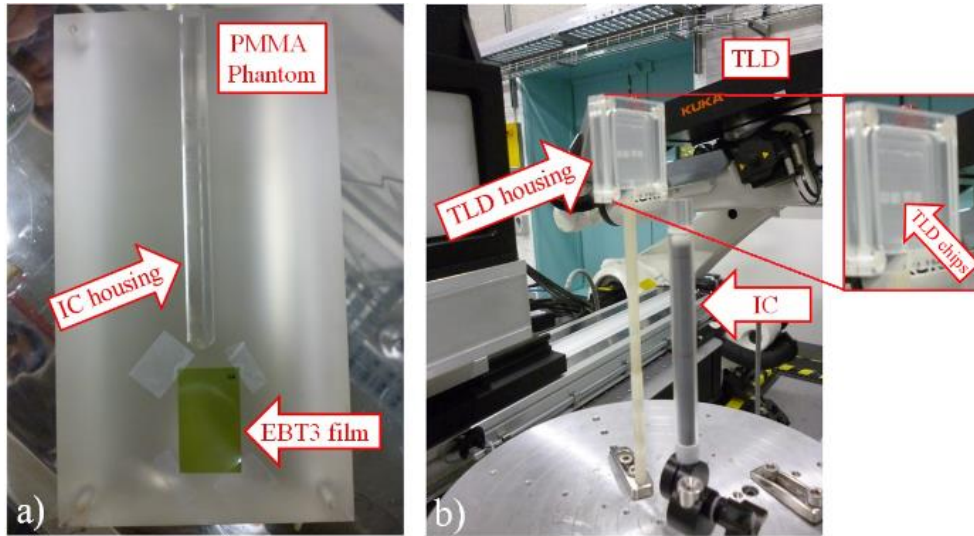
Figure 2.6: a) Photo of the midplane face of the two halves cylindrical PMMA phantom containing a cavity for the ionization chamber and with the EBT3 film in place; b) Setup for TLD irradiation: four TLD chips inserted in the PMMA housing and 100-mm pencil ionization chamber (IC) placed along the vertical direction. The inset shows the four chips in place in the housing. (from Di Lillo *et al.* 2017b)

The response of the radiochromic films EBT3 (lot # 12011401) was calibrated in terms of air kerma evaluated in a polymethylmethacrylate (PMMA) phantom in the range 0.05−2 Gy, while the response of the XR-QA2 films (lot # 10261501) was calibrated in terms of air kerma free-in-air in the range 0.005-0.200 Gy. We used the

calibrated pencil ionization chamber to measure the air kerma. A PMMA cylindrical phantom (14-cm diameter, 25-cm height), composed of two semi-cylinders to permit the film placement and with a cylindrical hole (13-mm diameter) along the cylinder axis, was employed for the EBT3 calibration. During irradiation, the pencil chamber was allocated in the hollow cavity along the cylinder axis, while the film piece was at midplane of the cylinder, at 1 cm from the IC to avoid scatter radiation contamination (Figure 2.6a). The dosimeters placed in the PMMA phantom (for EBT3 calibration) or free-in-air (for XR-QA2 calibration) were translated along the beam height direction at a constant speed because of the laminar beam configuration (Prezado *et al*, 2011 Brown *et al*, 2012). The scanning method mimics an uniform irradiation of dosimeters. Different exposures were obtained by setting different scan speeds. Films were digitized in RGB scanning mode (72 dpi, 48-bit, TIFF image) with an Epson Perfection V750 Pro flat-bed scanner and their response in the red channel was evaluated. Following Devic *et al*, 2016 and Di Lillo *et al*, 2016a, the calibration curve was carried out for EBT3 and XR-QA2 films, respectively. We want to highlight that the same scanning protocol was used for all measurements with radiochromic film performed for the feasibility study at 60 keV (section 2.5.1).

The irradiation protocol for TLD-100s calibration was similar to that used for the radiochromic films. The TLD chips placed in a PMMA housing (Figure 2.6b) (1 mm PMMA upstream and 1mm downstream) were exposed to the SR beam adopting the scanning method (Emiro *et al*, 2015). The dosimeter response was calibrated in terms of air kerma free-in-air measured with the pencil chamber in the range 0.5-1.7 Gy. For each calibration point, the average response of four different TLDs was evaluated.

Figure 2.7 and Figure 2.8 show the calibration curves of the dosimeters response at 60 keV. A linear fit function was employed for the calibration of the pencil chamber response in terms of air kerma rate and for the calibration of the TLDs response in air kerma free-in-air. The film response evaluated in terms of net optical density (*net OD*) for EBT3 and net reflectance change (*netΔR*) for XR-QA2 was correlated by means of a power function with the air kerma measured in the PMMA phantom and air kerma free-in-air, respectively.
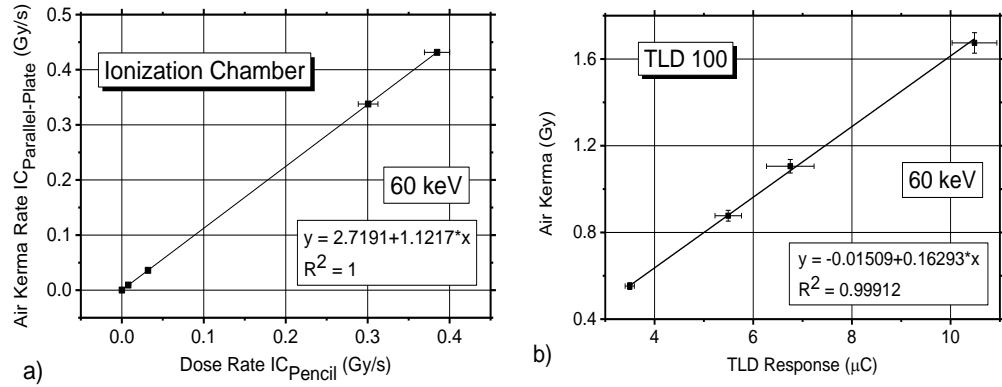
Figure 2.7: Calibration curve for the response of a) the pencil IC and b) TLD dosimeters at 60 keV. The continuous line is a linear fit to the data points. (from Di Lillo *et al.* 2017b)
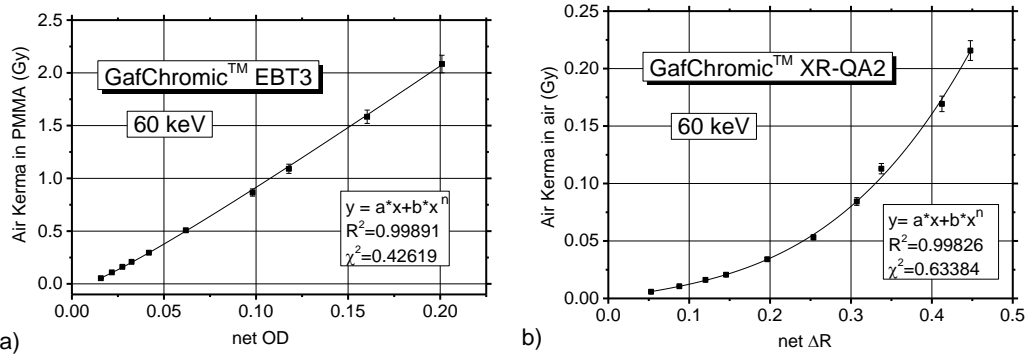
Figure 2.8: Dose-response curves evaluated for a) EBT3 and b) XR-QA2 radiochromic films at 60 keV. The power function indicated on the graphs was employed to fit the experimental data. (from Di Lillo *et al.* 2017b)

A preliminary assessment of the beam uniformity was also performed by imaging the SR beam with a radiochromic film, Gafchromic® XR-QA2. The SR beam size was 15 cm × 1.6 cm (H × V). Following Di Lillo *et al* (2015), the film response was converted to photon fluence per unit air kerma (mm^{-2} mGy^{-1}) providing the 2D distribution of the beam intensity in a plane transverse to the beam axis. Figure 2.9 shows the image of the SR beam acquired with radiochromic film XR-QA2 (Figure 2.9a) and the corresponding horizontal line profile (Figure 2.9b). For comparison, the calculated "Roll-off" curve at 60 keV is showed together with the measured profile. The measurement with radiochromic film yields a maximum variation of the beam flux along the horizontal direction of about 6%, in agreement with theoretical calculation.
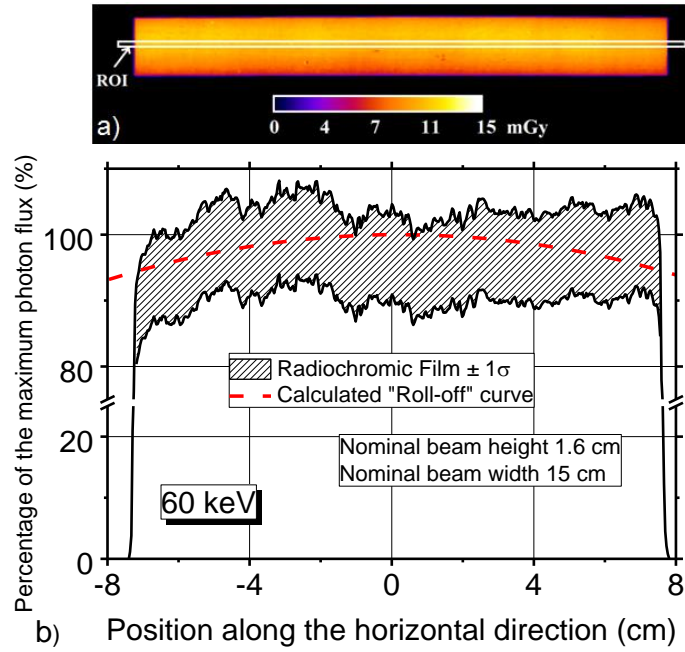
Figure 2.9: a) Dose map of the SR beam at 60 keV acquired with radiochromic film XR-QA2, the film response was calibrated in terms of air kerma in air. b) Horizontal average profile in the ROI shown in a) at 60 keV evaluated in the radiochromic film dose map. The maximum horizontal variation is about 6%. (from Di Lillo *et al.* 2017b)

2.5.1.2 Radial dose profile measurements

The radial dose distribution was evaluated in the same polyethylene (PE) cylindrical phantom (14-cm diameter, 15-cm height) employed for measurement with the orthovoltage X-ray tube (section 2.2.1). We measured the air kerma in the phantom by irradiating the 100-mm pencil chamber at each position during a complete rotation of the phantom. The PE cylinder was placed on an assembly of PMMA slabs (20 × 20 × 18 cm^3) mimicking the chest wall (Figure 2.10). The axis of rotation coincided with the cylinder axis. The radial dose distribution was assessed with SR beam collimated to 0.8 cm vertically and to 1.5, 4, 7, or 15 cm horizontally.
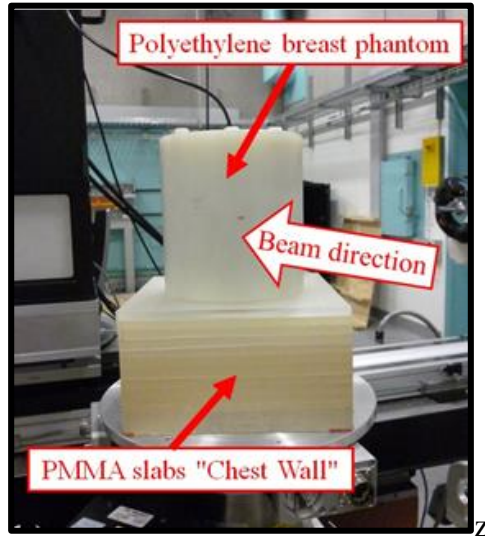
Figure 2.10: Experimental setup for radial dose profile measurement at AS. In this image, the IC is positioned in the central hole of the phantom. (from Di Lillo *et al.* 2017b)

The experimental setup was reproduced with MC code. In order to take into account the length of the pencil chamber, the dose along 100 mm in the direction of the cylinder axis was evaluated for the simulated data. Figure 2.11 shows the comparison between the dose profiles measured in the phantom (symbol) and profiles evaluated via MC simulation (line) at beam widths of 1.5, 4, 7, and 15 cm and a fixed beam height of 8 mm. The agreement in terms of mean percentage difference between simulations and measurements of dose profile at each collimation is within 5%. In particular, a mean percentage difference of 2.8% ± 0.7% and 4.7% ± 2.2% was evaluated for a collimated beam width of 15 and 1.5 cm, respectively. The data show that the shape of the radial dose profile depends on the SR beam width. In particular, for a 15-cm beam width the dose distribution is flat. When the beam width is progressively narrowed, the radial profile becomes peaked at the center of rotation. A periphery-to-center dose ratio of 103%, 48%, 33 %, 17% is estimated via MC simulation for beam width of 15, 7, 4 and 1.5 cm, respectively.
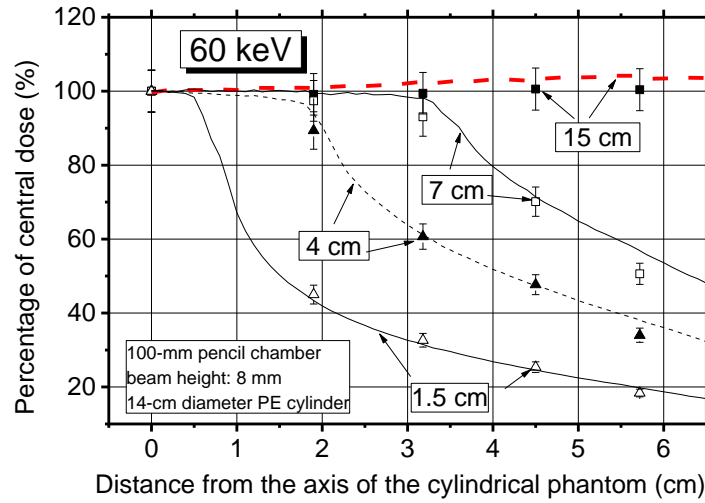
Figure 2.11: Comparison between the measured (symbols) and simulated (lines) relative air kerma in a 14-cm diameter polyethylene cylindrical phantom for beam width of 1.5, 4, 7 and 15 cm. For the MC simulation, the dose distribution was evaluated by integrating the dose along 100 mm in the direction of the cylinder axis. (from Di Lillo *et al.* 2017b)

The dose distributions shown in Figure 2.11 include two components: one due to the energy released in the volume directly irradiated with the 8-mm height beam and a second component due to the energy deposited by the scatter radiation in the phantom volume not directly exposed to the beam. It is of interest to evaluate the extent of the two separate terms in the total dose. Hence, we carried out MC simulations in which we derived the radial profile of the dose distribution in the 14-cm diameter PE phantom due to each separate contribution. Figure 2.12 shows the radial dose distribution obtained by scoring the energy only in the irradiated volume of the phantom (corresponding to ROI 1 in Figure 2.13), or in the zone outside the irradiated volume (reached by scattered photons) (corresponding to ROI 2 + ROI 3 in Figure 2.13), or in the whole volume (where the total dose is the sum of the two components) (corresponding to ROI 1+ ROI 2 + ROI 3 in Figure 2.13). The dose distributions were evaluated in the case of a beam collimated to 1.5 cm in the horizontal direction (Figure 2.12a) or wide beam of 15-cm width (Figure 2.12b). For each profile, the dose was expressed in percent of the central value of the distribution.
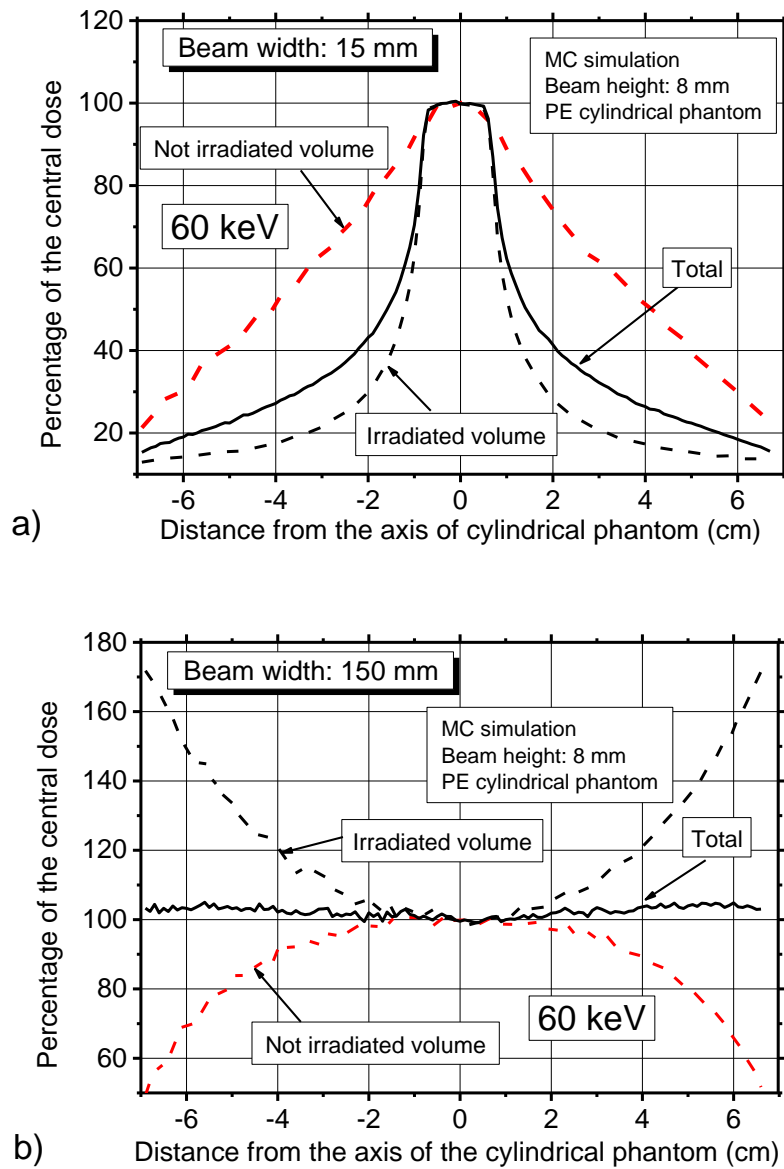
Figure 2.12: Dose profile along a diameter, obtained via MC simulation in a 14-cm diameter polyethylene cylindrical phantom for beam width of a) 1.5 cm and b) 15 cm. For each beam collimation, the dose profile was evaluated scoring the energy in the irradiated volume (ROI 1 in Figure 2.13), in the not irradiated volume (ROI 2 + ROI 3 in Figure 2.13) and in whole volume used for the measurements (ROI 1+ ROI 2 + ROI 3 in Figure 2.13). Each profile was normalized to its central value (from Di Lillo *et al.* 2017b)
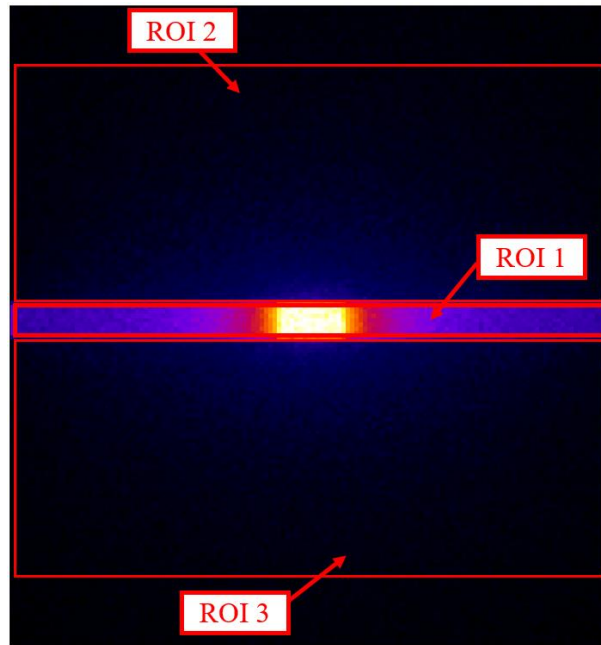
Figure 2.13: 2D map of the energy released in the 14-cm PE cylindrical phantom. The map was obtained via MC simulation. The ROIs used for evaluation of the dose distribution reported in figure 2.12 are showed.

For the collimated beam (Figure 2.12a), the dose profile in the irradiated volume is peaked at the center of rotation showing a dose distribution different from that evaluated in the whole volume. The dose profile in the not irradiated volume has a triangular shape with a maximum value at the rotation centre.

The irradiation with the wide beam (Figure 2.12b) produces a cupped dose distribution in the irradiated volume because of the exponential attenuation of X-ray beam in the material, which provides a greater dose deposit at the periphery. A domed profile characterizes the dose distribution in the not irradiated volume and the combined effect of these two contributions results in a flat dose distribution in the total volume. For comparison, Figure 2.14 shows the radial distributions obtained scoring the energy only in the irradiated volume for different beam widths (from 1.5 to 15 cm) at 60 keV. A periphery-to-centre dose ratio of about 171%, 62%, 35% and 14% is estimated for beam width collimations of 15, 7, 4, and 1.5 cm, respectively.
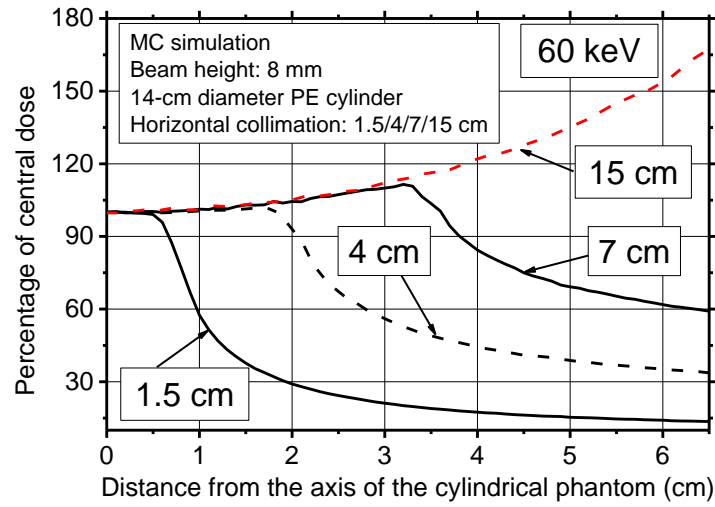
Figure 2.14: Dose profile obtained via MC simulation in a 14-cm diameter polyethylene cylindrical phantom, for various widths of the horizontal collimation (from 1.5 cm to 15 cm). The dose profile was evaluated in the irradiated phantom slice. (from Di Lillo *et al.* 2017b)

2.5.1.3 *Assessment of the periphery-to-center dose ratio with radiochromic film and TLD*

We estimated the periphery-to-center dose ratio in a 14-cm diameter PMMA cylindrical phantom by measuring the air kerma at the phantom axis (centre) and at 4 cm from the axis (periphery) during a complete rotation of the phantom. Air kerma measurements were made with both radiochromic film EBT3 and TLD-100. The cross-section of the SR beam was 15 mm (H) $\times$ 16 mm (V). A cylinder with two 13-mm diameter cavities was used for measurements with TLD-100. Ten TLD chips filling the cavity were irradiated at each position and the average of their response was used to calculate the dose ratio. Radiochromic film were placed at midplane of the same phantom used for the calibration. The dose ratio was calculated by estimating the mean pixel value, calibrated in terms of air kerma, in two ROIs (centre and periphery) of area 3 mm $\times$ 3 mm. Table 2.2 reports the periphery-to-centre dose ratio at 4 cm from the cylinder axis measured with radiochromic film EBT3 and with TLDs. A dose ratio of 24% $\pm$ 3% was estimated with TLD chips, in agreement with simulation result within the experimental error. However, a dose ratio of 47% $\pm$ 3% was evaluated with radiochromic film. We investigated this discrepancy and attributed it, at least in part, to the process of film scanning. The films were scanned with the Scanner EPSON V750 PRO which has been in use in our laboratory for

many years. We noticed the onset of an artefact with excess pixel values on one side of the scanning field, which may produce alteration of the line profile measured with the film dosimeters. A new scanner EpsonV850 PRO was bought, but was available only in the last part of this thesis work.

Table 2.2: Periphery-to-center dose ratio simulated with MC code and measured with TLD100, radiochromic film EBT for a SR beam collimated at 1.5 cm along the horizontal direction at 60 keV. (from Di Lillo *et al.* 2017b)

	Periphery-to-center dose ratio (%)
Radiochromic film EBT3	47 ± 3
TLD-100	24 ± 3
MC Simulation	22.2 ± 0.3

2.5.1.4 Dose painting application

The feasibility of dose painting applications was studied by performing measurements with radiochromic film. Pieces of radiochromic film EBT3 of size 12 cm × 5 cm (H × V) were positioned at mid-plane of a 14-cm diameter PMMA cylinder phantom placed at the isocenter. A collimated SR beam of size 1.5 cm × 1.6 cm (H × V) irradiated the phantom at air kerma rate free-in-air of 2.22 Gy/min. Non-uniform dose distributions – two-off center foci and a linear distribution of three hot spots – were obtained with multiple rotations of phantom shifting laterally the axis of rotation. The two off-center foci were irradiated by shifting the axis of rotation 3.96 cm. The rotation speed was set at 10 °/s for the first turn (for delivering 0.6 Gy to the first focus) and at 5 °/s for the second turn (with 1.2 Gy delivered to the second focus). The three hot spots were obtained by rotating three times the phantom with a speed of 10°/s and shifting laterally the center of rotation by 0.75 cm at each rotation. Figure 2.15 and Figure 2.16 show the non-uniform dose distributions (two off-center foci and linear distribution of three hot spots) evaluated with both measurements (Figure 2.15) and MC simulations (Figure 2.16). The experimental dose distributions were evaluated averaging the dose profile in a ROI of size 11.5×1.2 cm on the radiochromic film images, as shown in Figure 2.15. The same approach was used to evaluate the dose distribution with MC simulation. The surface plots of the percentage of the maximum dose is also reported. The dose distribution is reported as percentage of the maximum dose.
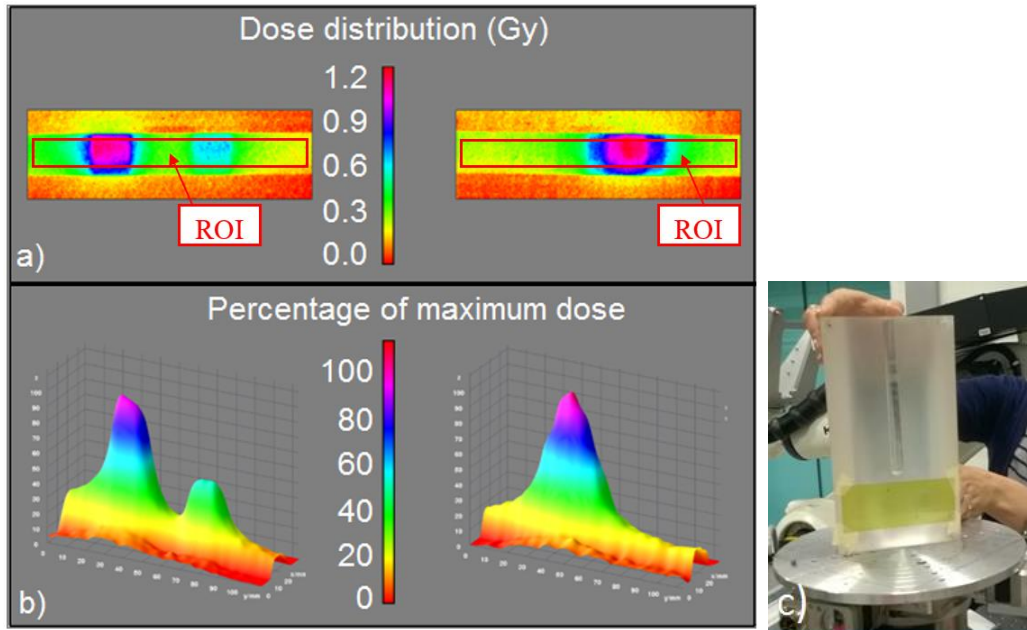
Figure 2.15: a) 2D dose distributions evaluated with radiochromic film EBT3 in a 14-cm diameter PMMA phantom and b) corresponding surface plots of percentage of maximum dose: two off-center foci (left side) and line distribution (right side). ROIs where the average dose distributions were evaluated are showed. The intended dose distribution was obtained with multiple rotations. c) Showing, for ease of visualization of the sample geometry, a photo taken during the placement of one half of the cylindrical phantom on the rotation stage, where the piece of EBT3 film is visible at mid-plane in the PMMA phantom. Above the film is visible the half cavity realized for hosting the ion chamber. (from Di Lillo *et al.* 2017b)
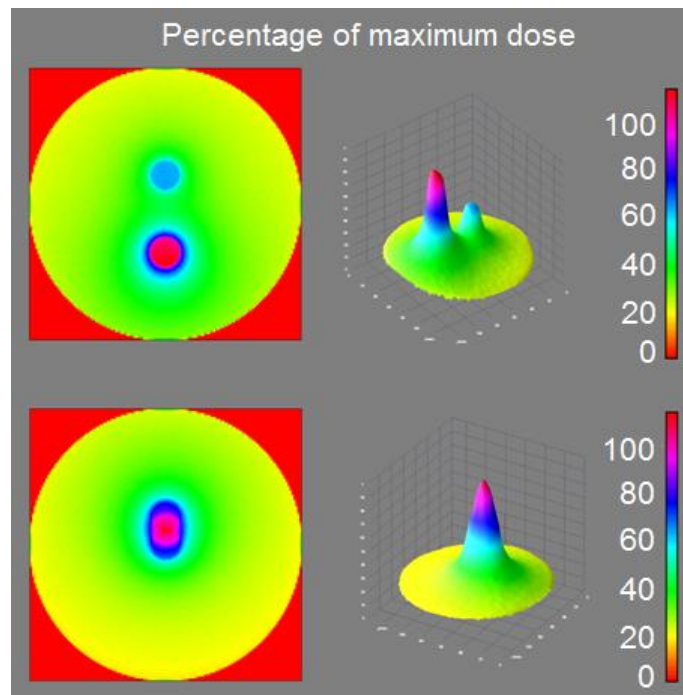
Figure 2.16: Two off-center foci and line dose distributions in a 14-cm diameter PMMA phantom obtained via MC simulations and line dose profiles evaluated in terms of percentage of maximum dose. (from Di Lillo *et al.* 2017b)

The two off-centre foci irradiation resulted in two target doses of about 1.2 Gy and 0.6 Gy with the low-dose focus near the centre of phantom. Both experimental and MC data show a flat dose distribution inside the low-dose focus, while the dose increases by increasing the distance from the phantom centre inside the other focus because of the X-ray attenuation in the phantom (Figure 2.17a). The overlap of the two dose distributions produces a dose deposition of about 30% of the maximal dose at the edge nearest the high-dose focus. At the opposite edge, measurements and MC simulation provide two different values of dose: 10% and 20% of the maximal dose, respectively.
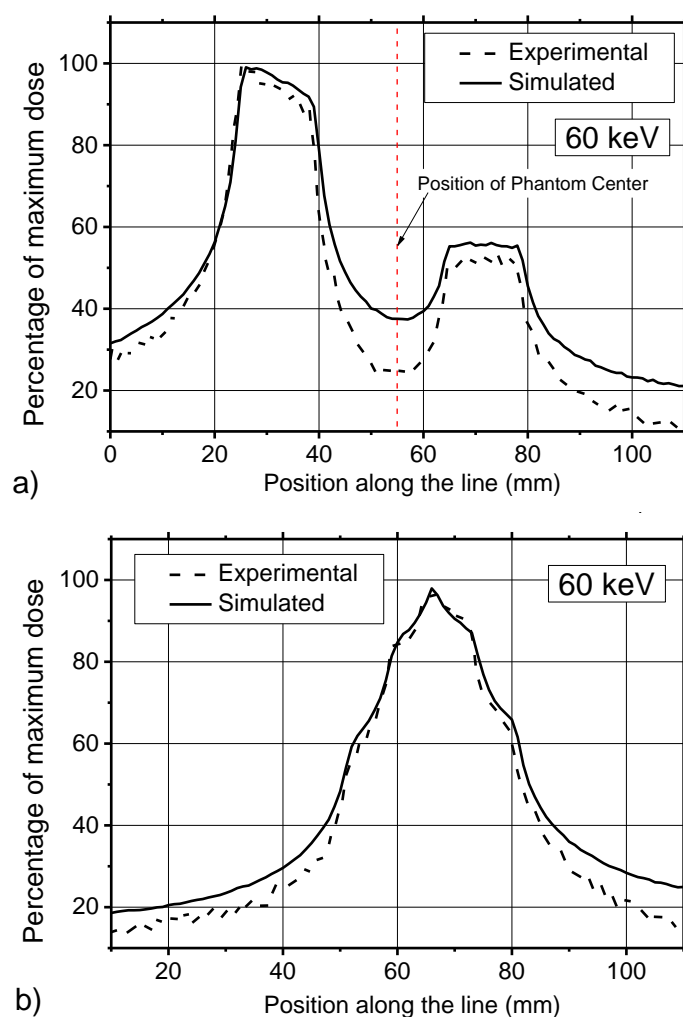
Figure 2.17: Line dose profiles of the percentage of maximum dose for 60-keV irradiation of a) two off-center foci or b) for a linear distribution. For the two foci irradiation, the centre of the phantom was also indicated at position 55 mm. Dashed line: experimental; continuous line: simulated data. (from Di Lillo *et al.* 2017b)

The linear distribution of three hot spots resulted in a wide-peak profile with a non-smooth shape due to the overlap of the hot spots. A dose deposition of 25% of the maximal dose is estimated at 3 cm from the peak of the dose distribution via measurements, while a dose value of 30% is calculated at the same distance with data from MC simulation (Figure 2.17b). Although the dose profiles obtained with the two different data sets (measurements and MC simulations) demonstrated similar shapes, we point out that a discrepancy exists between simulated and measured data, as it was shown in Figure 2.17. We have attributed this disagreement to the response of the radiochromic film to the rotational irradiation at low energy. In addition, we want to underline the choice of the normalization point could influence the behaviour of this discrepancy. In future works, a gamma test index (used in clinical routine for the evaluation of the treatment planning process) will be used to provide a better evaluation of the performance of the delivered dose strategy.

2.5.2   Study of SR^{3}T at high energy

After the feasibility study at 60 keV, the investigation on SR^{3}T was extended at higher energy with measurements of radial dose profile and dose distributions in phantom at 80 and 100 keV.

2.5.2.1   Profile of X-ray beams

An evaluation of the beam profiles at 80 and 100 keV was performed with radiochromic film EBT3. A procedure similar to that reported in Di Lillo *et al* (2015) and used in section 2.5.1 was employed. The radiochromic film were scanned with EPSON V850 PRO in RGB mode (72 dpi, 48-bit, TIFF image). Their response in the red channel was calibrated in terms of photon fluence obtaining the 2D distribution of the beam intensity. The horizontal beam profiles evaluated in the centre of the beam height at 80 keV and 100 keV are reported in Figure 2.18.
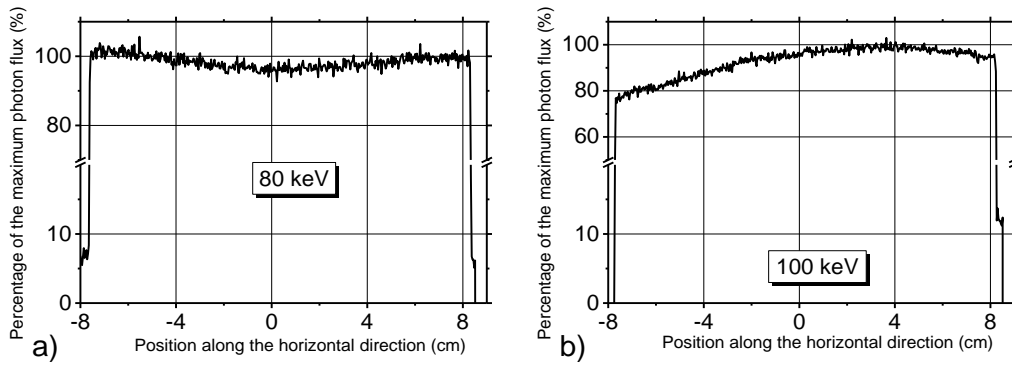
Figure 2.18: Horizontal average profile in a ROI evaluated in the radiochromic film dose map at 80 keV (a) and 100 keV (b). The position 0 corresponds to the center of the beam.

The profiles were normalized at the maximum photon flux. A maximum variation of 6% along 16 cm was observed at 80 keV with a minimum in the centre of beam. The beam profile at 100 keV is asymmetric with minimum value on an edge of 80 % of the maximum photon flux. This indicates that the beam collimation was likely not symmetric in respect to the beam centre.

2.5.2.2 Radial Dose Profile

Measurements of radial dose profile in a 14-cm diameter PE cylindrical phantom were performed at 60, 80 and 100 keV using a semiflex ionization chamber (PTW 31010) with the dosimeter T10023 UNIDOS webline. The chamber was firstly calibrated in terms of air kerma free-in-air with reference to the ADC IC-105 chamber of IMBL at each energy employing the calibration protocol already reported for the pencil chamber in the feasibility study at 60 keV (section 2.5.1.1). The use of this chamber permits to avoid trouble due to the partial irradiation of the dosimeter (section 2.5.1.2) because the X-ray beam height available at IMBL can be larger than the dosimeter size – sensitive volume 2.75 mm-radius, 6.5-mm-length (http://www.ptw.de/semiflex_chambers0.html). The radial dose profiles were evaluated with the same measurements protocol used for the feasibility study at 60 keV(section 2.5.1.2). The beam height was fixed at 1.0 cm. The radial dose profile were acquired at beam width of 1.5, 4, 5.5, 7, or 16 cm. The air kerma rate at the centre of the phantom and the rotation speed were 152 mGy/s and 15 °/s at 60 keV, 66.7 mGy/s and 10°/s at 80 keV, 28.7 mGy/s and 5°/s at 100 keV. The experiment was also simulated with the MC code (section 2.4).
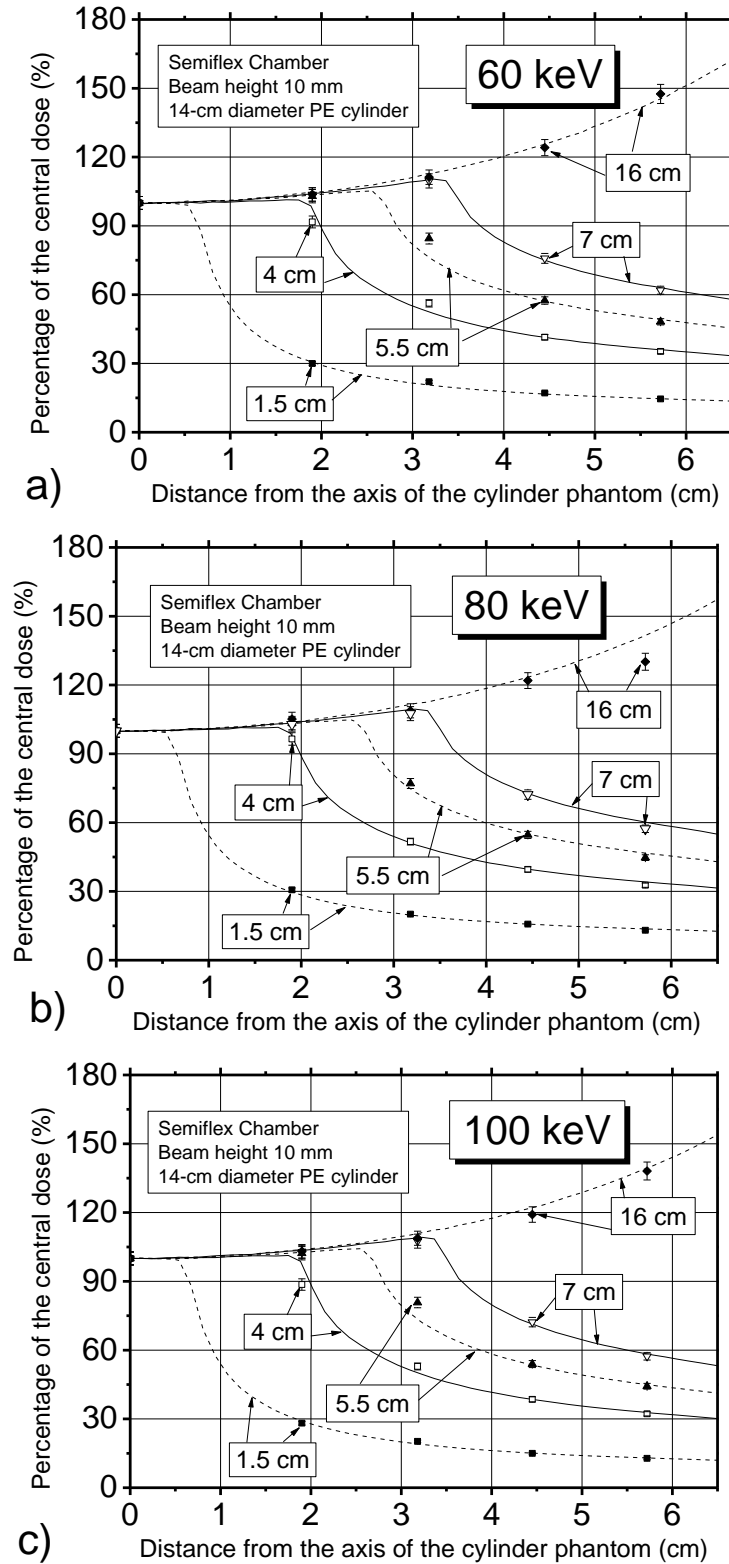
Figure 2.19: Comparison between the measured (symbols) and simulated (lines) relative air kerma in a 14-cm diameter polyethylene cylindrical phantom for beam width of 1.5, 4, 5.5, 7 and 16 cm at 60 keV (a), 80 keV (b), and 100 keV (c).

Table 2.3: Mean percentage difference in the dose distribution between measurements and MC simulations evaluated for beam collimations of 1.5, 4, 5.5, 7, and 16 cm at 60, 80, and 100 keV.

Collimation of X-ray beam (cm)	Mean Percentage Difference (%)		
	60 keV	80 keV	100 keV
16.0	1.5 ± 0.8	4 ± 3	2 ± 1
7.0	1.4 ± 1.3	3 ± 2	1.7 ± 1.3
5.5	4 ± 5	3 ± 2	3 ± 4
4.0	5 ± 3	2.6 ± 0.9	5 ± 5
1.5	4 ± 3	2.8 ± 0.9	3 ± 3

Figure 2.19 shows the radial dose distributions carried out from measurements as well as from simulations at 60 keV, 80 keV, 100 keV. As already shown in section 2.5.1.2, the radial dose distribution depends on the beam collimation. A cupped profile with a minimum in the centre of the phantom was observed for beam width of 16 cm, while a dose distribution peaked in the centre of rotation results for 1-cm collimated beam. The comparison between measurements and simulations shows a good agreement. The analysis of data reveals mean percentage difference in the dose distribution between simulations and experimental data less than 5% (Table 2.3). The periphery-to-centre dose ratio was evaluated at 5.72 cm (1.5, 4, 5.5, 7, and 16 cm) at each energy (60, 80, and 100 keV) by using the results from measurements. The same evaluation was carried out at 6.5 cm via MC simulations.Table 2.4 and Table 2.5 summarizes the estimated values. The dose ratio decreases with increasing the beam collimation in the horizontal direction at fixed energy. This behaviour is due the principle of rotational summation of dose. In particular, periphery-to-centre dose ratio ranges between 13.4% and 164 % at 60 keV, 12.5% and 160% at 80 keV, and 11.9% and 156% at 100 keV at 6.5 cm. Moreover, a decrement of the dose ratio increasing the photon energy was observed at each beam collimation. A similar result was reported in section 2.4.1 for a beam of size 1.5 cm $\times$ 0.6 cm.

Table 2.4: Periphery-to-center dose ratio evaluated at 5.72 cm with measurements for beam collimations of 1.5, 4, 5.5, 7, and 16 cm at 60, 80, and 100 keV.

Collimation of X-ray beam (cm)	Periphery-to-centre dose ratio (%)		
	60 keV	80 keV	100 keV
16.0	147 ± 4	130 ± 4	138 ± 4
7.0	61.9 ± 1.8	63.2 ± 1.8	57.3 ± 1.6
5.5	48.2 ± 1.4	44.7 ± 1.3	44.3 ± 1.3
4.0	35.3 ± 0.9	32.7 ± 0.9	32.2 ± 0.4
1.5	14.5 ± 0.4	13.1 ± 0.4	12.8 ± 0.4

However, we note that the dose ratio evaluated at 5.72 cm via measurements for a 16-cm width beam at 80 keV is lower than that obtained at 100 keV. This could be attributed to troubles during the measurement. Indeed, the experimental result at 80 keV is also lower than the expected value as shown in the comparison between measurements and simulations at 80 keV (Figure 2.19): simulation provides a ratio of about 142% instead of 130% measured at the same distance. Figure 2.20 shows the periphery-to-centre dose ratio evaluated at 6.5 cm via MC simulation as a function of the photon energy. In spite of energy dependence, the values of dose ratios obtained at different energies are in the same magnitude order at fixed collimation, e.g. from 11.9% at 100 keV to 13.4% at 60 keV. This means that in terms of skin sparing there is not a large difference in using photons at 60 keV or 100 keV (see also Figure 2.5)). Moreover, the photoelectric absorption at the tumour at energies lower than 100 keV is higher than that at 320 kV or 6 MV. These considerations encourage us to investigate the use of dose-enhancement agents at low energy (e.g. below 100 keV). A preliminary study on the use of these agents is reported in section 2.7.

Table 2.5: Periphery-to-center dose ratio evaluated at 6.5 cm via MC simulations for beam collimations of 1.5, 4, 5.5, 7, and 16 cm at 60, 80, and 100 keV.

Collimation of X-ray beam (cm)	Periphery-to-centre dose ratio (%)		
	60 keV	80 keV	100 keV
16.0	164 ± 3	160 ± 2	156 ± 2
7.0	57.2 ± 0.9	54.3 ± 0.8	52.5 ± 0.8
5.5	44.8 ± 0.7	42.4 ± 0.6	40.7 ± 0.6
4.0	32.9 ± 0.5	31.1 ± 0.5	29.8 ± 0.4
1.5	13.4 ± 0.2	12.5 ±0.2	11.9 ± 0.2
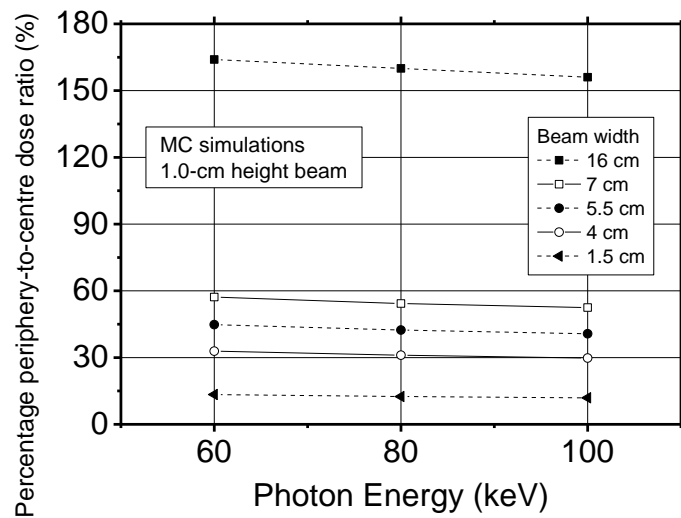
Figure 2.20: Percentage periphery-to-centre dose ratio obtained via MC simulations as a function of photon energy. The beam height was fixed at 1.5 cm, the beam width was set at 16, 7, 5.5, 4, or 1 cm. The periphery value was evaluated at 6.5 cm.

2.5.2.3 *Dose distribution in phantom*

The dose distribution in a 14-cm PMMA cylindrical phantom was evaluated with radiochromic film EBT3 at 100 keV. We used the same 14-cm diameter cylindrical phantom employed for the EBT3 calibration in the feasibility study at 60 keV (section 2.5.1). Pieces of radiochromic film were placed at mid-plane in the phantom to image the 2D dose map produced by the irradiation of a target volume in the centre of phantom. A flat-bed scanner EPSON V850PRO digitized the films in RGB scanning mode (72 dpi, 48-bit, TIFF image). The radiochromic film were previously calibrated in terms of air kerma free-in-air (Figure 2.21) by using a power function.
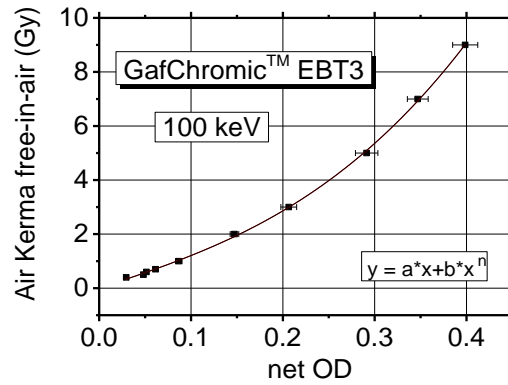
Figure 2.21: Calibration curve for the response of radiochromic film EBT3 at 100 keV. The continuous line is a fit with a power function to the data points.

We recorded the dose distribution obtained with a SR beam of size 1.5 cm × 1.0 cm (H × V) at 100 keV with a piece of film of size (5 cm × 18 cm). The 14-cm diameter PMMA phantom rotated by 360° at a speed of 15°/s during the irradiation. We measured an air kerma rate in the phantom of 21 mGy/s at the central axis of the cylinder. The linear profile along the horizontal direction is reported in Figure 2.22. As expected because of the principle of dose summation and as already reported in the previous sections, the film recorded a dose distribution peaked in the centre of rotation for that narrow beam. The flat part of the profile has an extension of about 1.5 cm, equal to the horizontal size of the irradiating beam, and indicates a target air kerma of about 0.6 Gy. The full width half maximum of the distribution is 2-cm wide. The air kerma profile outside the target decreases with the distance from the axis of rotation with an exponential behaviour, as shown in Figure 2.22. Please note that the line profile extended for a width of 18 cm, since the film pieces was larger than the diameter of the phantom (14 cm).
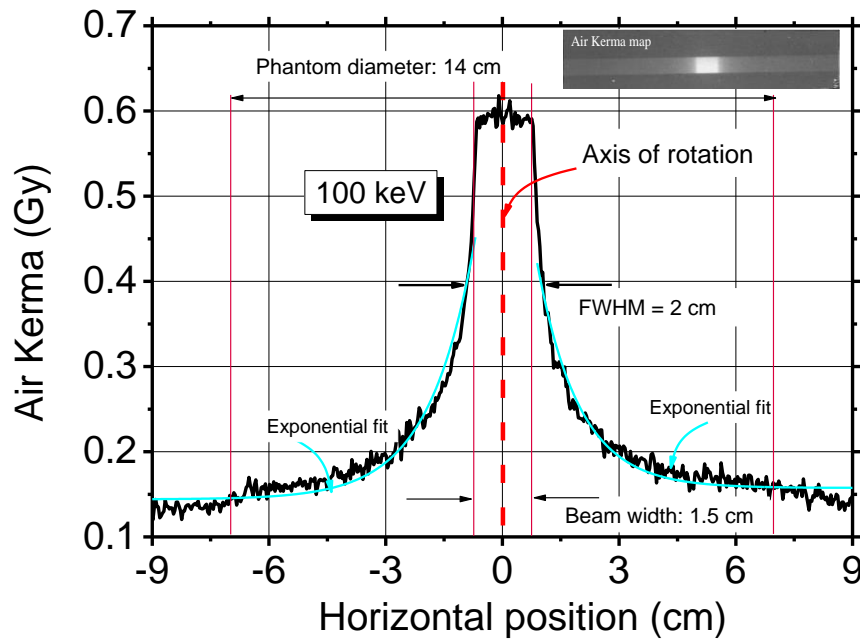
Figure 2.22: Line dose profile along the horizontal direction evaluated with radiochromic film for the irradiation of a single spot in the centre of the 14-cm diameter PMMA phantom. The beam size was 1.5 cm × 1.0 cm (H×V). The inset shows the 2D air kerma map imaged by film. The cyan continuous lines are exponential fits to the left-hand and right-hand side tails of the distribution.
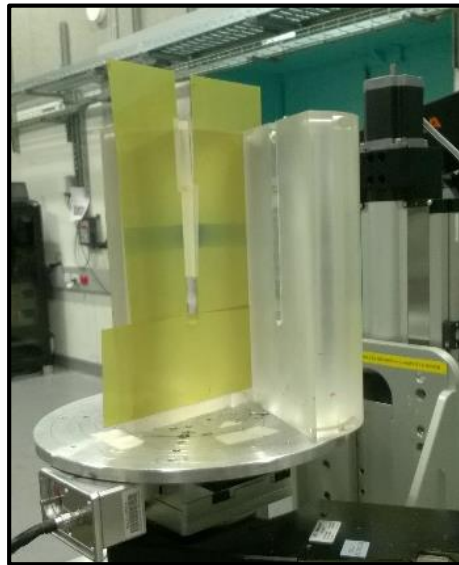
Figure 2.23: Experimental setup for dose distribution measurement at AS. Three pieces of radiochromic film were placed at mid-plane of the 14-cm PMMA cylindrical phantom. The longitudinal section of the phantom was covered with film with the exception of a small rectangular area in the centre.

The previous measurement provides the radial dose distribution at mid-plane only in the volume directly irradiated with SR beam. In order to evaluate the dose distribution in the whole phantom volume, three radiochromic pieces (8.5 cm × 20.3 cm) were placed at mid-plane in the phantom (Figure 2.23). X-ray beam of size 1.5

cm × 2.0 cm (H×V) irradiated the phantom at air kerma rate in phantom of 23.1 mGy/s. The rotation speed was set at 1°/s. The 2D dose map acquired with radiochromic film at mid-plane of the cylinder during a complete rotation of the phantom is shown in Figure 2.24. We assembled the images from each film taking into account their position during the irradiation. The dark area in the centre along the vertical direction corresponds to that non-covered by radiochromic film: pixel values in this region were set to 0. The collimated X-ray beam irradiated a volume resulting in a rectangular area along the diameter direction on the 2D map with a dose target of about 7 Gy in the centre of the phantom. The target is partially visible in the dose map. The isodose curves are showed in Figure 2.25. A dose from 2% and 10% of the maximum value was measured in the phantom area which was not directly irradiated by the X-ray beam. This dose is due to the energy released by scatter radiation. Figure 2.26 shows the line profiles along the vertical direction evaluated at 1 cm (ROI 1 in Figure 2.24) and 5 cm from the cylinder axis (ROI 2 in Figure 2.24). Both of profiles were normalized to the maximum value of the 2D dose map. They show a peak corresponding to the positions where the ROIs used for the profile estimation cross the area directly irradiated by the primary beam. The peaks are asymmetric because of the vertical photon distribution of the SR beam. The profile at 1 cm from the cylinder axis has a peak value of 100% corresponding to the dose target, while a peak value of 23% was estimated from the vertical dose profile at 5 cm from the axis. The dose evaluated at 5 cm from the beam centre position in the vertical direction was about 5% of the maximum value in ROI 1 and 3% of the maximum value in ROI 2. Please note that the part of the radiochromic film was out of the phantom and that the phantom top surface was at about 8 cm from the beam centre along the vertical direction.
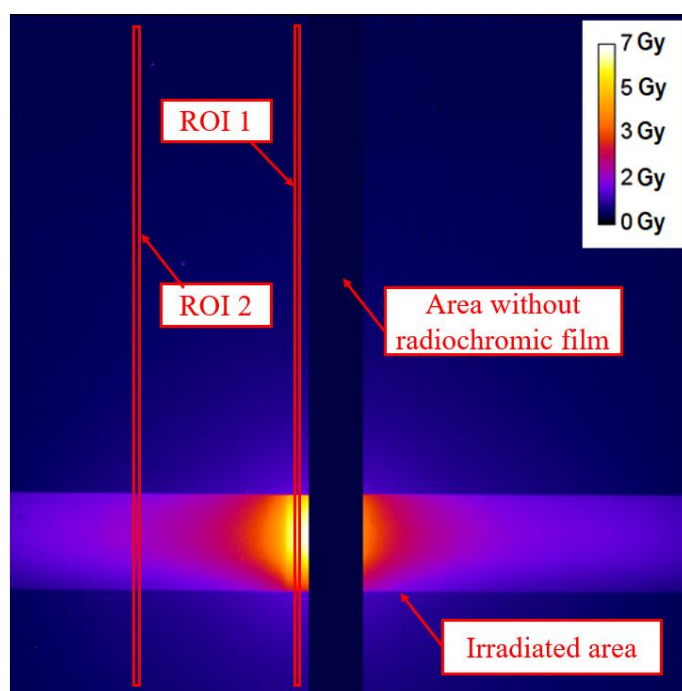
Figure 2.24: 2D dose map at mid-plane in a 14-cm PMMA cylindrical phantom. The pixel values are air kerma free-in-air in Gy.
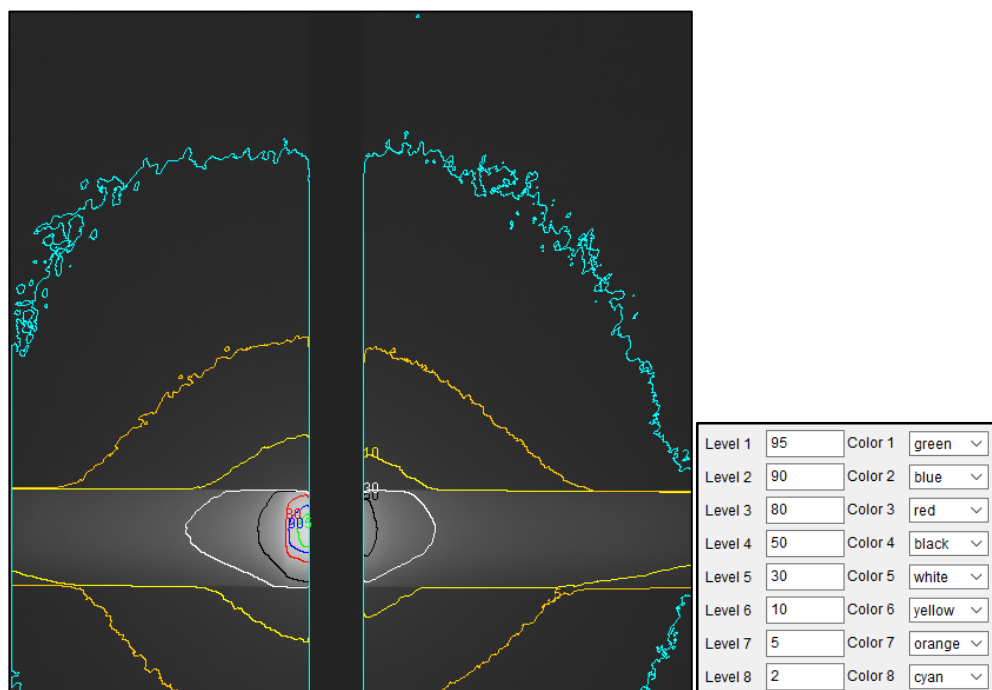
Figure 2.25: Isodose Curves obtained using a X-ray beam collimated at 1.5 cm in the horizontal direction. The dose distribution was evaluated in a 14-cm PMMA cylindrical phantom. The pixel value were normalized to the maximum. The isodose legends in percent of the maximum dose are indicated on the subpanel on the right side.
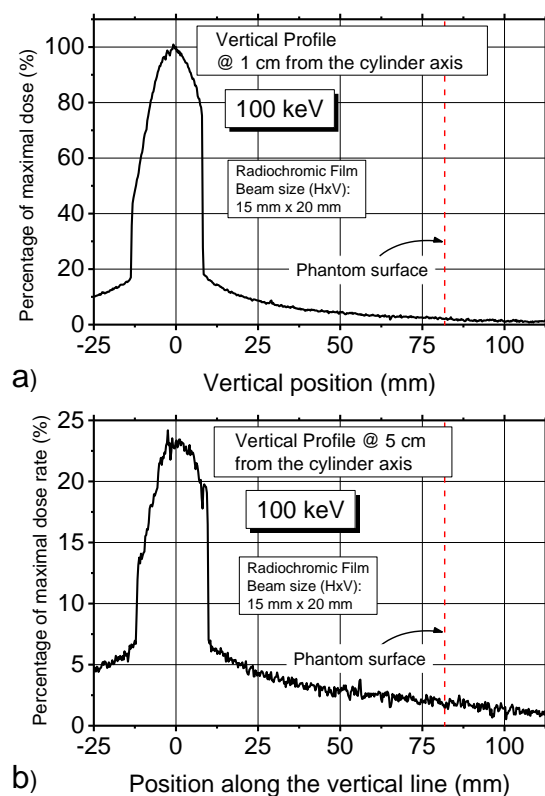
Figure 2.26: Vertical average profile evaluated in the radiochromic film dose map at 1 cm (a) and 5 cm (b) from the cylinder axis at 100 keV.
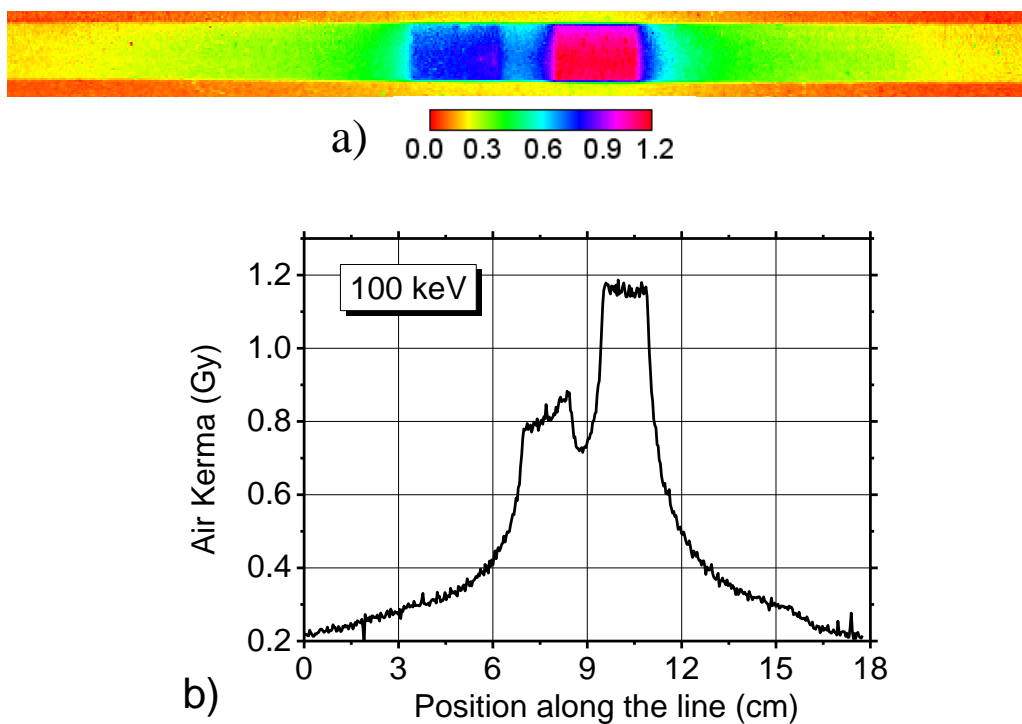
Figure 2.27: 2D dose distributions and evaluated with radiochromic film EBT3 in a 14-cm diameter PMMA phantom at 100 keV and b) corresponding line dose profile. The intended dose distribution (two foci) was obtained with two rotations by shifting the center of rotation 2.5 cm.

We also investigated the dose distribution produced by two foci irradiation with a beam of size 1.5 cm × 1.0 cm (H × V) at 100 keV. Dose painting technique reported in section 2.5.1.4 was employed for the irradiation. In particular, two irradiations – one per each focus – were performed by shifting 2.5 cm the axis of rotation. The rotation speed was set at 15°/s for the first turn and 8 °/s for the second one. The air kerma rate in phantom was 21 mGy/s. The dose distribution was acquired with a piece of radiochromic film EBT3 (20 cm × 4 cm) at mid-plane in the 14-cm PMMA phantom (Figure 2.27a). The line dose profile is shown in Figure 2.27b. The irradiation resulted in a focus of higher dose of about 1.15 Gy and a second focus of about 0.8 Gy. The profile also reveals that in the low-dose focus the dose decrease with the increment of the distance from the other focus because of the overlap of the two dose distributions.

Finally, an evaluation of the dose due to the scatter radiation in the 14-cm diameter PMMA cylinder along the phantom axis was performed with the semiflex ionization chamber at 100 keV. The dosimeter was placed in the phantom at 7 cm from the top surface. The phantom was translated along the vertical direction in step of 5 mm for a total path of 150 mm so that the X-ray beam of size 1.5 cm×2.0 cm (HxV) irradiated different sections of the object at each step. The air kerma rate was measured at each step. The acquired profile is shown in Figure 2.28. We observed a distribution peaked at the phantom position where the X-ray beam directly irradiated the ionization chamber. A dose rate 6.2% of the maximum value were evaluated for the X-ray beam irradiating the phantom at 5 cm from the ionization chamber.
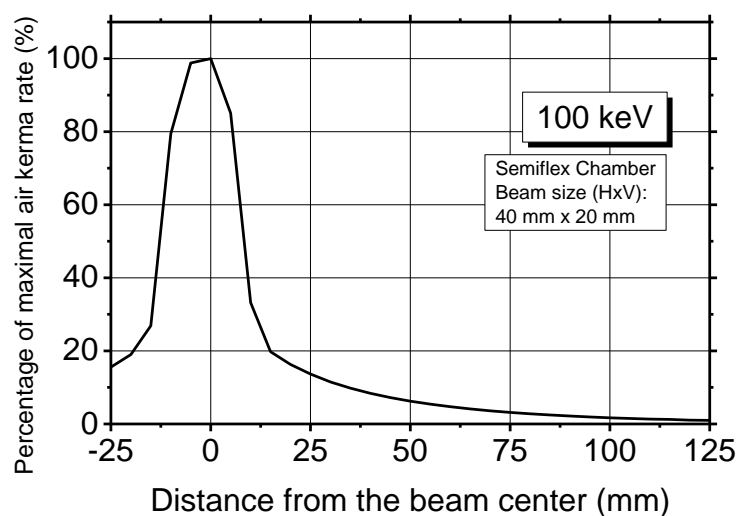
Figure 2.28: Vertical air kerma rate profile evaluated in 14-cm diameter PMMA phantom along the cylinder axis with the semiflex ionization chamber at 100 keV. The dose rates were normalized to the maximum.

2.6 Measurements at the European Synchrotron Radiation Facility

The European Synchrotron Radiation Facility (ESRF) is one of the most brilliant third generation SR source in the world. It operated at a nominal electron energy of 6 GeV and a ring current ranging from 40 mA to 200 mA depending on the filling mode (see http://www.esrf.eu/home/UsersAndScience/Accelerators.html). The ID17 is the beamline dedicated to the biomedical applications such as radiotherapy, radiobiology and biomedical imaging. The X-ray source is a multi-pole wiggler magnet (W150) with 21 poles (period of 15 cm) and a maximum magnetic field of 1.6 T at the minimum allowed gap (24.8 mm) (Mittone, 2014b) corresponding to a maximal critical energy of 38.1 keV. If a higher photon flux is required, a second wiggler (W125) can be employed. W125 has 22 poles (12.5-cm period) and a maximum magnetic field of 1.8 T at a gap of 11 mm (Mittone, 2014b). ID17 includes two optical hutches corresponding to two experimental hutches. The first experimental hutch is at 40 m from the source and is dedicated to study for microbeam, mini beam and pencil beam radiotherapy as well as image-guided brain surgery by using a filtered white beam in the energy range 40 keV−600 keV (see http://www.esrf.eu/UsersAndScience/Experiments/CBS/ID17). The experiments

with monoenergetic X-ray beam are conducted in the second hutch placed at 150 m from the source. The high distance from the source permits to obtain an high degree of spatial coherence and an X-ray beam of size up to $150 \times 7 mm^2$ (H×V) (http://www.esrf.eu/UsersAndScience/Experiments/CBS/ID17). Two different systems of monochromators are available to produce the monoenergetic X-ray beam. The first one is a Si-bent Laue crystal used for angiography, the second is a fixed-exit monochromator composed of two water-cooled bent Si crystals in Laue geometry, which can nominally select energy up to 80 keV (Mittone, 2014b, http://www.esrf.eu/UsersAndScience/Experiments/CBS/ID17). However, X-ray beam with higher energy can be obtained with the monochromator working in particular conditions. The measurements performed at ESRF represent an extension of the first feasibility study at 60 keV conducted at AS and reported in section 2.5.1. The goal was to investigate the use of the SR^3T at energy higher than 60 keV. For this purpose, the same measurements performed for the feasibility study were taken at energies in the range 80–175 keV.

2.6.1 *Profile of the X-ray beams*

The X-ray beam was imaged with radiochromic film Gafchromic XR-QA2 at 80, 100, 120, and 175 keV. The horizontal profiles are shown in Figure 2.29 reporting the photon flux normalized at the maximum as a function of the position along the horizontal direction. We observe that the flux distribution turns more and more narrow with increasing the photon energy. In addition, beam profiles have a non-symmetric structure at each energy. In particular, the variation of the beam intensity was estimated to be about 25% at 80 keV up to about 50% at 120 keV. The asymmetry might be due to the fact that the monochromator crystal was not in optimal Bragg position during the measurement.
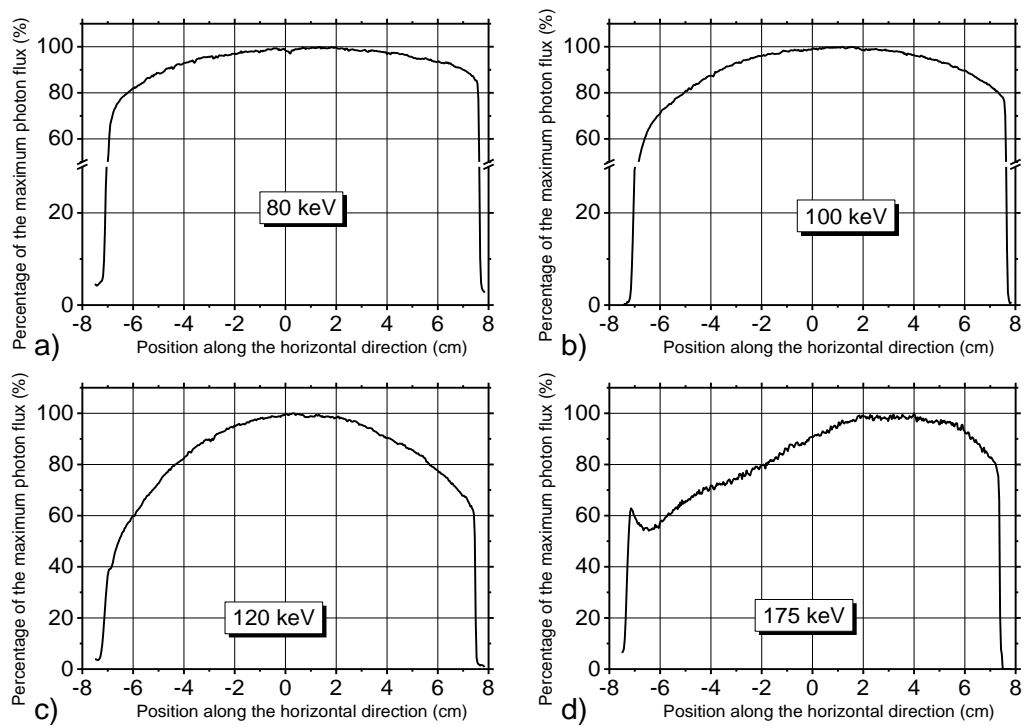
Figure 2.29: Horizontal average profile in a ROI evaluated in the radiochromic film dose map at 80 keV (a), 100 keV (b), 120 keV (c), and 175 keV (d). The position 0 corresponds to the center of the beam.
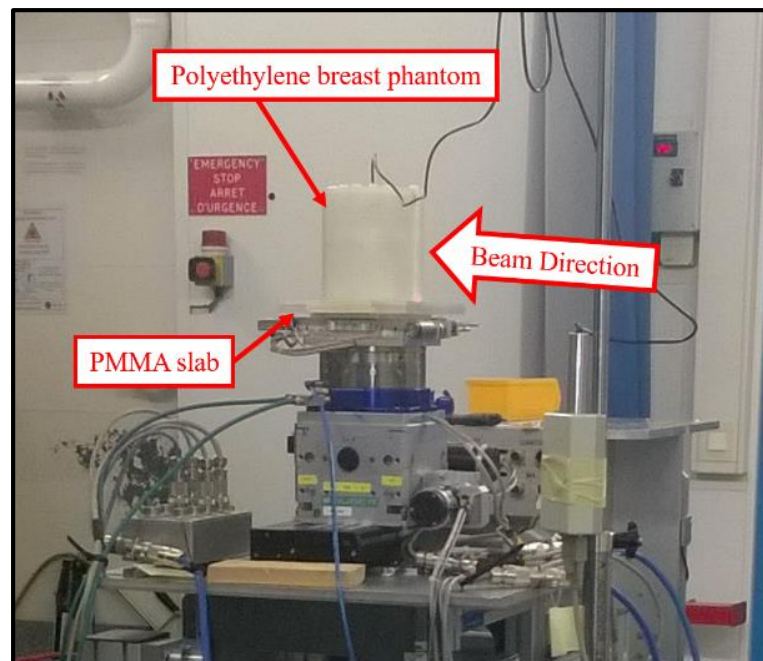
Figure 2.30: Experimental setup for radial dose profile measurement at ESRF, in this image the IC is positioned in the central hole of the phantom. The PE phantom was placed on a single PMMA slice of thickness 1 cm.

2.6.2 Radial Profile in a cylindrical phantom

The protocol employed for the measurements of the radial dose profile was the same used at AS (section 2.5.1.2). The experimental setup is shown in Figure 2.30. The air kerma was measured with the pencil ionization chamber (mod. 20x6-3CT, Radcal Corp., Monrovia, CA, USA). In contrast to experiment at AS, the PE phantom was placed on a single 1-cm thick slice of PMMA. Measurements were carried out at energy of 80 keV, 100 keV, 120 keV, and 175 keV. The X-ray beam was collimated to 6 mm vertically and to 1.5, 4, 7, or 15 cm horizontally. The same geometry of irradiation was reproduced with the MC code (section 2.4). Also in this case, the dose evaluation via MC simulation was obtained by scoring the deposited energy along 10 cm in the direction of the cylinder axes to reproduce the energy integration of the pencil chamber. The radial dose profiles are shown in Figure 2.31 and Figure 2.32. The dose profile are reported as percentage of the central dose. A dose profile peaked at the center of rotation was observed for the collimated beam at each energy. In the case of the 15-cm beam width, MC simulations and mesurements show two different behaviors for the dose distribution: a cupped profile resulted from the simulations and a domed profile from the experimental data. Moreover, the mean percentage differences in the dose distribution between experimental values and simulations was estimated in the range 4–15% with a significant difference in the cases of 1.5-cm and 15-cm collimated beams (Table 2.6). This discrepancy between measurements and simulations is probably due to a misalignment of the PE phantom with respect to the X-ray beam. Indeed, a different normalization is obtained when the centre of rotation is not on the cylinder axes. In addition, for 15-cm collimated beam, since the beam is 1 cm wider than the phantom in the horizontal direction, the X-ray beam might not irradiate the entire phantom and therefore the ionization chamber might measure a lower dose when placed at the peripheral position. Finally, a last contribution to the discrepancy could be due to the beam profile which was supposed uniform in the simulation, whilst an asymmetric profile was observed in the real case. However, an asymmetric beam profile was also observed at 100 keV at AS without any strong influence on the experimental dose distribution which was comparable with that obtained via simulations.
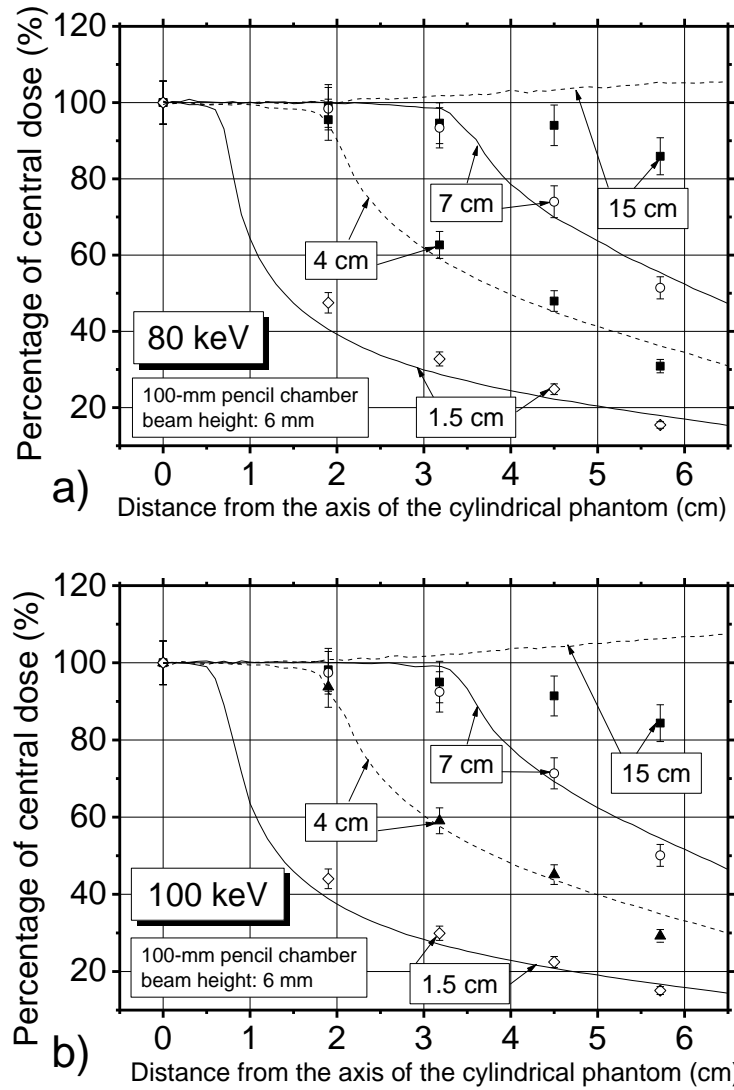
Figure 2.31: Comparison between the measured (symbols) and simulated (lines) relative air kerma in a 14-cm diameter polyethylene cylindrical phantom for beam width of 1.5, 4, 7 and 14 cm at 80 keV (a) and 100 keV (b). For the MC simulation, the dose distribution was evaluated by integrating the dose along 100 mm in the direction of the cylinder axis.
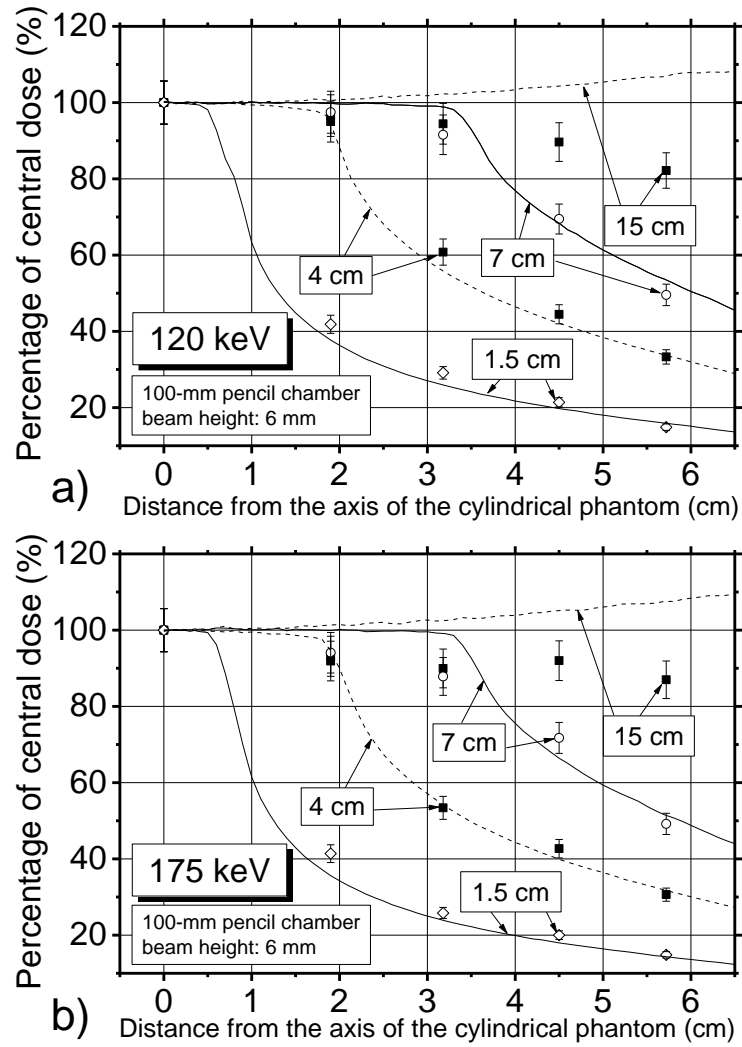
Figure 2.32: Comparison between the measured (symbols) and simulated (lines) relative air kerma in a 14-cm diameter polyethylene cylindrical phantom for beam width of 1.5, 4, 7 and 14 cm at 120, and 175 keV. For the MC simulation, the dose distribution was evaluated by integrating the dose along 100 mm in the direction of the cylinder axis.

Table 2.6: Mean percentage difference in the dose distribution between measurements and MC simulations evaluated for beam collimations of 1.5, 4, 7, and15 cm at 80, 100, 120, and 175 keV.

Collimation of X-ray beam	Mean Percentage Difference (%)			
(cm)	80 keV	100 keV	120 keV	175 keV
15	10 ± 9	12 ± 12	4 ± 2	15 ± 6
7	5 ± 3	5 ± 3	5 ± 3	7 ± 3
4	8 ± 7	7 ± 8	4 ± 3	4 ± 3
1.5	13 ± 3	10 ± 2	9 ± 2	8 ± 5

106

2.6.3 Assessment of the periphery-to-centre dose ratio with TLD

Measurements of the periphery-to-centre dose ratio in a PMMA phantom were carried out at 100 keV for beam collimation of 1.5 and 15 cm by using TLD-100. The TLD response was calibrated in terms of air kerma free-in-air in the range 0.5–1.5 Gy at 100 keV following the irradiation protocol used at AS (section 2.5.1.3). Figure 2.33 shows the calibration curve, for which a linear fit was used. As for the measurements at AS, a 14-cm diameter PMMA phantom with two cavities for the dosimeters positioning was employed. The beam height was set at 5 mm. Five TLD chips were irradiated at each position and the average of their response was used to calculate the dose ratio. The irradiation was also simulated with MC code. The results obtained with measurements and MC simulations for beam collimations of 1.5 cm and 15 cm are reported in Table 2.7. We calculated a dose ratio of 122% ± 15% for a collimation of 15 cm by using the measurements from TLD chips, comparable with the ratio obtained from simulations within the experimental error. However, the dose ratio measured for a beam collimation of 1.5 cm was not comparable with that from simulations. It is quite likely that also in this case the phantom positioning was crucial.
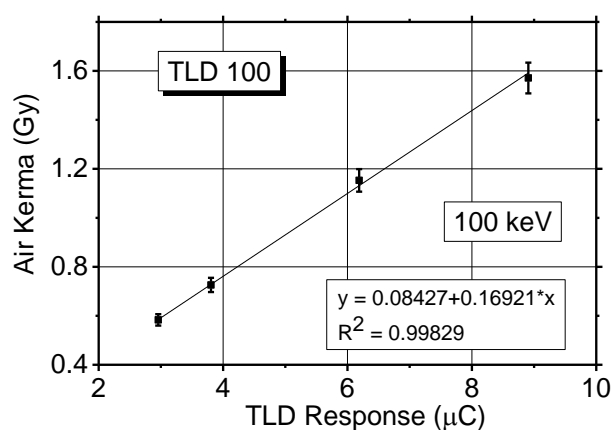
Figure 2.33: Calibration curve for the response of TLD dosimeters at 100 keV. The continuous line is a linear fit to the data points.

Table 2.7: Periphery-to-centre dose ratio simulated with MC code and measured with TLD100 for a SR beam collimated at 1.5 cm and 15 cm along the horizontal direction at 100 keV.

Collimation of X-ray beam (cm)	Periphery-to-centre dose ratio (%)	
	Measurement	MC simulation
15	122 ± 15	126 ± 2
1.5	35 ± 5	17 ± 0.3

2.6.4 Dose Painting

Dose painting technique reported in section 2.5.1.4 was employed to obtain three irradiation spots ("tumour foci") and a linear dose distribution at 100 keV. The dose distributions were imaged with radiochromic film EBT3 of size 12 cm $\times$ 5 cm (H $\times$ V) placed at mid-plane of a 14-cm diameter PMMA cylinder phantom. The radiochromic film were calibrated in terms of air kerma in PMMA following the calibration protocol reported in section 2.5.1. The scanner EPSON V750 PRO was used to scan the film in RGB mode (48 bit, TIFF image, 72 dpi). The cross-section of SR beam was 1.0 cm $\times$ 0.5 cm (H $\times$ V). Dose distributions were acquired with multiple rotations at a constant speed of 4°/s changing the position of the axis of rotation at each rotation. In particular, the axis was shifted by 1.5 cm at each rotation for the three foci irradiation, while the shift was 0.5 cm at each rotation in order to obtain a "line dose distribution". Figure 2.34 and Figure 2.35 show the dose distribution measured with the radiochromic film. The three foci irradiation (Figure 2.34a) obtained with three rotations – one rotation per focus – results in three target doses of about 400 mGy. In fact, the central focus produced during the first rotation shows a flat dose distribution of about 430 mGy, whilst the line profile (Figure 2.34b) reveals that in the two lateral foci the dose decreases increasing the distance from the central focus. This effect is a consequence of the overlap of the three dose distributions. In order to acquire a line dose distribution (Figure 2.35a), five dose target were irradiated by shifting the axis of rotation 0.5 cm at each rotation. The line profile resulted in a wide-peak distribution with a maximum of about 950 mGy and FWHM of 3 cm (Figure 2.35b).
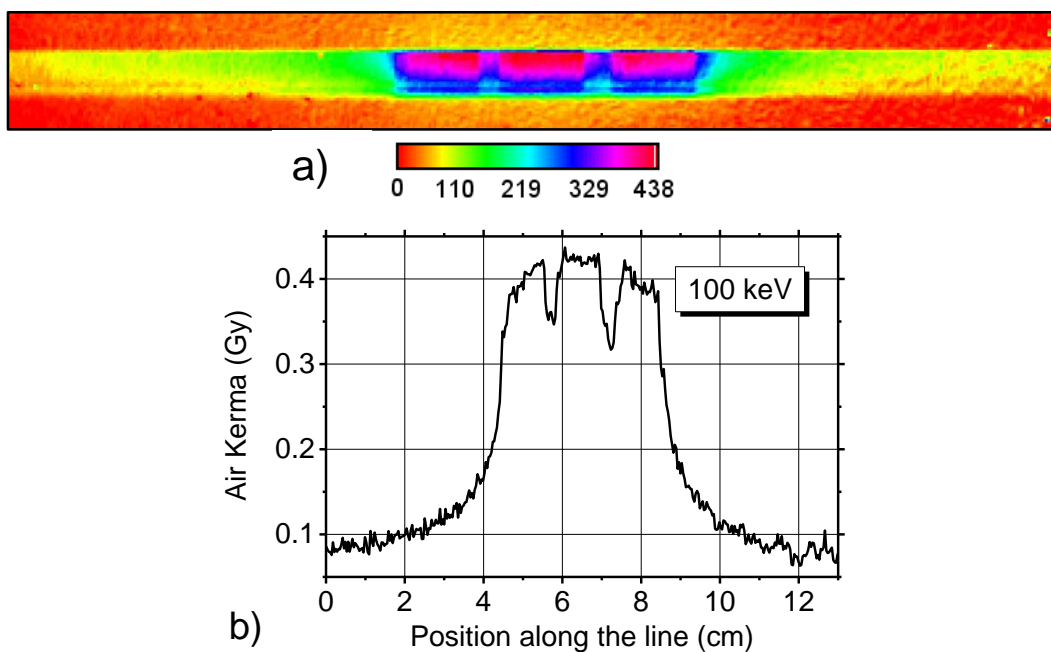
Figure 2.34: 2D dose distributions evaluated with radiochromic film EBT3 in a 14-cm diameter PMMA phantom at 100 keV. and b) corresponding line dose profile. The intended dose distribution (three foci) was obtained with three rotations by shifting the centre of rotation 1.5 cm.
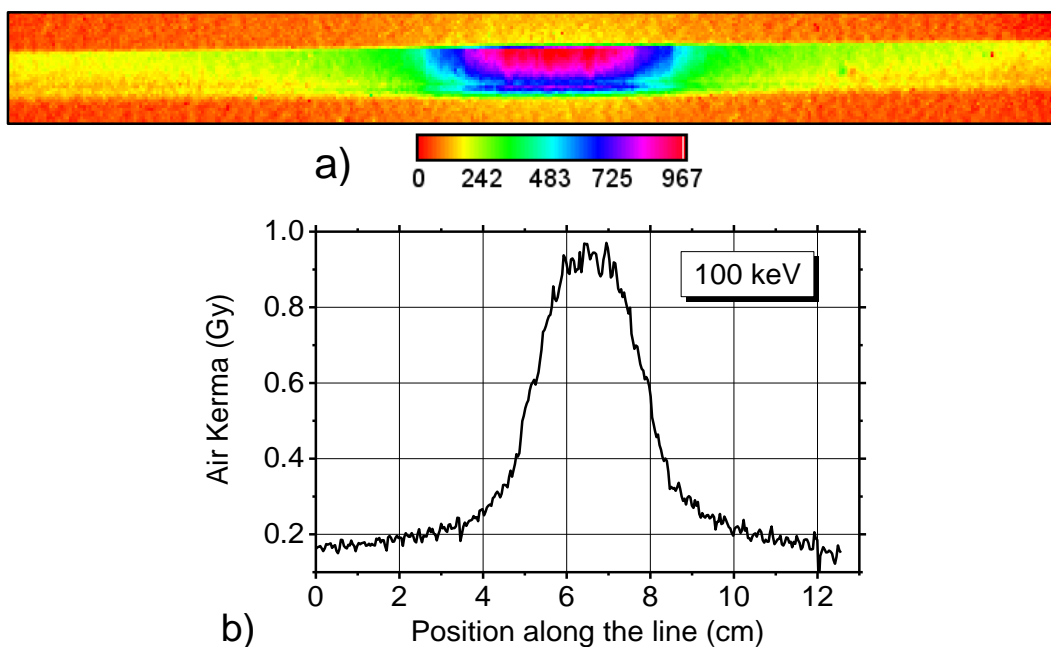
Figure 2.35: 2D dose distributions evaluated with radiochromic film EBT3 in a 14-cm diameter PMMA phantom at 100 keV. and b) corresponding line dose profile. The intended dose distribution (line distribution) was obtained with five rotations by shifting the centre of rotation 0.5 cm.

2.7 Ongoing work: Preliminary results of the use of dose-enhancement agent

The use of the contrast-enhancement agents for synchrotron radiation radiotherapy was studied with experiment in vitro (Estève et al, 2002, Corde *et al*., 2004, Bobyk *et al*, 2013) and in vivo (Adam *et al,* 2003, Adam *et al*, 2005, Adam *et al*, 2006, Obeid *et al*, 2014, Balosso *et al*, 2014, Bräuer-Krish *et al*, 2015). Measurements of dose enhancement factor with dosimeter are difficult because the dose-enhancement agent should be injected in the active volume of the dosimeter. However, techniques based on unlaminated radiochromic film (Morris *et al*, 2006, Rakowski *et al*, 2015) as well as 3D gel (Boudou *et al*, 2007, Rahman *et al*, 2012) were proposed in the literature.

We carried out a preliminary study on the use of iodinated solutions and gold nanoparticles for SR^3T by measuring the air kerma in the solutions with radiochromic film EBT3 as well as the X-ray transmission from radiographic images at 60, 80, and 100 keV at IMBL of AS. The measurements with radiochromic film is based on the idea that the increased X-ray absorption in the solution in which the radiochromic films were immersed determines the decrease of the air kerma at the surface of the dosimeter. A 10-cm diameter PMMA phantom with a central cavity of diameter 2.5 cm was employed for measurements. The cavity was filled with 10 ml of iodinated solutions containing different amount of contrast agent (320 mg I/ml, 32 mg I/ml, 3.2 mg I/mg, 1 mg I/ml) or 10-ml stabilized suspensions in citrate buffer of gold nanoparticles with size 5, 20, or 100 nm (Sigma-Aldrich, Inv., Germany). The nanoparticles concentrations in the solutions were about 5.5×10^{13} particles/ml, 6.5×10^{11} particles/ml, 3.9×10^9 particles/ml for 5-nm, 20-nm, 100-nm diameter nanoparticles, respectively (http://www.sigmaaldrich.com/technical-documents/articles/materials-science/nanomaterials/gold-nanoparticles.html). The cross-section of SR beam was 16 cm × 2 cm (H × V).

Measurements with radiochromic film

In order to measure the air kerma in the solution, pieces of radiochromic film EBT3 (2.5 cm × 4 cm) were immersed in the medium in the phantom cavity with the longer

side parallel to the cylinder axis and were irradiated by the SR beam from a single angle. The phantom was translated through the beam along the vertical position with a constant speed of 5 mm/s at 60 keV, 2.5 mm/s at 80 keV, and 1 mm/s at 100 keV. The air kerma rate was 450 mGy/s, 181 mGy/s, and 69 mGy/s at 60, 80, and 100 keV, respectively. The radiochromic film were scanned in RGB scanning mode (72 dpi, 48-bit, TIFF image) by using a flat-bed scanner EPSON V700 PHOTO available at IMBL and calibrated in terms of air kerma free-in-air.

The comparison of the air kerma measured with the radiochromic film in air, water and in the solutions containing iodine or gold nanoparticles is shown in Figure 2.36. The figure shows average pixel value in the film image evaluated in a ROI of size 0.3 cm $\times$ 1.0 cm (see Figure 2.37) and corresponding measurement uncertainty. The air kerma measured in water is indicated with a horizontal dash line on the graph. The lowest air kerma was measured in the iodinated solution with 320 mg I/ml at each energy: 13%, 38%, and 54% of the air kerma evaluated in water at 60, 80, and 100 keV, respectively. The doses measured in solutions with gold nanoparticles were comparable to that estimated in water within the measurements uncertainty at 60 keV and 80 keV. This indicates that the concentration of gold nanoparticles in the solution is too low and that the solutions shows energy absorption similar to water. On the other hand, the air kerma in solutions of 20-nm diameter gold nanoparticle as well as 100-nm diameter gold nanoparticles is lower than air kerma evaluated in water at 100 keV. We note that the absorption K-edge of gold is at 80.734 keV (Figure 2.38), so that the result at 100-keV photon energy may take into account the photoelectric interaction with K-shell electrons, in addition to L-shell electrons as may occur with 60 keV and 80 keV photons.
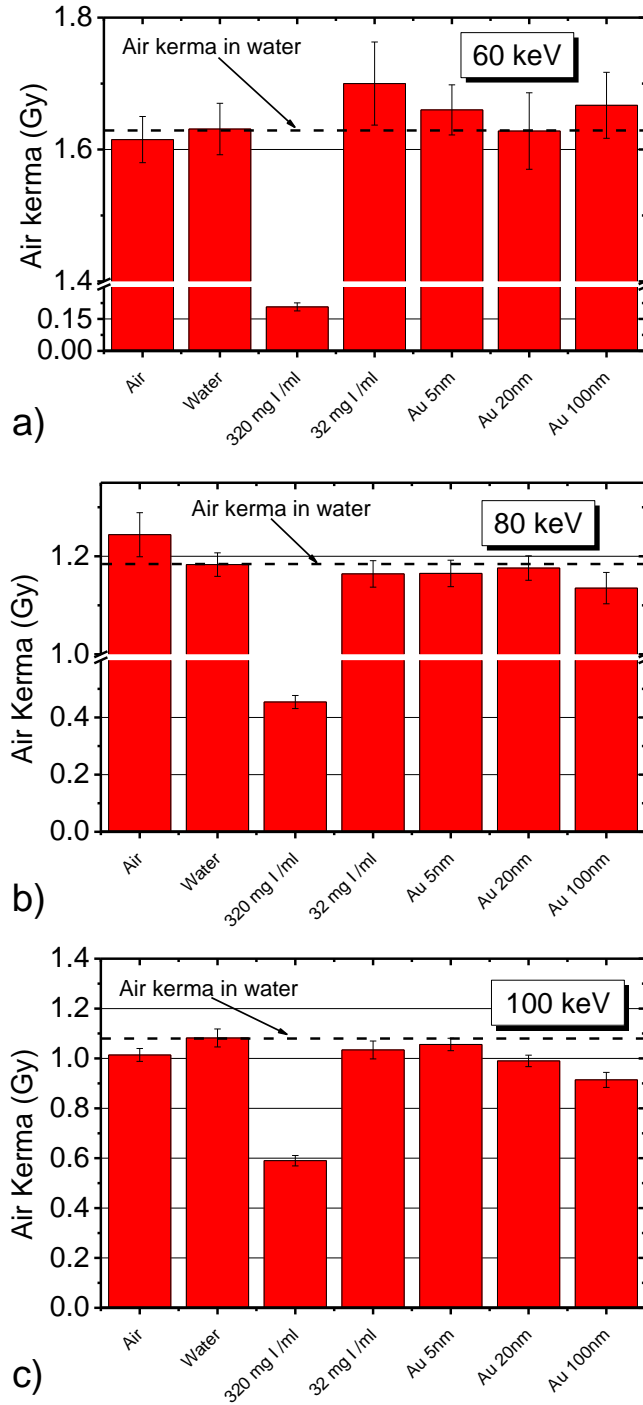
Figure 2.36: Comparison of the dose measured with radiochromic film EBT3 in air, water, iodinated solutions with different concentration of iodine (320 mg I/ml, 32 mg I/ml) and solutions of gold nanoparticle of different size (5nm, 20 nm, 100 nm). The comparison is reported at 60 keV (a), 80 keV (b) and 100 keV (c). The radiochromic film was calibrated in terms of air kerma free-in-air. The dose was estimated as the average pixel value in a ROI of size (0.3 cm × 1.0 cm) on the films. The horizontal dash line indicated the dose value measured when the film was immersed in water.

112
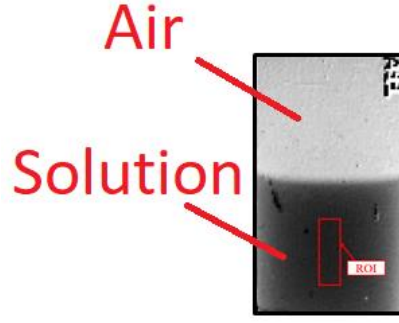
Figure 2.37: Dose map imaged with radiochromic film at 60 keV. The film was immersed in a iodinated solution with a concentration of 320 mg I/ ml. The ROI used for the dose evaluation is shown.
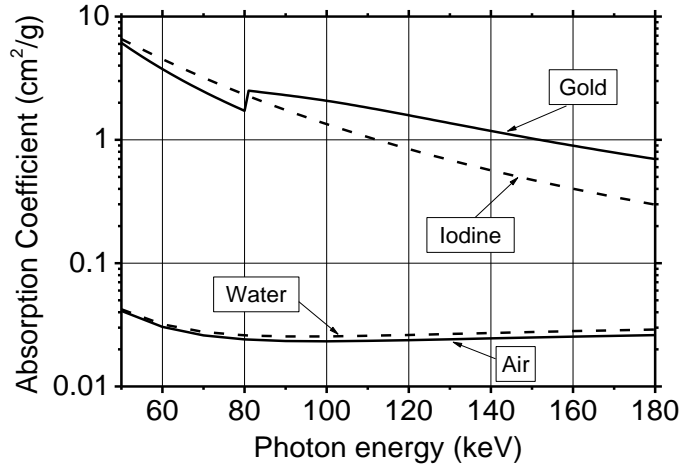
Figure 2.38: Absorption coefficient of air, water, iodine and gold as function of photon energy. The values were estimated with the XMuDat software (Nowotny, 1998).

Measurements with radiographic image

The measurements with radiographic image were based on estimation of X-ray transmission defined by the Lambert-Beer Law:

$$\frac{I}{I_0} = e^{-\mu x} \tag{2.1}$$

where I is the transmitted beam intensity and I_0 is the incident beam intensity. Radiographic images were acquired with a Hamamatsu C9252DK-14 flat panel detector featuring a 200 μm pitch and a 1-mm thick CsI:Tl scintillator. The detector was at 6 m from the sample. The X-ray transmission image was obtained by dividing the images acquired with phantom on the beamline by a flat field image (obtained without phantom). We assumed the linear response of the detector after dark field correction. Figure 2.39 shows the comparison of the X-ray transmission evaluated

113

for each medium filling the phantom cavity. In particular, the average and standard deviation of the pixel values in a ROI of size (0.3 cm × 1.0 cm) (Figure 2.40) was estimated. The iodinated solutions with high concentration of iodine (320 mg I/ml and 32 mg I/ml) yield a transmission signal lower than that from water at each energy. This is due to the greater X-ray attenuation coefficient of iodine with respect to water (Figure 2.41). We also observe that the solution with a higher concentration of iodine caused a greater attenuation of the X-ray beam resulting in a lower X-ray transmission. The X-ray transmission produced by the solutions with gold nanoparticles as well as that from iodinated solutions with a low concentration (3.2 mg I/ml and 1 mg I/ml) is comparable to that obtained for water at each energy indicating a too low concentration of dose-enhancement agents in the solutions.

a)

b)

114
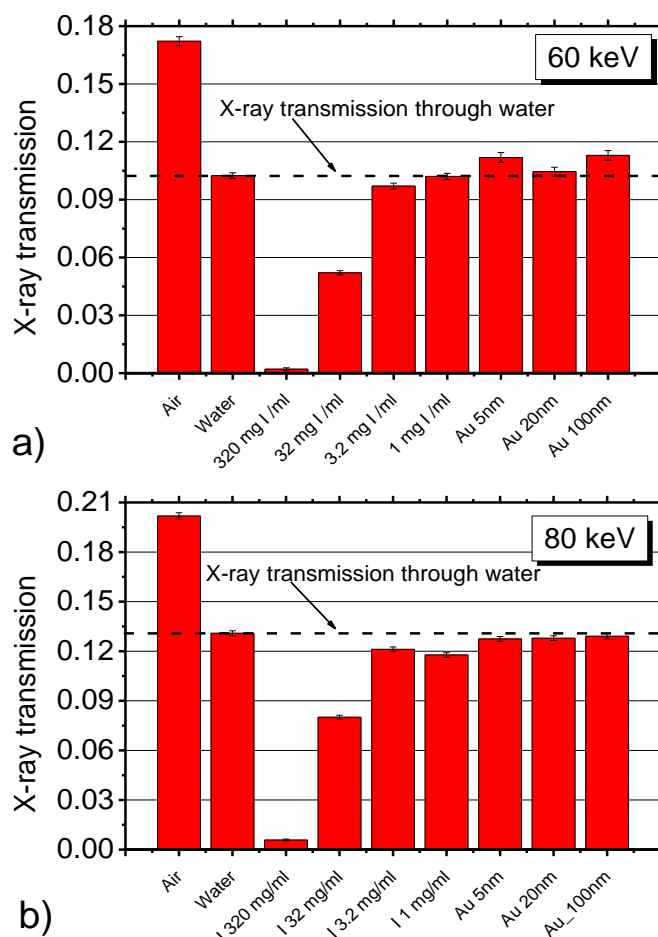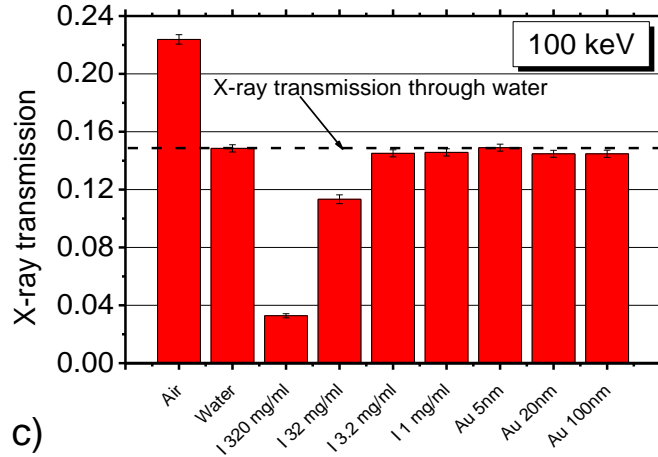
Figure 2.39: Comparison of the X-ray transmission acquired with Hamamatsu C9252DK-14 flat panel detector. The phantom cavity was filled with air, water, iodinated solutions with different concentration of iodine (320 mg I/ml, 32 mg I/ml, 3.2 mg I/ml, 1 mg I/ml) and solutions of gold nanoparticle of different size (5nm, 20 nm, 100 nm). The comparison is reported at 60 keV (a), 80 keV (b) and 100 keV (c). The X-ray transmission was estimated as the average of pixel values in a ROI of size (0.3 cm × 1.0 cm). The horizontal dash line indicates the transmission value measured when cavity was filled of water.
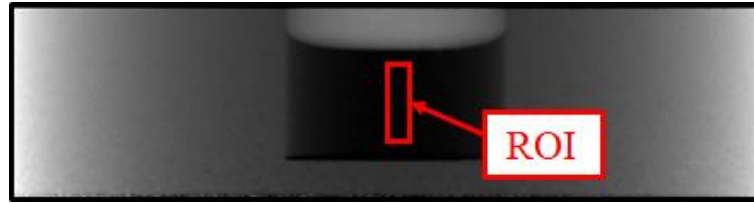
Figure 2.40: Crop of the 2D map of X-ray transmission at 60 keV with the cavity filled of iodinated solution with a concentration of 32 mg I/ ml. The ROI used for the transmission evaluation is shown.
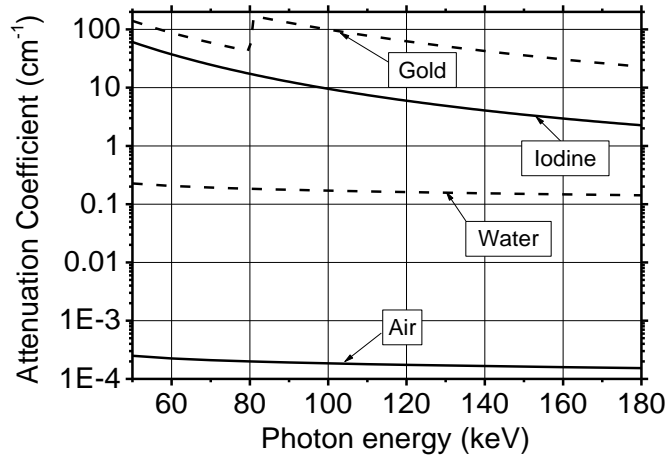
Figure 2.41: Attenuation coefficient of air, water, iodine and gold as function of photon energy. The values were estimated with the XMuDat software (Nowotny, 1998).

115

2.8 Discussion

In this part of the thesis work, we provided a proof-of-principle showing the feasibility of the external beam radiotherapy for breast cancer treatment with SR at low energy (60 keV – 120 keV) with measurements performed at AS, ESRF and MC simulation.

We showed that the shape of the dose distribution in a PE cylinder phantom depends on the SR beam collimation. The beam collimation in the direction perpendicular to the phantom axis produces a dose distribution peaked at the centre of rotation. In particular, we showed that it is possible to obtain a focus of dose in the centre of rotation with a dose to the skin of about 14% of the target dose at 60 keV, for a beam collimation of 1.5 cm and the centre of rotation, corresponding to the tumour position, on the cylinder axis. The periphery-to-dose ratio was 12.5% at 80 keV and 11 % and 100 keV. These values are comparable to that of 10 % obtained via MC simulation at 175 keV, in the same irradiation conditions. This last energy produces the same depth-dose distribution of an orthovoltage X-ray tube operating at 300 kVp (De Lucia, 2015). For comparison, *Prionas et al, 2012* reported a dose to the skin <7% of the maximal dose for 320 kVp X-ray beam collimated at 1 cm, while Breitkreutx *et al.* (2017) in the feasibility study of KVAT at 200 kV reported lesion-to-skin ratio of 2.3 and 3.3 for lesion of 4 and 3 cm, respectively. In terms of tumour-to-skin dose ratio, for a target "tumour" in the centre of the phantom, the tumour-to-skin dose ratio was evaluated between 7.4 at 60 and 9.5 at 175 keV, respectively (this ratio is about 7 for 6-MV clinical beams, see Podgorsak, 2005).

In the study performed at 60 keV at AS, periphery-to-centre dose ratio measured with TLDs at 4 cm from the cylinder axis [(24 ± 3)%] was comparable with that obtained via MC simulation. A similar agreement was observed for the same mesurements performed at ESRF at 100 keV for 15-cm collimated beam. On the other hand, a discrepancy of 50% between simulated and experimental data from ESRF was evaluated for a 1.5-cm width beam.

The measurements performed with SR beam at ESRF and with the orthovoltage X-ray tube in the Dept. of Physics of Università di Napoli Federico II highlighted

that the accuracy of the beam collimation and the alignment of the sample with respect to X-ray beam are critical issue for SR³T.

The dose painting feasibility was demonstrated with both MC simulations and measurements with radiochromic films in a 14-cm PMMA cylinder phantom. Non-uniform dose distributions can be obtained by using multiple rotations, by shifting the centre of rotation and changing the rotation speed. In particular, we reproduced two off-centre foci and line dose distribution at 60 as well as 100 keV and a three off-centre foci at 100 keV. Different dose profiles were observed inside the foci depending on their position along the diameter and the overlap of the tails of dose distributions produced at each rotation. For dose painting, the comparison between simulated data and experimental data acquired with radiochromic film showed a systematic overestimation of simulated data with respect to the measurements at 60 keV. This disagreement suggests the need to improve the study of EBT3 response to X-ray beam at low energy in the irradiation condition used for SR³T. Albeit we demonstrated the proof of principle of dose painting, the constraints stressed by Prionas *et al* (2012) – beam collimation accuracy, lesion proximity to the skin surface and chest wall, total treatment time – are still present.

We also examined the use of low energy photon beams with a dose-enhancement agent. The availability of a monoenergetic X-ray beam with high dose rate combined with the use of possible dose-enhancement agents or contrast agents (e.g. iodinated solution or gold nanoparticles) would permit to optimize the breast irradiation by selecting the best SR beam energy. In particular, the use of low photon energy (e.g. 120 keV or lower, with respect to MV photon energy of conventional radiotherapy) could increase the photoelectric absorption and hence increase the dose deposit in the region of accumulation of the radiosensitizer. In particular, the use of an iodinated medium (commonly adopted for contrast enhanced mammography) whose in vivo biochemical kinetics is well investigated, could be an advantageous addition to the technique, for dose enhanced SR³T (DE-SR³T technique). In order to investigate the use of the dose-enhancement agents (iodine and gold nanoparticles), we employed a technique based on the measurement of air kerma in the solution containing the radiosensitizer with radiochromic film EBT3 and another technique based on the evaluation of the X-ray transmission through the solution from radiographic images.

Both these technique do not permit to evaluate the dose-enhancement effect directly. However, effect of the use of different materials on the dose or on the X-ray transmission can be estimated.

We note that the available air kerma rate free-in-air (e.g. 2.22 Gy/min at 60 keV at AS) can be comparable with the one adopted in conventional radiotherapy with MV X-ray beams (about 0.5 Gy/min) (Prionas et al, 2012) by using an appropriate beam filtration. As regards a future SR^{3}T treatment session, taking as reference a 1-min rotation time, the necessity of multiple rotations/translations of the patient bed for covering the tumor volume with the available beam size might require a scan time in the range of e.g. 10 min. This would be higher than the typical irradiation time for the single fraction of conventional breast radiotherapy. During the scan the breast should be immobilized in a suitable holder. With a dose rate of about 2 Gy/min, a therapy session may deliver a tumor dose in the order of 2 Gy, as in a single fraction of fractionated conventional plan (25 fractions). However, we noted that a significantly higher dose rate is available for SR^{3}T at SR sources, which would permit hypo-fractionated treatment plans with the same irradiation times.

In addition, image guided SR^{3}T (with or without contrast enhancement) can be performed, permitting real-time computed tomography imaging with additional delivery of glandular doses in the order of few mGy (Mettivier et al, 2016). Moreover, the use of a radio-sensitizer can also improve the performance of the imaging. Prionas et al (2010) reported the results of the first clinical trial of contrast-enhanced BCT showing an improvement of the conspicuity of malignant breast lesion with respect unenhanced breast CT and a visibility of malignant calcification similar to mammography. They also calculated the lesion enhancement "as the difference between lesion intensity normalized to the adipose tissue intensity in pre-contrast and post-contrast images" Prionas et al (2010) estimating an enhancement of 55.9 HU ± 4.0 and 59. HU ± 2.8 for malignant lesions and ductal carcinoma in situ, respectively. They also evaluated the benign lesions enhanced 17.6 HU ± 6.1 Prionas et al (2010).

Potential application of SR^{3}T technique are limited fractions rotational radiotherapy, radiotherapy boost and small lesion irradiation. Sites potentially

suitable for SR³T are the AS in Melbourne, Australia, ESRF in Grenoble, France, and CLS in Saskatoon, Canada.

The work reported in this thesis represents the starting point of the study on this new radiotherapy technique and shows its potential with dosimetric studies. In the next future, radiobiological studies will be performed in order to compare the radiobiological response of the breast cells to the SR³T irradiation to that obtained with a conventional radiotherapy irradiation.

We foresee several possible implementations of the technique in order to resolve some critical issues showed in this work. A possible reduction of the number of rotations or translations for the treatment of large lesion could be obtained with spiral scan, or rotational scan over 180°, or a curved scan trajectory. We expected a spiral trajectory in a rotational scan around the tumour produces less dose to the skin than compared to circular orbit scan, as recently investigating by M. Donzelli at ESRF (Bräuer-Krisch, 2016). In addition, we have observed that in the case of multiple-foci irradiations the use of a beam with a constant intensity during the rotational irradiation produces target doses with an uneven distribution. We suggest that an intensity modulation of the X-ray beam during the rotation could overcome this issue. The modulation could be obtained by using a combination of attenuators (e.g. PMMA attenuator) moving through the beam. The shape of attenuators can be studied in combination with its movement to obtain the desired intensity modulation during the treatment. The proposed technique is similar to that used in proton therapy for energy-modulation of the beam (Cirrone *et al*, 2004).

Finally, we remind that the SR source also provides a polychromatic X-ray beam with high photon flux (pink or white beam), which is used for study of microbeam radiotherapy. These polyenergetic sources could be adopted for breast SR³T as well. We forsee an interesting application of the microbeam radiotherapy (MRT) to the breast in combination with the rotational or spiral irradiation of SR³T. A proposal together with scientist at CLS in Canada has been submitted recently by the medical physics group in Napoli to study this last application.

Conclusions

Breast imaging techniques employing X-rays have undergone fundamental changes in the last two decades, with the introduction of 3D imaging techniques like DBT and cone-beam breast CT. SR research on breast imaging may play an important role in investigating the limits and potential of new dedicated techniques for 2D and 3D breast imaging, by exploiting the energy tunability and high spatial coherence of SR beam. In particular, phase-contrast breast mammography with SR and phase-contrast breast tomography with SR are under investigation. A leading international activity is carried out at the SYRMEP beamline of ELETTRA synchrotron radiation facility. I was involved since the beginning of the breast CT project at ELETTRA, as reported in the first part of this thesis. We showed the feasibility of the technique, under strict dosimetric limits which require a total glandular dose during the CT scan, not higher than the mean glandular dose of conventional two-view mammography. In order to prepare a future clinical protocol for breast CT with SR, both beam dosimetry and phantom dosimetry issues must be assessed, together with quality assurance procedures. As result of my work, an assessment has been provided of the energy dependent response of dosimeters adopted in the SYRMA-CT project.

However, SR is an intense light source, whose dose rates are large enough to conceive its use for *radiotherapy* of breast cancer in addition to *imaging* of breast cancer. On the basis of the experience gained during my activity within SYRMA-CT project for breast CT, I performed a series of experiments at major SR centres (ESRF in Europe and AS in Australia) which represent the first experimental validation of the feasibility of a new radiotherapy technique for breast cancer. This technique is based on the rotation of the patient support table and a pendant breast, so that the fixed laminar SR beam irradiates the tumour in a circular orbit (or in a spiral orbit). The principle for this new SR^{3}T technique relies on the spatial summation of the absorbed dose at kilovoltage energies along the axis of rotation passing through the tumour site. The very exciting possibility of introducing such a new experimental technique for breast cancer radiotherapy can now be founded on the very large dataset of measurements with breast phantoms reported in the second part of this thesis. In particular, the use of energy photons (in the range 60–120 keV) for breast

radiotherapy might open the way for higher photoelectric absorption and increased dose-enhancement factor when using radiosensitizing agents (e.g. gold nanoparticles) as under investigation for conventional radiotherapy. Moreover, due to the presence of an intense transmitted X-ray beam during a SR^3T treatment, image-guided SR^3T might be implemented, so as to localise during the treatment the irradiation target. Finally, the use an iodinated contrast agent can be envisaged as well for enhanced tumour contrast.

The research work exposed in this thesis is still ongoing, with new, exciting, scientifically stimulating observations to be expected in the next years.

Final remarks

The work presented in this thesis demonstrated, for the first time, the possibility to employ the same setup based on SR to perform diagnostic breast computed tomography as well as image-guided breast rotational radiotherapy, by suitably tuning the energy, the shape and the intensity of the SR beam. In this setup, the patient lies prone on a translating/rotating bed with a hole for the pending uncompressed breast and the SR beam irradiates the organ during a complete or partial rotation of the bed. The use of the low energy beam (between 30 and 40 keV) with low dose rate (in the order of a few mGy/min) permits to perform diagnostic CT breast imaging, while radiotherapy applications can be investigated by using a high energy SR beam (60–120 keV) with high dose rate (several Gy/min).

In the first part of this thesis, we have demonstrated how the high spatial coherence of the SR beam together with the use of a high-efficiency single-photon counting detector provided optimal conditions to perform phase-contrast breast CT. PhC-BCT imaging of a breast mastectomy specimen produced high-contrast and high-resolution maps of the tissue structures after retrieving the phase-map. We have also demonstrated that the use of the conventional clinical dose metric, MGD, can be not adeguate in the case of partial breast irradiation planned in the SYRMA-CT/3D project and can produce an underestimate of the risk from radiation. We introduced new dose metrics, MGD_V and MGD_T, which take into account the partial irradiation geometry. MGD_V provides an estimate of the mean glandular dose in the irradiated tissue slice evaluated as the ratio of energy released in the irradiated slice by the glandular mass which was directely irradiated with X-ray beam, m_g, , while MGD_T is defined as the ratio of the energy released in the whole breast, and the masss m_g. A complete characterization of TLD and radiochromic film dosimeters which will be used for phantom and beam dosimetry was also carried out in this thesis. Finally, we have assessed for the SYRMA-CT/3D setup a spatial resolution higher than that of cone-beam BCT systems present in the literature.

In the second part of the thesis, we have demonstrated that the BCT setup can be used for radiotherapy application by changing the energy and the dose rate of the SR beam. We have showed the feasibility of the rotational breast radiotherapy with

SR at energies in the range 60–120 keV with MC simulations and experiments on phantoms. The use of low photon energy would provide a higher dose-enhancement when a radiosensitizing (e.g. gold nanoparticles) is used for breast radiotherapy. This new technique could be promising for the treatment of the small lesion and hypo-fractionated radiotherapy, with a skin-to-lesion dose ratio comparable to that of conventional radiotherapy for lesion at the centre of the breast. The use of the same platform developed for BCT also permits to perform radiotherapy in the same geometry as for the diagnostic imaging. This could also reduce the issues due to the patient repositioning during fractionated radiotherapy. In addition, the use of an imaging detector during the treatment would permit to perform an image-guided radiotherapy.

Acknowledgments

References

AAPM 2010 Report of AAPM Task Group 111: The future of CT dosimetry: comprehensive methodology for the evaluation of radiation dose in x-ray computed tomography *AAPM Report No 111* (City Park, MD: American Association of Physicist in Medicine).

Abrami, A., Arfelli, F., Barroso, R.C., Bergamaschi, A., Billè, F., Bregant, P., Brizzi, F., Casarin, K., Castelli, E., Chenda, V., Della Palma, L., Dreossi, D., Fava, C., Longo, R., Mancini, L., Menk, R.H., Montanari, F., olivo, A., Pani, S., Pillon, A., Quai, E., Ren Kaiser, S., Rigon, L., Rokvic, T., Tonutti, M., Tromba, G., Vascotto, A., Venanzi, C., Zanconati, F., Zanetti, A., Zanini, F. (2005) Medical applications of synchrotron radiation at the SYRMEP beamline of ELETTRA. *Nucl. Instrum. Methods A* **548**, 221–227.

Abramoff, M.D., Magelhaes, P.J., &Ram, S.J. (2004) Image processing with Imagej. *Biophotonics Int.* **11**, 36–42.

Adam. J.F., Elleaume, H., Jouber, A., Biston, M.C., Charvet A.M., Balosso, J., Le Bas, J.F., Estève, F. (2003) Synchrotron radiation therapy of malignant brain glioma loaded with an iodinated contrast agent: First trial on rats bearing F98 gliomas. *Int. J. Radiation Onc. Biol. Phys.* **57**(5), 1413–1426.

Adam, J.F., Biston, M.C., Joubert, A., Charvet, A.M., Le Bas, J.F., Estève, F., Elleaume, H. (2005) Enhanced delivery of iodine for synchrotron stereotactic radiotherapy by means of intracarotid injection and blood-brain barrier disruption: Quantitative iodine biodistribution studies and associated dosimetry. *Int. J. Radiation Onc. Biol. Phys.* **61**(4), 1173–1182.

Adam, J.F., Joubert, A., Biston, M.C., Charvet A.M., Peoc'h M., Le Bas J.F., Balosso, J., Estève, F., Elleaume, H. (2006) Prolonged survival of fischer rats bearing F98 glioma after iodine-enhanced synchrotron stereotactic radiotherapy. *Int. J. Radiation Onc. Biol. Phys.* **64**(2), 603–611.

Agostinelli et al. (2003) Genat4-a simulation toolkit. *Nucl. Instrum. Methods A* **506**, 205–303.

Ando, M., Bando, H., Endo, T., Ichihara, S., Hashimot, E., Hyodo, K., Kunisada, T., Li, G., Maksimenko, A., Mori, K., Shimao, D., Sugiyama, H., Yuasa, T., Ueno, E. (2008) Refraction-based 2D, 2.5D and 3D medical imaging: Stepping forward to a clinical trial. *European J. Radiology* **68**(3), S32–S36.

Auweter, S.D., Herzen, J., Willner, M., Grandl, S., Scherer, K., Bamberg, F., Reiser, M.F., Pfeiffer, F., Hellerhoff, K. (2014) X-ray phase-contrast imaging of the breast—advances towards clinical implementation. *Br. J. Radiol.* **87**, 1–8.

Bacci, C., D'Angelo, L., Furetta, C., Giancola, S. (1993) Comprehensive study on LiF:Cu, Mg, P (GR-200A) *Radiat. Prot. Dosim.* **47**, 215–218.

Bakshi, A.K., Chatterjee, S., Palani Selvam, T., Dhabekar, B.S. (2010) Study on the response of thermoluminescent dosimeters to synchrotron radiation:

experimental method and Monte Carlo calculations. *Radiat. Prot. Dosim.* **140**, 137–146.

Balosso, J., Estève, F., Elleaume, H., Bravin, A., Adam, J.F., Renier, M., Nemoz, C., Brochard, T., Berkvens, P., Le Bas J.F. (2014) Monoenergetic synchrotron beams: first human experience for therapeutic purpose. *Radiotherapy and Oncology* **11**, S81–S82.

Baran, P., Pacile, S., Nesterests, Y.I., Mayo, S.C., Dullin, C., Dreossi, D., Arfelli, F., Thompson, D., Lockie, D., McCormack, M., Taba, S.T., Brun, F., Pinamonti, M., Nickson, C., Hall, C., Dimmock, M., Zanconati, F., Cholewa, M., Quiney, H., Brennan, P.C., Tromba, G., Gureyev, T.E. (2017) Optimization of propagation-based x-ray phase-contrast tomography for breast cancer imaging. *Phys. Med. Biol.* **62**(6), 2315–2332.

Bellazzini, R., Spandre, G., Brez, A., Minuti, M., Pinchera, M., Mozzo, P. (2013) Chromatic x-ray imaging with a fine pitch CdTe sensor coupled to a large area photon counting pixel ASIC. *J. Instrum.* **8**, C02028.

BCSC (2009) – website: http://www.bcsc-research.org/statistics/benchmarks/screening/2009/tableSensSpec.html

Bobyk, L., Eouard, M., Deman, P., Vautrin, M., Pernet-Gallery, K., Deletoche, J., Adam, J.F., Estève, F., Ravant, J.L., Elleaume, H. (2013) Photoactivation of gold nanoparticles for glioma treatment. *Nanomedicine: NBM* **9**(7), 1089–1097.

Boone, J.M., Nelson, T.R, Lindfors, K.K., Seibert, J.A. (2001a) Dedicated breast CT: radiation dose and image quality evaluation. *Radiology* **221**, 657–67.

Boone, J.M. (2001b) Determination of the presampled MTF in computed tomography. *Med. Phys.* **28**, 356–60.

Boone, J. M. (2002) Normalized glandular dose (DgN) coefficients for arbitrary x-ray spectra in mammography: computer-fit values of Monte Carlo derived data. *Med. Phys.* **29**, 869–875.

Boone J.M., Shah N., Nelson T.R. (2004). A comprehensive analysis of DgN(CT) coefficients for pendant-geometry cone-beam breast computed tomography. *Med Phys* **31,** 226–235.

Boone, J.M., Kwan, A.L.C., Seibert, J.A., Sha, N., Lindfors, K.K. (2005) Technique factors and their relationship to radiation dose in pendant geometry breast CT *Med. Phys.* **32,** 3767–76.

Boone, J. M., Prionas, N., Burkett, G. W., Packard, N. J., & Yang, K. (2009) TU-E-303A-03: Breast CT as a Platform for Image Guided Therapies of Breast Cancer. *Med. Phys.* **36**(6), 2747–2747.

Bos, A.J.J. (2001) High sensitivity thermoluminescence dosimetry. *Nucl. Instr. Methods B* **184**, 3–28.

Boudou, C., Tropres, I., Rousseau, L., Amalle, L., Adam, J.F., Estève, F., Elleaume, H. (2007) Polymer gel dosimetry for synchrotron stereotactic radiotherapy and iodine dose-enhancement measurement. *Phys. Med. Biol.* **52**, 4881–4892.

Bovi. M., Laitano, R.F., Pimpinella, M., Toni, M.P., Casarin, K., Quai, E:, Tromba, G, Vascotto, A., & Dressi, D. (2007) Absolute air-kerma measurement in a synchrotron light beam by ionization free-air chamber. Presented at the workshop on Absorbed Dose and Air Kerma Primary Standards, Paris, France, 9–11 May 2007.

Bräuer-Krish, E., Adam, J.F., Alagoz, E., Bartzch, S., Crosbie, J, & DeWagter, C. (2015). Medical physics aspects of the synchrotron radiation therapies: Microbeam radiation therapy (MRT) and synchrotron stereotactic radiotherapy (SSRT). Phys. Med. **31**(6), 568–583.

Bräuer-Krish, E. (2016) Microbeam Radiation Therapy (MRT): achievements and future perspectives. Presented at International Conference on Translational Research in Radio-Oncology | Physics for Health in Europe, Geneve, Switzerland, 15–19 February 2016.

Bravin, A., Coan, P., Suortti, P. (2013) X-ray phase-contrast imaging: from pre-clinical applications towards clinics. *Phys. Med. Biol.* **58**,R1–R35.

Bravin, A., Olko, P., Schültke, E., & Wilkens, J.J. (2015) SYRA3 COST action–microbeam radiation therapy: roots and prospects. *Phys. Medica* **31**, 561–563.

Breitkreutz, D.Y., Weil, M.D., Zavgorodni, S., Bazalova-Carter, M. (2017) Monte Carlo simulations of a kilovoltage external beam radiotherapy system on phantoms and breast patients. *Med. Phys.,* DOI:10.1002/mp.12619

Brown, T.A.D., Hogstrom, K.R., Alvarez, D., Mathews, K.L., Ham, K. & Dugas, J.P. (2012) Dose-response curve of EBT, EBT2, and EBT3 radiochromic films to synchrotron-produced monochromatic x-ray beams. *Med. Phys.* **39**(12), 7412–7417.

Cai, W., Ning, R. (2009) Dose efficiency consideration for volume-of-interest breast imaging using X-ray differential phase-contrast CT. Proc SPIE 2009;7258. *Med. Imag.: Physics of Medical Imaging,* 72584D.

Camerani, M.C., Golosio, B., Somogyi, A., Simionovici, A.S., Steenari, B.M., Panas, E. (2004) X-ray fluorescence tomography of individual municipal solid waste and biomass fly ash particles. *Anal. Chem.* **76**, 1568–95.

Castelli, E., Arfelli, F., Dreossi, D., Longo, R., Rokvic, T., Cova, M.A., Quaia, E., Tonutti, M., Zanconati, F., Abrami, A., Cheda, V., Menk, R.H., Quai, E., Tromba, G., Bregant, P., de Guarrini, F. (2007) Clinical mammography at the SYRMEP beam line. *Nucl. Instrum. Meth. A* **572**, 237–240.

Castelli, E., Tonutti, M., Arfelli, F., Longo, R., Quaia, E., Rigon, L., Sanabor, D., Zanconati, F., Dreossi, D., Abrami, A., Quai, E., Bregant, P., Casarin, K., Chenda, V., Menk, R.H., Rokvic, T., Vascotto, A., Tromba, G., Cova, M.A. (2011) Mammography with synchrotron radiation: first clinical experience with phasedetection technique. *Radiology* **250**, 684–94.

Cauzid, J., Philippot, P., Bleuet, P., Simionovici, A., Somogyi, A., Golosio, B. (2007) 3D imaging of vapour and liquid inclusions from the Mole Granite,

Australia, using helical fluorescence tomography. *Spectrochim. Acta* B **62**, 799–806.

Cirrone, G.A.P., Cuttone, G., Di Rosa, F., Nigro, S.L., Pia, M.G., Raffaele, L., Russo, G. (2004) Monte Carlo based implementation of an energy modulation system for proton therapy. *IEEE Nucl Sci Symp Conf Rec 2004* **4**, 2133–2137.

Coan, P., Bravin, A., Tromba, G. (2013) Phase-contrast x-ray imaging of the breast: recent developments towards clinics. *J. Phys. D: Appl. Phys* **46**, e494007.

Corde, S., Joubert, A., Adam, J.F., Charvet, A.M., Le Bas, J.F., Estève, F., Elleaume, H., Balosso, J. (2004) Synchrotron radiation-based experimental determination of the optimal energy for cell radiotoxicity enhancement following photoelectric effect on stable iodinated compounds. *Br. J. Cancer* **91**(3), 544–551.

Coone, A.B., Dickler, A., Kirk; M.C., Liao, Y., Shah, A.P., Strauss, J.B., Chen, S., Turian, J., Griem, K.L. (2010) Tomotherapy and multifield intensity-modulated radiotherapy planning reduce cardiac doses in left-sided breast cancer patients with unforable cardiac anatomy. *Int. J. Radiation Oncology Bio. Phys.* **78**(1), 104–110.

Cox, J.D., Kian Ang, K. (2010) Radiation Oncology: Rational-Technique-Results. *MOSBY Elsevier*. Ninth Edition.

Crosbie, J.C., Rogers, P.A.W., Stevenson, A.W., Hall C.J., Lye J.E., Nordström T., Midgley S.M., & Lewis, R.A. (2013) Reference dosimetry at the Australian Synchrotron's imaging and medical beamline using free-air ionization chamber measurements and theoretical predictions of air kerma rate and half value layer. *Med. Phys.* **40** (6), 062103.

CSIRO – website: https://ts-imaging.net/Services/Simple/ICUtilXdata.aspx

Dance, D.R. (1990) Monte Carlo calculation of conversion factors for the estimation of mean glandular breast dose. *Phys. Med. Biol.* **35**, 1211–1219.

Darby, S.C., Ewertz, M., McGale, P., Bennet, A.M., Blom-Goldman, U., Brønnum, D., Correra, C., Cutter, D., Gagliardi, G., Gifante, B., Jensen, M.B., Nisbet, A., Peto, R., Rahimi, K., Taylor, C., Hall, P. (2013) Risk of ischemic heart disease in women after radiotherapy for breast cancer. *N. Engl. Med.* **368,** 987–998.

David C, Weitkamp T, Pfeiffer F, Diaz A, Bruder J, Rohbeck T, Groso, A., Bunk, O., Stampanoni, M., Cloetens, P. (2007) Hard X-ray phase imaging and tomography using a grating interferometer. *Spectrochim. Acta B* **62**, 626–30.

Delogu, P., Golosio, B., Fedon, C., Arfelli, F., Bellazzini, R., Brez, A., Brun, F., Di Lillo, F., Dreossi, D., Mettivier, G., Minuti, M., Oliva, P, Pinchera, M., Rigon, L, Russo, P., Sarno, A., Spandre, G., Tromba, G., Longo, R. (2017a) Imaging study of a phase-sensitive breast-CT system in continuous acquistion mode. *J. Instrum.* **12**, C01016.

Delogu, P., Brombal, L., Di Trapani, V., Donato, S., Bottigli, U., Dreossi, D., Golosio, B., Oliva, P., Rigon, L., Longo, R. (2017b) Optimization of the equalization procedure for a single-photon countin CdTe detector used for CT. *J. Instrum.* **12**, C11014.

De Lucia, P. A. (2015) Kilovoltage rotational external beam radiation therapy (kV-EBRT) for breast cancer treatment. *M.Sc. thesis (Physics).* Università di Napoli Federico II. Available at: http://www.infn.it/thesis/PDF/getfile.php?filename=10622-De%20Lucia-magistrale.pdf

De Lucia, P. A., Mettivier, G., Di Lillo, F., Sarno, A., & Russo, P. (2016) SR-EBRT: Synchrotron radiation external beam rotational radiotherapy for breast cancer treatment. *Phys. Med.,* Suppl., **32**, 19.

Deman, P., Vautrin, M., Edouard, M., Stupar, V., Bobyk, L., Farion, R., Elleaume, H., Rémy, C., Barbier, E. L., Estève, F., & Adam, J. F. (2012) Monochromatic minibeams radiotherapy: from healthy tissue-sparing effect studies toward first experimental glioma bearing rats therapy. *Int. J. Radiat. Oncol. Biol. Phys.* **82** (4), 693–700.

De Rose, F., Fogliata, A., Franceschini, D., Navarria, P., Villa, E., Iftode, C., D'Agostino, G., Cozzi, L., Lobefalo, F., Mancosu, P., Tomatis, S., & Scorsetti, M. (2016) Phase II trial of hypofractionated VMAT- based treatment for early stage breast cancer: 2-year toxicity and clinical results. Radiat Oncol **11** (1):120.

Devic, S., Seuntjens, J., Hegyi, G., Podgorsak, E., Soares, C.G., Kirov, A.S., Ali, I., Williamson, J.F., & Elizondo, A. (2004) Dosimetric properties of improved Gafchromic films for seven differenr digitizers. *Med. Phys.* **31**, 2392–2241.

Devic, S., Seuntjens, J., Sham, E., Podgorsak, E., Schmidtlein C.R., Kirov, A.S., & Soares, C.G. (2005) Precise radiochromic film dosimetry using a flat-bed document scanner. *Med. Phys.* **31**, 2245–2253.

Devic, S., Tomic, N. & Lewis, D. (2016). Reference radiochromic film dosimetry: review of technical aspects. *Phys. Med.* **32**(4), 541–556.

Di Lillo, F. (2014) Phase-contrast breast computed tomography with a synchrotron radiation source and a single photon counting detector. *M.Sc. thesis (Physics).* Università di Napoli Federico II. Available at: http://www.infn.it/thesis/thesis_dettaglio.php?tid=9291

Di Lillo, F., Dreossi, D., Emiro, F., Fedon, C., Longo, R., Mettivier, G., Rigon L., Russo, P. & Tromba, G. (2015) Use of XR-QA2 radiochromic films for quantitative imaging of a synchrotron radiation beam. *J. Instrum.* **10**(05), C05002.

Di Lillo, F., Mettivier, G., Sarno, A., Tromba, G., Tomic, N., Devic, S. & Russo, P. (2016a) Energy dependent calibration of XR-QA2 radiochromic film with monochromatic and polychromatic x-ray beams. *Med. Phys.* **43**(1), 583–588.

Di Lillo, F., Mettivier, G., Sarno, A., & Russo, P. (2016b). Towards breast cancer rotational radiotherapy with synchrotron radiation. *Phys. Med.* **32**, Suppl. 3, 253–254.

Di Lillo, F., Mettivier, G., Sarno, A., Castriconi R., & Russo, P. (2017a). Towards breast cancer rotational radiotherapy with synchrotron radiation. *Phys. Med.* **41**, 20–25.

Di Lillo, F., Mettivier, G., Castriconi, R., Sarno, A., Hausermann, D., Hall, C, Stevenson, A.W., Russo, P. (2017b) *Synchrotron radiation external beam rotational radiotherapy of breast cancer: proof of principle.* J Synchrotron Rad, under review

Duggan, L, Hood, C., Warren-Forward, H., Haque, M., & Kron,T. (2004) Variation in dose response with x-ray energy of LiF:Mg, Cu, P thermoluminescence dosimeters: implication for clinical dosimetry. *Phys. Med. Biol.* **49**, 3831–3845.

Edouard, M., Broggio, D., Prezado, Y., Estève, F., Elleaume, H., Adam, J.F. (2010) Treatment plans optimization for contrast-enhanced synchrotron stereotactic radiotherapy. *Med. Phys.* **31**(6), 2445–2456.

Emiro, F., Di Lillo, F., Mettivier, G., Fedon, C., Longo, R., Tromba, G. & Russo, P. (2015) Energy response of GR-200A thermoluminescence dosemeters to 60Co and to monoenergetic synchrotron radiation in the energy range 28–40 keV. *Rad. Prot. Dosim.* **168**(1), 40–45.

Estève, F., Corde, S., Elleaume, H., Adam, J.F., Joubert, A., Charvet, A.M., Biston, MC, Balosso, J, Le Bas, JF. (2002) Enhanced radio sensitivity with iodinated contrast agents using monochromatic synchrotron X-rays on human cancerous cells. *Academic Radiology* **9** (s2), S540–S543.

Fardin, L., Oliva, P., Golosio, B., Brun, F., Rigon, L., Longo, R. (2016) Comparison among iterative reconstruction techniques for phase-sensitive breast tomography. *Phys. Med.* **32** (Suppl.3), 217.

Fedon, C., Longo, F., Mettivier, G., Longo, R. (2015) GEANT4 for breast dosimetry: parameters optimization study. *Phys. Med. Biol.* **60,** N311–323.

Fedon, C. (2016) Simulations and experimental assessment of dosimetric evaluations for breast imaging studies with Synchrotron Radiation. *Ph.D. thesis.* Università degli studi di Trieste, Trieste, Italy.

Fiedler, S., Bravin, A., Keyriläinen, J., Fernández, M., Suortti, P., Thomlinson, W., Tenhunen, M., Virkkunen, P., Karjalainen-Lindsberg, M.L. (2004) Imaging lobular breast carcinoma: comparison of synchrotron radiation DEICT technique with clinical CT, mammography and histology. *Phys. Med. Biol.* **49**,175–88.

Fogliata, A., Seppala, J., Reffiori, G., Lobefalo, F., Palumbo, V., De Rose, F., Franceschini, D., Scorsetti, M., Cozzi, L. (2017) Left breast cancer planning with VMAT technique:the dosimetric trade-offs. *Radiation and Oncology* **123** (Suppl. 1), S840.

Giaddui, T., Cui, Y., Galvin, J., Chen, W., Yu, Y., & Xiao, Y. (2012) Characteristics of GAfChromic XRQA2 films for kV image dose measurement. *Med. Phys.* **39**, 842–850.

Giaddui, T., Cui, Y., Galvin, J., Yu, Y., & Xiao, Y. (2013) Comparative dose evaluations between XVI and OBI cone beam CT systems using GafChromic XRQA2 film and nanoDot optical simulated luminescence dosimeters. *Med. Phys*. **40**, 062102.

Golosio, B., Brunetti, A., Cesareo, R. (2004) Algorithmic techniques for quantitative Compton tomography. *Nucl. Instrum. Methods* B **213**,108–11.

Gonzalez, V.J., Buchholz D.J., Langen, K.M., Olivera, G.H., Chauhan, B., Meeks, S.L., Ruchala, K.J., Haimerl, J., Lu, W., Kupelian, P.A. (2006) Evaluation of two tomotherapy-based techniques for the delivery of whole-breast intensity-modulated radiation therapy. *Int. J. Radiation Oncology Biol. Phys.* **65**(1), 284–290.

González, P.R., Furetta, C., Azorín, J. (2007) Comparison of the TL responses of two different preparations of LiF:Mg, Cu, P irradiated by photons of various energies. *Appl. Rad. Isotopes* **65**, 341–344.

Grandl, S., Willner, M., Herzen, J., Mayr, D., Auweter, S.D., Hipp, A., Pfeiffer, F., Reiser, M., Hellerhoff, K. (2013) Evaluation of phase-contrast CT of breast tissue at conventional X-ray sources – presentation of selected findings. *Z. Med. Phys.* **23**(3), 212–221.

Grotzer, M.A., Schültke, E., Bräuer-Krish, E., & Laissue, J. A. (2015) Microbeam radiation therapy: clinical perspectives. *Phys. Med.* **31**(6), 564–567.

Hammerstein, G.R., Miller, D.W., White, D.R., Masterson, M.E., Woodard, H.Q., Laughlin, J. S. (1979) Absorbed radiation dose in mammography. *Radiology* **130**, 485–91.

Henson, K.E., McGale, P., Taylor, C., Darby, S.C. (2013) Radiation-related mortality from heart disease and lung cancer more than 20 years after radiotherapy for breast cancer. *Br J Cancer* **108**,179–82.

Honda, C., Ohara, H., Gido, T. (2006) Image qualities of phase-contrast mammography. In: *Digital mammography 8th international workshop*, IWDM 2006. Manchester, UK, June 18–21, 2006 proceedings 4046. p. 281–8.

Horowitz, Y. S. (1984) Thermoluminescence and Thermoluminescent Dosimetry, vols I, II, and III. CRC Press.

Huang, S.Y., Boone, J.M., Yang, K., Kwan, A.L.C., Pachard, N. J. (2008) The effect of skin thickness determined using breast CT on mammographic dosimetry. *Med. Phys.* **35**, 1199–206.

Hubbell, J.H. & Seltzer, S.M. (1995). Tables of X-ray Mass Attenuation Coefficients and Mass Energy-Absorption Coefficients from 1 keV to 20 MeV for Elements Z = 1 to 92 and 48 Additional Substances of Dosimetric Interest. *NIST Technical Report 5632.*

IAEA 2011 Status of computed tomography. Dosimetry for wide cone beam scanners *IAEA Human Health Reports No 5* (Vienna: International Atomic Energy) (www-pub.iaea.org/ MTCD/Publications/PDF/Pub1528_web.pdf).

Kak, A.C., Slaney, M. (1988) Principles of Computed Tomographic Imaging. (New York: IEEE press).

Kalender, W.A., Beister, M., Boone, J.M., Kolditz, D., Vollmar, S.V., Weigel M.C.C. (2012) High-resolution spiral CT of the breast at very low dose: concept and feasibility consideration. *Eur. Radiol.* **22**, 1–8.

Kalender, W.A. (2014) Dose in x-ray computed tomography. *Phys. Med. Biol.* **59**, R129–50.

Keyriläinen, J., Fernaández, M., Fielder, S., Bravin, A:, Karjalainen-Lindsberg, M.L., Virkkunen, P., Elo, E.M., Tenhunen, M., Suortti, P., Thomlinmson, W. (2005) Visualisation of calcifications and thin collagen strands in human breast tumour specimens by the diffraction-enhanced imaging technique: a comparison with conventional mammography and histology. *Eur. J. Radiology* **53**(2), 226–237.

Keyriläinen, J., Fernaández, M., Lindsberg, M.L.K., Virkkunen, P., Leidenius, M., von Smitten, K., Sipilä, P., Fiedler, S., Suhonen, H., Suortti, P., Bravin, A. (2008) Toward high-contrast breast CT at low radiation dose. *Radiology* **249**, 321–327.

Khan, F.M., Gibbsons, J.P. (2014) The Physics of Radiation Therapy. *Wolters Kluwer*. Fifth Edition.

Kirby, A.M., Evans, P.M., Donovan, E.M., Convery, H.M., Haviland, J.S., Yarnold J.R. (2010) Prone versus supine positioning for whole and partial-breast radiotherapy: a comparison of non-target tissue dosimetry. *Radiother. Oncol.* **96**(2), 178–184.

Kron, T., Duggan, L., Smith, T., Rosenfeld, A., Butson, M., Kaplan, G., Howlett, S., & Hyodo, K. (1998) Dose response of various radiant detectors to synchrotron radiation. *Phys. Med. Biol.* **43**, 3235–3259.

Kwan, A.L.C., Boone, J.M., Yang, K., Huang, S.Y. (2007) Evaluation of the spatial resolution characteristics of a cone-beam breast CT scanner. *Med. Phys.* **34**, 275–81.

Lin, Y., Paganetti, H., McMahon, S. J., & Schuemann, J (2015). Gold nanoparticle induced vasculature damage in radiotherapy: Comparing protons, megavoltage photons, and kilovoltage photons. *Med. Phys.* **42**(10), 5890–5902.

Lindfors, K.K., Boone, J.M., Nelson, T.R., Yang, K., Kwan, A.L. & Miller, D.F. (2008) Dedicated breast CT: initial clinical experience. *Radiology* **246**(3), 725–733.

Longo, R., Tonutti, M., Rigon, L., Arfelli, f., Dreossi, D., Quai, E., Zanconati, F., Castelli, E., Tromba, G., Cova, M.A. (2014) Clinical study in phase-contrast mammography: image-quality analysis. *Phil. Trans. R. Soc.* **372**, 20130025.

Longo, R., Arfelli, F., Bellazzini, R., Bottigli, U., Brez, A., Brun, F., Brunetti, A., Delogu, P., Di Lillo, F., Dreossi, D., Fanti, V., Fedon, C., Golosio, B., Lanconelli, N., Mettivier, G., Minuti, M., Oliva, P., Pinchera, M., Rigon, L., Russo, P., Sarno, A., Spandre, G., Tromba, G., & Zanconati, F. (2016).

Towards breast tomography with synchrotron radiation at Elettra: first images. *Phys. Med. Biol.* **61**(4), 1634–1649.

Lymberis, S.C., Keith deWyngaert, J., Parhar, P., Chhabra, A.M., Fenton-Kerimian, M., Chang, J., Hochman, T., Guth, A., Roses, D., Goldberg, J.D., Formenti, S.C. (2012) Prospective assessment of optimal individual postion (Prone versus supine) for Breast Radiotherapy: Volumetric and dosimetric correlations in 100 patients. *Int. J. Radiation Oncol. Biol. Radiol.* **84**(4), 902–909.

MacDonald, S.M. (2016). Proton therapy for breast cancer: getting to the heart of the matter. *Int. J. Radiat. Oncol. Biol. Phys.* **95**(1),46–48.

Mackie, T.R., Holmes, T., Swerdloff, S., Reckwerdt, P., Deasy, J.O., Yang, J., Paliwal, B., Kinsella, T. (1993) Tomotherapy: A new concept fro the delivery of dynamic conformal radiotherapy. *Med. Phys.* **20**(6), 1709–1719.

Malvezzi, M., Carioli, G., Bertuccio, P., Boffetta, P., Levi, F., La Vecchia, C., Negri, E. (2017) European cancer mortality predictions for the year 2017, with focus on lung cancer. *Annals of Oncology* **28**, 1117–1123.

Manna, E., Maiti, S., Bhattachryya, S., Ghosh, S.K. (2016) Early detection of breast cancer: management with radiotherapy associated with cardiovascular disease (CVD), heart failure among the breast cancer survivors woman. *J Women's Health Care* **5**(4), http://dx.doi.org/10.4172/2167-0420.1000323.

Martella, E. Dosimetric characterisc of LiFMg, Cu, P (GR-200A). *A.S.G. – Applicazioni Scientifiche Generali*.

Martínez-Rovira, I., Sempau, J., Fernández-Varea, Bravin, A., Prezado, Y. (2010) Monte Carlo dosimetry for forthcoming clinical trials in x-ray microbeam radiation therapy. *Phys. Med. Biol.* **55**, 4375–4388.

Martínez-Rovira, I., Prezado, Y. (2011) Monte Carlo dose enhancement studies in microbeam radiation therapy. *Med. Phys.* **38**(7), 4430–4439

Martínez-Rovira, I., Sempau, J., Prezado, Y. (2012a) Development and commissioning of a Monte Carlo photon beam model for the forthcoming clinical trials in microbeam radiation therapy. *Med. Phys.* **39**(1), 119–131.

Martínez-Rovira, I., Sempau, J., Prezado, Y. (2012b) Monte Carlo-based treatment planning system calculation engine for microbeam radiation therapy. *Med. Phys.* **39**(5), 2829–2838.

Martínez-Rovira, I., Sempau, J., Prezado, Y. (2014) Monte Carlo-based dose calculation engine for minibeam radiation therapy. *Phys. Med.* **30**(1), 57–62.

Mast, M.E., Vredeveld, E.J., Credoe H. M., van Egmond, J., Heijenbrok, M.W., Hug, E.B., Kalk, P., van Kempen-Harteveld, L.M.L., Korevaar, E.W., van der Laan, H.P., Langendijk, J.A., Rozema, H.J.E., Petoukhova, A.L., Schippers, J.M., Struikmans, H. and & Maduro J. H. (2014). Whole breast proton irradiation for maximal reduction of heart dose in breast cancer patients. *Breast Cancer Res. Treat.* **148**(1)**,** 33–39.

Menegotti, L., Delana, A., & Martigliano A. (2008) Radiochromic film dosimetry with a flatbed scanner: a fast accurate method for dose calibration and uniformity correction with single film exposure. *Med. Phys.* **35**, 3078–3085.

Merchant, T.E., & McCormick, B. (1994). Prone postion breast irradiation. *Int. J. Radiation Oncol. Biol. Phys.* **30**(1), 197–203.

Mettivier G, Russo P. (2011a) Measurement of the MTF of a cone-beam breast computed tomography laboratory scanner. *IEEE Trans. Nucl. Sci.* **58**, 703–713.

Mettivier G., Russo P., Cesarelli M., Ospizio R., Passeggio G., Roscilli L., Pontoriere G., Rocco R. (2011b) Dedicated scanner for laboratory investigations on cone-beam CT/SPECT imaging of the breast. *Nucl. Instrum. Meth.* A **629**(1), 350–356.

Mettivier G., Fedon C., Di Lillo F., Longo R., Sarno A., Tromba G. & Russo P. (2016) Glandular dose in breast computed tomography with synchrotron radiation. *Phys. Med. Biol.* **61**(2), 569–587.

Mittone, A., Bravin, A., Coan, P. (2014a) Radiation dose in breast CT imaging with monochromatic x-rays: simulation study of the influence of energy, composition and thickness. *Phys. Med. Biol.* **59** 2199–206.

Mittone, A. (2014b) Development of X-ray phase-contrast imaging technique for medical diagnosis: towards clinical application. *Ph.D. thesis.* Ludwig-Maximilians-Universität, Munich, Germany. Available at: https://edoc.ub.uni-muenchen.de/18449/1/Mittone_Alberto.pdf.

Momose, A., Takeda, T., Itai, Y., Hirano, K. (1996) Phase-contrast X-ray computed tomography for observing biological soft tissues. *Nat. Med.* **2**,473–475.

Moorthy, S. (2016) IMRT versus VMAT for breast: a dosimetric point of view. *Radiotherapy and Oncology* **119** (Suppl. 1), S771.

Morris, K.N., Weil, M.D., Malzbender R. (2006) Radiochromic film dosimetry of contrast-enhanced radiotherapy (CERT). *Phys. Med. Biol.* **51**, 5915–5925.

Nakajima, T., Matuyama, Y., Matsuzawa, T., & Kojano, A. (1978) Development of a new highly sensitive LiF thermoluminescence dosimeter and its applications. *Nucl. Instrum. Methods* **157**, 155–162.

Nesterets, Y.I., Gureyev, T.E., Mayo, S.C., Stevenson, A.W., Thompson, D., Brown, J.M.C., Kitchen, M.J., Pavlov, K.M., Lokie, D., Brun, F., Tromba, G. (2015) A feasibility study of x-ray phase-contrast mammographic tomography at the imaging and medical beamline of the Australian synchrotron. *J. Synchrotron Radiat.* **22**, 1509–1523.

Nowotny, R. (1998) XMuDat: photon attenuation data on PC. *IAEA-NDS-195* https://www-nds.iaea.org/publications/iaea-nds/iaea-nds-0195.htm

Obeid, L., Deman, P., Tessier, A., Balosso, J., Estève, F., Adam, J.F. (2014) Absolute perfusion measurements and associated iodinated contrast agent time course in

brain metastasis: a study for contrast-enhanced radiotherapy. *J. Cereb. Blood. Flow Metab.* **34**(4), 638–645.

O'Connell A., Conover D. L., Zhang Y., Seifert P., Logan-Young W., Lin C. F. L., Sahler L. & Ning R. (2010) Cone-beam CT for breast imaging: Radiation dose, breast coverage, and image quality. *Am. J. Roentgenol.* **195**(2), 496–509.

O'Connell, A.M., Karellas, A., Vedantham, S. (2014) The potential role of dedicated 3D breast CT as a diagnostic tool: review and early clinical examples. *Breast J.* **20**, 592–605.

Olivo, A., Gkoumas, S., Endrizzi, M., Hagen, C.K., Szafraniec, M.B., Diemoz, P.C., Munro, P.R.T., Ignatyev, K., Johnson, B., Horrocks, J.A., Vinnicombe, S.J., Jones, J.L., Speler, R.D. (2013) Low-dose phase contrast mammography with conventional x-ray sources. *Med. Phis.* **40**(9), 090701.

Olko, P., Bilski, P., Ryba, E., & Niewiadomski, T. (1993) Microdosimetric interpretation of the anomalous photon energy response of ultra-sensitive LiF:Mg, Cu, P TL dosimeters. *Radiat. Prot. Dosim.* **47**, 31–35.

Olko, P., Bilski, P., Budzanowski, M., Waligòrski, M.P.R., Fasso, A., & Ipe, N. (1999) Modelling of the thermoluminescence response of LiF;Mg, Cu, P detectors after doses of low energy photons. *Radiat. Prot. Dosim.* **84**, 103–108.

Otto, K. (2008) Volumetric modulated arc therapy: IMRT in a single gantry arc. *Med. Phys.* **35**, 310–317.

Pacilè, S., Brun, F., Dullin, C., Nesterets, Y.I., Dreossi, D., Mohammadi, S., Tonutti, M., Stacul, F., Lokie, D., Zanconati, F., Accardo, A., Tromba, G., Gureyev, T.E. (2015) Clinical application of low dose phase contrast breast CT:methods for the optimization of the reconstruction workflow. *Biomed. Opt. Express* **6**(8), 3099.

Paganin, D., Mayo, S.C., Gureyev, T.E., Miller, P.R., Wilkins, S.W. (2002) Simultaneous phase and amplitude extraction from a single defocused image of a homogeneous object. *J. Microsc.* **206**, 33–40.

Pani, S., Longo, R., Dreossi, D., Montanari, F., Olivo, A., Arfelli, F., Bergamaschi, A., Poropat, P., Rigon, L., Zanconati, F. (2004) Breast tomography with synchrotron radiation: preliminary result.s *Phys. Med. Biol.* **49**, 1739–54.

Pelliccia, D., Poole, C.M., Livingstone, J., Stevenson, A.W., Smyth, L.M.L., Rogers, P.A.W., Haüsermann, D., & Crosbie, J.C. (2016) Image guidance protocol for synchrotron microbeam radiation therapy. *J. Synch. Radiat.* **23**(2), 566–573.

Podgorsak E. B. (2005) Radiation Oncology Physics: A Handbook for Teachers and Students. Vienna: International Atomic Energy Agency.

Poole, C.M., Day, L.R.J., Rogers, P.A.W., & Crosbie, J.C. (2017) Synchrotron microbeam radiotherapy in a commercially available treatment planning system. *Biom. Phys. Eng. Express* **3**(2), 025001.

Prezado, Y., Renier, M., Bravin, A. (2009a) A new method of creating minibeam patterns for synchrotron radiation therapy: a feasibility study. *J. Synchrotron Rad.* **16**, 582–586.

Prezado, Y., Thengumpallil, S., Renier, N., Bravin, A. (2009b) X-ray energy optimization in minibeam radiation therapy. *Med. Phys.* **36**(11), 4897–4902.

Prezado, Y., Martínez-Rovira, Thengumpallil, S., Deman, P. (2011) Dosimetry protocol for the preclinical trials in white-beam minibeam radiation therapy. *Med. Phys.* **38**(9) 5012–5020.

Prezado, Y., Sarun, S., Gil, S., Deamn, P., Bouchet, A., Le Duc, G. (2012) Increase of lifespan for glioma-bearing rats by using minibeam radiation therapy. *J. Synchrotron Rad.* **19**, 60–65.

Prezado, Y., Deman, P., Varlet, P., Jouvion, G., Gil, S., Le Clec, C., Bernard, H., Le Duc, G., Sarun, S. (2015) Tolerance to dose escalation in minibeam radiation therapy applied to normal rat brain: long-term clinical, radiological and histopathological analysis. *Radiation Research* **184**(3), 314–321.

Prezado, Y., Vautrin, M., Martínez-Rovira, I., Bravin, A., Estève, F., Elleaume, H., Berkvens, P., & Adam, J.F. (2011) Dosimetry protocol for the forthcoming clinical trials in synchrotron stereotactic radiation therapy (SSRT). *Med. Phys.* **38** (3), 1709–1717.

Prionas, N.D., Lindfors, K.K., Ray, S., Huang, S.Y., Beckett, L.A., Monsky W.L., Boone, J.M. (2010) Contrastenhanced dedicated breast CT: initial clinical experience *Radiology* **256**, 714–23.

Prionas, N.D., McKenney, S.E., Stern, R.L. and & Boone, J.M. (2012). Kilovoltage rotational external beam radiotherapy on a breast computed tomography platform: a feasibility study. *Int. J. Rad. Oncol. Biol. Phys.* **84**(2)**,** 533–539.

Quai, E., Longo, R, Zanconati, F., Jaconelli, G., Tonutti, M., Abrami, A., Arfelli, F., Dreossi, D., Tromba, G., Cova, M.A. (2013) First application of computed radiology to mammography with synchrotron radiation. *Radiol. Med.* **118** 89–100.

Rahman, W.N., Wong, C.J., Ackerly, T., Yagi, N., Geso, M. (2012) Polymer gels impregnated with gold nanoparticles implemented for measurements of radiation dose enhancement in synchrotron and conventional radiotherapy type beams. *Australs. Phys. Eng. Sci. Med.* **35**, 301–309.

Rakowski, J.T., Laha, S.S., Buczek M.G., Tucker M.A., Liu, F., Mao, G., Hillman, Y., Lawes, G. (2015) Measurement of gold nanofilm dose enhancement using unlaminated radiochromic film. Med. Phys. **42**(10), 5937–5944.

Rampado, O., Garelli, E:, Deagostini, D., & Ropolo, R. (2006) Dose and energy dpendence of response of GafCgromic XR-QA film for kilovoltage x-ray beam. *Phys. Med. Biol.* **51**, 2871–2881.

Rao, M., Yang, W., Chen, F., Sheng, K., Ye, J., Mehta, V., Shepard, D., Cao, D. (2010) Comparison of Elekta VMAT with helical tomotherapy and fixed field

IMRT: Plan quality, delivery efficiency and accurancy. *Radiation Therapy Physics* **37**(3), 1350–1359.

Rault, E., Lacornerie, T., Dang, H.P., Crop, F., Lartigau, E., Reynaert, N., Pasquier, D. (2016) Accelerated partial breast irradiation using robotic radiotherapy: a sodimetric comparison with tomotherapy and three-dimensional conformal radiotherapy. *Radiation Oncology* **11**(1), 29.

Renier, M., Brochard, Th., Nemoz, C., Requardt, H., Bräuer, E., Estève, F., Balosso, J., Suortti, P., Baruchel, J., Elleaume, H., Berruyer, G., Berkevens, P., Bravin A. (2008) The radiotherapy clinical trials projects at the ESRF: technical aspects. *Eur. J. Radiol.* **68**(3), S147–150.

Russo, P., Mettivier, G., Lauria, A., Montesi, M. C. (2010) X-ray cone-beam breast computed tomography: Phantom studies. *IEEE Trans. Nucl. Sci* **57**(1), 160-172.

Sarno, A., Mettivier, G., Russo, P. (2015) Dedicated breast computed tomography: basic aspects. *Med. Phys.* **42**(6), 2786–2804.

Sarno, A., Mettivier, G., Di Lillo, F. Russo, P. (2016a). Monte Carlo evaluation of normalized glandular dose coefficients in mammography. In *International Workshop on Digital Mammography*. Springer International Publishing. 190-196.

Sarno, A., Mettivier, G., Di Lillo, F., Russo, P. (2016b) A Monte Carlo study of monoenergetic and polyenergetic normalized glandular dose (DgN) coefficients in mammography. *Phys. Med. Biol.* **62** (1), 306-325.

Sarno, A., Mettivier, G, Golosio, B, Oliva, P, Spandre, G, Di Lillo, F, Fedon, C., Longo, R., Russo, P. (2016c) Imaging performance of phase-contrast breast computed tomography with synchrotron radiation and a CdTe photon-counting detector. Phys. Med. **32**(5), 681–690.

Sarno, A., Mettivier, G., Di Lillo, F., Cesarelli, M., Bifulco, P., Russo, P. (2016d) Cone-beam micro computed tomography dedicated to the breast. *Med. Engin. Phys.* **38**(12), 1449–1457.

Sarno, A. (2017a) Dose and image quality in X-ray phase contrast breast imaging. *Ph.D. thesis.* Università degli studi di Napoli Federico II, Napoli, Italy.

Sarno, A., Dance, D.R., van Engen, R.E., Young, K.C., Russo, P., Di Lilo, F., Mettivier, G., Bliznakova, K., Fei, B., Sechopoulos, I. (2017b) A monte carlo model for mean glandular dose evaluation in spot compression mammography. *Med. Phys.* **44**(7), 3848–3860

Sarno, A., Golosio, B., Russo, P., Arfelli, F., Bellazzini, R., Brez, A., Brun, F., Delogu, P., Di Lillo, F., Dreossi, D., Fedon, C., Longo, R., Mettivier, G., Oliva, P., Rigon, L., Spandre, G., Tromba, G. (2017d) A framework for iterative reconstruction in phase-contrast computed tomography dedicated to the breast. IEEE *Trans. Rad. Pl. Med. Sc*. DOI:10.1109/TRPMS.2017.2749059.

Sarno, A., Masi, M., Antonelli, N., Di Lillo, F., Mettivier, G., Castriconi, R., & Russo, P. (2017c) Dose volume distribution in digital breast tomosynthesis: a phantom study. *IEEE Trans. Rad. Pl. Med. Sc.* **1**(4), 322–328.

Serduc, R., Bräuer –Krisch, E., Bouchet, A., Renaud, L., Brochard, T., Bravin, A., Laissue, J., & Le Duc, G. (2009) First trial of spatial and temporal fractionations of the delivered dose using synchrotron microbeam radiation therapy. J. *Synchrotron Rad.* **16**(4), 587–590.

Sechopoulos, I., Feng, S.S.J., D'Orsi, C.J. (2010) Dosimetric characterization of a dedicated breast computed tomography clinical prototype. *Med. Phys.* **37**, 4110–20.

Sechopoulos, I. (2013a) A review of breast tomosynthesis: I. The image acquisition process. *Med. Phys.* **40**, 014301.

Sechopoulos, I. (2013b) A review of breast tomosynthesis: II. Image reconstruction, processing and analysis, and advanced application. *Med. Phys.* **40**, 014302.

Shapiro, S., Coleman, E.A.m Broeders, M., Codd, M., de Koning, H., Fracheboud, J., Moss, S., Paci, E., Stacjenko, S., Ballard-Barbash, R., for the International Breast Cancer Screening Network (IBSN) and the European Network of Pilot Projects for Breast Cancer Screening. (1998) Breast Cancer screening programmes in 22 countries: current policies, administration and guidelines. *Int. J. Epidemiol.* **27**(5),735–742

Shen, W., Tang, K., Zhu, H., & Liu, B. (2002) New advances in LiF:Mg, Cu, P TLDs (GR-200A). Radiat. Prot. Dosim. 100, 357–360.

Shi, L., Vedantham, S., Karellas, A. and O'Connel, A.M. (2013) Technical note: skin thickness measurements using high-resolution flat-panel cone-beam dedicated breast CT. *Med. Phys.* **40**, 031913.

Siegal, R.L., Miller, K.D., Jemal, A. (2016) Cancer Statistics, 2016. *CA Cancer J. Clin.* **66**, 7–30

Slatkin, D.N., Spanne, P., Dilmanian, F.A., & Sandborg, M. (1992) Microbeam radiation therapy. *Med. Phys*. **19**(6), 1395–400.

Snigirev, A., Snigireva, I., Kohn, V., Kuznetsov, S., Schelokov, I. (1995) On the possibilities of x-ray phase contrast microimaging by coherent high-energy synchrotron radiation. *Review of scientific instruments* **66**(12), 5486–5492.

Stampanoni, M., Wang, Z., Thüring, T., David, C., Roessi, E., Trippel, M., Kubik-Huch, R.A., Singer, G., Hohl, M.K., Hauser, N. (2011) The first analysis and clinical evaluation of native breast tissue using differential phase-contrast mammography. *Invest. Radiol.* 4**6**(12), 801–806,

Steiding, C., Kolditz, D., Roessler, A.C., Kalender, W.A. (2014) Quantitative assessment of the spatial dependence of non-stationary high-contrast spatial resolution, low-contrast detectability, and noise behavior in 3D imaging of the breast. In: 20th European congress of radiology (ECR) 2014, March 6–10, Vienna, Austria.

Stevenson, A.W., Mayo, S.C., Häusermann, D., Maksimenko, A., Garrett, R.F., Hall, C.J., Wilkins, S.W., Lewis, R.A. & Myers, D.E. (2010). First experiments on the Australian Synchrotron Imaging and Medical beamline, including investigations of the effective source size in respect of X-ray imaging. *J. Synch. Rad.* **17**(1), 75–80.

Stevenson, A.W., Hall, C.J., Mayo, S.C., Häusermann, D., Maksimenko, A., Gureyev, T.E., Nesterets, Y.I., Wilkins, S.W. & Lewis, R.A. (2012). Analysis and interpretation of the first monochromatic X-ray tomography data collected at the Australian Synchrotron Imaging and Medical beamline. Journal of synchrotron radiation *J. Synch. Rad.* **19**(5), 728–750.

Stevenson, A.W., Crosbie J.C., Hall, C.J., Häusermann, D, Livingstone, J. & Lye, J.E. (2017) Quantitative characterization of the X-ray beam at the Australian Synchrotron Imaging and Medical Beamline (IMBL). *J. Synch. Rad.* **24**(1), 110–14.

Szafraniec, M.B., Konstantinidis, A.C., Tromba, G., Dreossi, D., Vecchio, S., Rigon, L., Sodini, N., Naday, S., Gunn, S., McArthur, A., Olivo, A. (2015) Synchrotron based planar imaging and digital tomosynthesis of breast and biopsy phantoms using a CMOS active pixel sensor. *Phys. Med.* **31**(2), 192–198.

Sztrókay, A., Diemoz, P.C., Schlossbauer, T., Brun, E., Bamberg, F., Mayr, D., Reiser, N.F., Bravin A., Coan, P. (2012) High-resolution breast tomography at high energy: a feasibility study of phase contrast imaging on a whole breast. *Phys. Med. Biol.* **57**, 2931–2942.

Sztrókay, A., Herzen, J., Auweter, S.D., Liebhardt, S., Mayr, D., Willner, M., Hahn, D., Zanette, I., Weitkamp, T., Hellerhoff, K., Pfeiffer, F., Reiser, M.F., Bamberg, F. (2013) Assessment of grating-based X-ray phase-contrast CT for differentiation of invasive ductal carcinoma and ductal carcinoma in situ in an experimental ex vivo set-up. *Eur. Radiol.* **23**, 381–387.

Takeda, T., Momose, A., Ueno, E., Itai, Y. (1998) Phase-contrast X-ray CT image of breast tumor. *J Synchrotron Radiat* **5**, 1133–1135.

Takeda, T., Momose, A., Hirano, K., Haraoka, S., Watanabe, T., Itai, Y. (2000) Human carcinoma: early experience with phase-contrast X-ray CT with synchrotron radiation-comparative specimen study with optical microscopy. *Radiology* **214**, 298–301.

Thacker, S. C. and Glick, S.J. (2004) Normalized glandular dose (DgN) coefficients for flat-panel CT breast imaging. *Phys. Med. Biol.* **49**, 5433–5444.

Tomic, N., Devic, S., Deblois, F., & Seuntjens, J. (2010) Reference radiochromic film dosimetry in kilovoltage photon beams during CBCT image acquisition. *Med. Phys.* **37**, 1083–1092.

Tomic, N., Quintero, C., Whiting, B.R., Aldelaijan, S., Bekerat, H., Liang, L., Deblois, F., Seutjens, & Devic, S. (2014) Characterization of the calibration curves and energy dependence GafChromic™ XR-QA2 model based radiochromic film dosimetry system. *Med. Phys.* **41**, 062105.

Torre, L.A., Siegel, R.L., Ward, E.M., & Jemal, A. (2016). Global cancer incidence and mortality rates and trends—an update. *Cancer Epidemiol. Prev. Biomarkers* **25**(1), 16–27.

Tromba, G., Pacilè, S., Nesterets, Y.I., Brun, F., Dullin, C., Dreossi, D., Mayo, S.C., Stevenson, A.W., Pavlov, K.M., Kitchen, M.J., Thompson, D., Brown, J.M.C., Lockie, D., Tonutti, M., Stacul, F., Zanconati, F., Accardo, A., Gureyev, T.E. (2016) Phase-Contrast clinical breast CT: Optimization of Imaging setups and reconstruction workflows. In *International Workshop on digital mammography. Springer International Publishing*. 625–634.

Vedantham, S., Shi, L., Karellas, A., O'Connell, A.M., Conover, D.L. (2013) Personalized estimates of radiation dose from dedicated breast CT in a diagnostic population and comparison with diagnostic mammography. *Phys. Med. Biol.* **58**, 7921–7936.

Verma, V., Shah, C. & Mehta M.P. (2016) Clinical outcomes and toxicity of proton radiotherapy for breast cancer. *Clinical Breast Cancer* **16**(3)**,** 145–154.

Wysokinski, T., Harkness, T., Belev, G., Dawicki, W., Arnason, T., Gordon, J., Davies, G., Lobanova, L., Zhu, N., Webb, A., Miller, D., Chapman, D., & Liu, X. (2016) Induced Breast Cancer Cell Apoptosis by Synchrotron-Based Irradiation with Monochromatic Microbeams. *CMBES Proceedings* **39**(1).

Wilkins, S.W., Gureyev, T.E., Gao, D., Pogany, A., Stevenson, A.W. (1996) Phase-contrast imaging using polychromatic hard X-rays. *Nature* **384**, 335–338.

Willner, M., Herzen, J., Grandl, S., Auweter, S., Mayr, D., Hipp, A., Chbior, M., Sarapata, A., Achterhold, K., Zanette, I., Witkamp, T., Sztrókay, A., Hellerhoff, K., Reiser, M., Pfeiffer, F. (2014) Quantitative breast tissue characterization using grating-based x-ray phase-contrast imaging. *Phys. Med. Biol.* **59**, 1457–1571.

Wu, X., Gingold, E.L., Barnes, G.T., Tucker, D.M. (1994) Normalized average glandular dose in molybdenum target-rhodium filter and rhodium target-rhodium filter mammography. *Radiology* **193**, 83–89.

Xop 2.3 – website: http://www.esrf.eu/Instrumentation/software/dataanalysis/xop2.4 .

Yang, K., Kwan, A.L.C., Huang, S.Y., Packard, N.J., Boone, J.M. (2008) Noise power properties of a cone-beam CT system for breast cancer detection. *Med Phys.* **35**, 5317–27.

Yi Y, Lai C J, Han T, Zhing Y, Shen Y, Liu X, Ge S, You Z, Wang T and Shaw C C 2011 Radiation doses in cone-beam breast computed tomography: a Monte Carlo simulation study. *Med. Phys.* **38**, 589–97.

Yu, C.X. (1995) Intensity-modulated arc therapy with dynamic multileaf collimation: an alternative to tomotherapy. *Phys. Med. Biol.* **40**, 1435–1449.

Zhao, B., Zhang, X., Cai, W., Conover, D., Ning, R. (2015) Cone beam breast CT with multiplanar and three dimensional visualization in differentiating breast masses compared with mammography. *Eur. J. Radiol.* **84**, 48–53.

Zhao, Y., Brun, E., Coan, P., Huang, Z., Sztrókay, A., Diemoz, P.C., Liebhardt, S., Mittone, A., Gasilov, S., Miao, J., Bravin, A. (2012) High resolution, low dose phase contrast x-ray tomography for 3D diagnosis of human breast cancers. *Proc. Natl Acad. Sci. USA* **109**, 18290–94.